

Xu Feng

**Investigating scattering phenomena from Lattice
QCD using twisted mass fermions**

2010

Theoretische Physik

**Investigating scattering phenomena from Lattice
QCD using twisted mass fermions**

Inaugural-Dissertation
zur Erlangung des Doktorgrades
der Naturwissenschaften im Fachbereich Physik
der Mathematisch-Naturwissenschaftlichen Fakultät
der Westfälischen Wilhelms-Universität Münster

vorgelegt von
Xu Feng
aus Zhejiang, P.R.China

- 2010 -

Dekan:	Prof. Dr. Johannes P. Wessels
Erster Gutachter:	Prof. Dr. Gernot Münster
Zweiter Gutachter:	Priv.-Doz. Dr. Karl Jansen
Tag der mündlichen Prüfungen:	15.07.2010
Tag der Promotion:	15.07.2010

To my beloved parents.

ABSTRACT

We present results from first principle and non-perturbative Lattice QCD calculations which are directly relevant to scattering experiments of high energy physics. In particular, we study pion-pion scattering, where we analyze the ρ resonance parameters in the isospin $I = 1$ channel and the pion-pion scattering length in the $I = 2$ channel. In addition, we consider the e^+e^- scattering for which we provide a calculation of the leading order hadronic contribution a_μ^{had} to the anomalous magnetic moment of the muon. All the calculations are carried out using two dynamical flavors of maximally twisted mass fermions, which show a quadratic continuum limit scaling in the lattice spacing.

Concerning the S-wave pion-pion scattering length $a_{\pi\pi}^{I=2}$ in the isospin $I = 2$ channel we have used pion masses ranging from 520 MeV to 290 MeV and two lattice spacings of 0.079 fm and 0.063 fm. We use chiral perturbation theory at next-to-leading order to extrapolate our results to the physical point where we find $m_\pi a_{\pi\pi}^{I=2} = -0.0439(5)$. This can be compared to the recent experimental determination of $m_\pi a_{\pi\pi}^{I=2} = -0.0444(9)$ from NA48/2 at CERN.

For the P-wave pion-pion scattering phase in the rho decay channel we use very similar pion masses and lattice spacings as above and ensure that the physical kinematics for the ρ -meson decay, $m_\pi/m_\rho < 0.5$, is satisfied. Making use of finite size methods, we evaluate the pion-pion scattering phase in the center-of-mass frame and two moving frames, which allows us to map out the scattering phase as a function of the energy in the resonance region. From this we extract the ρ mass and decay width and study their quark mass dependence. The results obtained here demonstrate that resonances can indeed be analyzed on finite size lattices with numerical calculations, opening the prospect to tackle also other hadronic resonances.

Finally, we have calculated a_μ^{had} from the vacuum polarization tensor for pion masses from 640 MeV to 290 MeV. We have examined both finite size effects and lattice artifacts in our calculations, addressing therefore for the first time the systematic effects in the determination of a_μ^{had} .

ACKNOWLEDGEMENTS

First of all, I would like to thank Priv.-Doz. Dr. Karl Jansen. Karl brought this interesting thesis topic to me and supervised my Ph.D. study for three years. To me, he is not only a teacher of patience who taught me physics but also a mentor of vision who showed me how to learn physics.

I would like to thank Prof. Dr. Gernot Münster. Gernot kindly supported my Ph.D. study for three years only, if really true. I am deeply indebted for his help.

I would like to thank Prof. Dr. Chuan Liu. Chuan was the supervisor of my Bachelor and Master thesis. It is him who opened the door to the scientific world for me.

Special thanks go to Dr. Dru B. Renner. Dru generously shared with me his knowledge on physics, patiently showed me many lattice techniques, helpfully discussed with me all problems appearing in the course of my work and kindly gave me a lot of nice suggestions. For all this, I say thank you.

I would like to thank Dr. Carsten Urbach and Dr. Marc Wagner for technical help and providing their softwares. I thank Dr. Gregorio Herdoiza for his very valuable discussions.

I would like to thank all my friends at DESY Zeuthen and Humboldt University, in particular my officemates and colleagues, S. Dinter, E. Garcia Ramos, Ph. Gerhold, J. Gonzalez Lopez, I. Hailperin, D. Hesse, J. Kallarackal, P. Kovacikova, M. Marinkovic, A. Nube, M. Petschlies, F. Virotta and R. Welsing for the enjoyable time, the physics conversation and the warm friendship.

Privately, I must thank my housemates, Hadwig Dorsch and Chris Frederiksen, for their kind help, warm care and family-like treatment.

I would like to thank DESY for offering me the wonderful opportunity to study physics in Zeuthen and providing me office space and computer access.

Finally, I would like to thank the Deutsche Forschungsgemeinschaft for three years' financial support under grant SFB/TR9-03 and Mu 757/13.

TABLE OF CONTENTS

DEDICATION	iii
ABSTRACT	iv
ACKNOWLEDGEMENTS	v
LIST OF TABLES	ix
LIST OF FIGURES	x
I INTRODUCTION	1
II LATTICE QCD FUNDAMENTALS	9
2.1 Euclidean correlation functions	9
2.2 Lattice regularization	12
2.2.1 Lattice quark fields	13
2.2.2 Lattice gauge fields	15
2.3 Lattice QCD action – Wilson action	16
2.3.1 Computation of correlation functions	18
2.3.2 Continuum limit and Symanzik’s improvement program	19
2.4 Lattice QCD action – Wilson twisted mass action	20
2.4.1 Twisted mass fermion action	20
2.4.2 O(a) improvement	21
2.4.3 Isospin symmetry breaking	23
III FINITE SIZE METHODS	25
3.1 Scattering in the infinite volume	26
3.2 Scattering in a finite box	29
3.3 Finite size formulae in the center-of-mass frame	31
3.4 Generalization to the moving frame	34
3.5 Interpolating operators	38
IV I=2 CHANNEL: $\pi^+\pi^+$ SCATTERING LENGTH	42
4.1 Physical background	42
4.2 Method	44

4.2.1	Euclidean correlation function	44
4.2.2	Anti-periodic boundary conditions	45
4.3	Lattice calculation	47
4.3.1	Ensemble information	47
4.3.2	Stochastic sources	47
4.4	Results	48
4.4.1	Calculation of $m_\pi a_{\pi\pi}^{I=2}$	48
4.4.2	π^0 contamination	50
4.4.3	Finite volume effects	52
4.4.4	Lattice artifacts	53
4.4.5	Chiral extrapolation	53
V	I=1 CHANNEL: ρ RESONANCE PARAMETERS	57
5.1	Physical background	57
5.2	Method	59
5.2.1	Correlation matrix	59
5.2.2	Extraction of energies	61
5.2.3	Anti-periodic boundary conditions	62
5.3	Lattice calculation	64
5.3.1	Ensemble information	64
5.3.2	Various source methods	64
5.4	Results	66
5.4.1	Energy eigenvalues	66
5.4.2	Lattice discretization effects	68
5.4.3	Extraction of resonance parameters	69
5.4.4	Isospin symmetry breaking	71
5.4.5	Quark mass dependence	72
VI	VACUUM POLARIZATION AND HADRONIC MUON ANOMALOUS MAGNETIC MOMENT	79
6.1	Physical background	79
6.2	Determination of a_μ^{had}	82
6.2.1	Traditional method in Minkowski space	82

6.2.2	Lattice determination in Euclidean space	83
6.3	Determination of $\Pi(Q^2)$	84
6.3.1	Conserved current in the continuum	84
6.3.2	Conserved current on the lattice	85
6.3.3	Ward identities	86
6.4	Lattice setup	87
6.5	Results	88
6.5.1	$\Pi(\hat{Q}^2)$: analysis of systematic effects	88
6.5.2	a_μ^{had} : results from various data modeling	90
VII CONCLUSION AND OUTLOOK		98
CURRICULUM VITAE		113

LIST OF TABLES

3.1	List of the pion-pion interpolating operators, $\mathcal{O}_{\pi\pi}^{I,I_3}$, classified by Isospin number I and I_3	39
4.1	Ensembles used in the $I = 2$ pion-pion scattering. Only dimensionless quantities are needed in this calculation, but for guidance we give the value of m_π rounded to the nearest MeV for each ensemble indicated by β , $a\mu$ and L/a . We also list the ratio m_π/f_π , the number, N , of configurations used, the energy shift $a\delta E_{\pi\pi}^{I=2}$ and the scattering length $m_\pi a_{\pi\pi}^{I=2}$. The first uncertainty is statistical and, when present, the second one is systematic.	47
5.1	Ensembles used in the $I = 1$ pion-pion scattering. We give the ensemble name i.e. A_i, B_1 , the inverse bare coupling $\beta = 6/g_0^2$, the bare quark mass $a\mu$, the lattice size L/a and the value of m_π in units of MeV. We also list the ratio m_π/m_ρ and the number N of configurations used.	65
5.2	The results for the ρ -resonance mass m_ρ , the decay width Γ_ρ and the effective $\rho \rightarrow \pi\pi$ coupling $g_{\rho\pi\pi}$ at pion masses ranging from 480 MeV to 290 MeV.	71
5.3	The ρ mass and decay width from the chiral extrapolations of different models. The values of $m_{\rho,\text{phy}}, \Gamma_{\rho,\text{phy}}, M_\chi, \Gamma_\chi$ are given in units of GeV and $g_{\omega\rho\pi}$ in units of GeV^{-1}	73
5.4	Extraction of energy eigenvalues for the ground state and the first excited state in the CMF, MF1 and MF2. In the table we list the ensemble number, the reference time t_R , the beginning and end of the fitting window, t_{\min} and t_{\max} , the fit quality χ^2/dof and the fit results for energy eigenvalues E_n ($n = 1, 2$).	77
5.5	P-wave scattering phase $\delta_1(p)$ at the energies of the ground state and the first excited state in the CMF, MF1 and MF2. We list the ensemble number, the energy eigenvalue E_n , the center-of-mass energy E_{CM} , the momentum p , the scattering phase $\delta_1(p)$ in units of degree and $\sin^2 \delta_1(p)$. The results marked by a star denotes that the corresponding energy E_{CM} is above the $4m_\pi$ threshold. We therefore exclude them from our calculations.	78
6.1	Parameters used in the calculation of the hadronic vacuum polarization function.	87

LIST OF FIGURES

1.1	Experimental results for $R(s)$ in the range $1 \text{ GeV} < E = \sqrt{s} < 13 \text{ GeV}$ obtained at the various e^+e^- storage rings.	3
1.2	In the $I = 1$ channel the $e^+e^- \rightarrow \pi^+\pi^-$ cross section is shown. The ρ -resonance is formed in this channel.	5
4.1	The ratio $R(t)$ as a function of t . The solid lines are correlated fits to Eq. (4.19), from which the energy shifts $a\delta E_{\pi\pi}^{I=2}$ are extracted. The ensembles have been shifted vertically to facilitate easier comparison.	48
4.2	Chiral extrapolation for the $I=2$ pion-pion scattering length. The results in this work are shown together with the lattice calculations of NPLQCD [1,2] and CP-PACS [3] and the direct measurement from NA48/2 at CERN [4].	54
4.3	Difference between the lattice calculation of the scattering lengths and the LO χ PT prediction. The scattering lengths agree statistically with the LO χ PT prediction for $m_\pi = 290 \text{ MeV}$ to 520 MeV	55
5.1	For ensemble A_1 , the correlator $R_n(t, t_R)$ ($n = 1, 2$) as a function of t . From top to bottom, the three plots present the lattice calculations in the CMF, MF1 and MF2, respectively. The solid lines are correlated fits to Eq. (5.26), from which the energy eigenvalues E_n are extracted.	67
5.2	For ensemble A_2 , the correlator $R_n(t, t_R)$ ($n = 1, 2$) as a function of t . From top to bottom, the three plots present the lattice calculations in the CMF, MF1 and MF2, respectively. The solid lines are correlated fits to Eq. (5.26), from which the energy eigenvalues E_n are extracted.	67
5.3	For ensemble A_3 , the correlator $R_n(t, t_R)$ ($n = 1, 2$) as a function of t . From top to bottom, the three plots present the lattice calculations in the CMF, MF1 and MF2, respectively. The solid lines are correlated fits to Eq. (5.26), from which the energy eigenvalues E_n are extracted.	67
5.4	For ensemble A_4 , the correlator $R_n(t, t_R)$ ($n = 1, 2$) as a function of t . From top to bottom, the three plots present the lattice calculations in the CMF, MF1 and MF2, respectively. The solid lines are correlated fits to Eq. (5.26), from which the energy eigenvalues E_n are extracted.	67
5.5	For ensemble B_1 , the correlator $R_n(t, t_R)$ ($n = 1, 2$) as a function of t . From top to bottom, the three plots present the lattice calculations in the CMF, MF1 and MF2, respectively. The solid lines are correlated fits to Eq. (5.26), from which the energy eigenvalues E_n are extracted.	68
5.6	For ensemble A_1 , the scattering phases calculated in the CMF, MF1 and MF2 together with the effective range formula fit. At the positions where the scattering phase passes $\pi/2$ and $\pi/4$, the resonance mass m_ρ and the decay width Γ_ρ can be determined.	68

5.7	For ensemble A_2 , the scattering phases calculated in the CMF, MF1 and MF2 together with the effective range formula fit. At the positions where the scattering phase passes $\pi/2$ and $\pi/4$, the resonance mass m_ρ and the decay width Γ_ρ can be determined.	70
5.8	For ensemble A_3 , the scattering phases calculated in the CMF, MF1 and MF2 together with the effective range formula fit. At the positions where the scattering phase passes $\pi/2$ and $\pi/4$, the resonance mass m_ρ and the decay width Γ_ρ can be determined.	70
5.9	For ensemble A_4 , the scattering phases calculated in the CMF, MF1 and MF2 together with the effective range formula fit. At the positions where the scattering phase passes $\pi/2$ and $\pi/4$, the resonance mass m_ρ and the decay width Γ_ρ can be determined.	70
5.10	For ensemble B_1 , the scattering phases calculated in the CMF, MF1 and MF2 together with the effective range formula fit. At the positions where the scattering phase passes $\pi/2$ and $\pi/4$, the resonance mass m_ρ and the decay width Γ_ρ can be determined.	70
5.11	The ρ -meson mass as a function of the square of the pion mass. In the left panel, we fit the lattice results to Eq. (5.38). On the right panel, we fit them to Eq. (5.39).	74
5.12	The effective coupling $g_{\rho\pi\pi}$ as a function of the square of the pion mass. . .	76
5.13	The ρ decay width as a function of the square of the pion mass. In the left panel, we fit the lattice results to Eq. (5.38). On the right panel, we fit them to Eq. (5.39).	76
6.1	Leading hadronic contribution to $g - 2$	81
6.2	Volume dependence of $\Pi(\hat{Q}^2)$. This quantity requires an ultra-violet subtraction but is infra-red finite. Within the statistical errors there are no significant finite volume effects for $\Pi(\hat{Q}^2)$	89
6.3	Lattice spacing dependence of $\Pi(\hat{Q}^2)$ without the subtraction of $\Pi(\hat{0}^2)$ needed to regulate the vacuum polarization function.	90
6.4	Lattice spacing dependence of $\Pi(\hat{Q}^2) - \Pi(\hat{Q}_{\min}^2)$. The results have been renormalized at the lowest value of $\hat{Q}^2 \approx 0.1 \text{ GeV}^2$ at each lattice spacing to illustrate the effect of the subtraction. In the range $0.1 \text{ GeV}^2 < \hat{Q}^2 < 4 \text{ GeV}^2$, there is no explicit lattice spacing dependence.	91
6.5	Quark mass dependence of $\Pi(\hat{Q}^2)$ at large \hat{Q}^2 using $a = 0.079 \text{ fm}$. There is no noticeable quark mass dependence at large \hat{Q}^2 , consistent with pQCD expectations.	92
6.6	Quark mass dependence of $\Pi(\hat{Q}^2)$ at low \hat{Q}^2 using $a = 0.079 \text{ fm}$. There is a systematic, but not statistically significant, shift with quark mass from $m_\pi = 640 \text{ MeV}$ to 270 MeV	92

6.7	Quark mass dependence of $\Pi(\hat{Q}^2)$ at large \hat{Q}^2 using $a = 0.063$ fm. There is no noticeable quark mass dependence at large \hat{Q}^2 , consistent with pQCD expectations.	92
6.8	Quark mass dependence of $\Pi(\hat{Q}^2)$ at low \hat{Q}^2 using $a = 0.063$ fm. There is a systematic, but not statistically significant, shift with quark mass from $m_\pi = 640$ MeV to 270 MeV.	92
6.9	The low \hat{Q}^2 extrapolation of $\Pi(\hat{Q}^2)$ for $a = 0.079$ fm using polynomial fits. Each $\Pi(\hat{Q}^2)$ has been fit to cubic (dashed line) and quartic (solid line) functions of \hat{Q}^2 , showing agreement for all data sets.	93
6.10	The low \hat{Q}^2 extrapolation of $\Pi(\hat{Q}^2)$ for $a = 0.063$ fm using polynomial fits. Each $\Pi(\hat{Q}^2)$ has been fit to cubic (dashed line) and quartic (solid line) functions of \hat{Q}^2 , showing agreement for all data sets.	93
6.11	The results for a_μ^{had} using a cubic fit. Within the statistical errors, we do not find explicit finite size effects and lattice artifacts. Unfortunately, with the large errors, we do not find a clear quark mass dependence either. . . .	93
6.12	The results for a_μ^{had} using a quartic fit. As we increase the order of the polynomial from the cubic fit to the quartic fit the results become much noisier and a systematic, but not statistically significant, rise in a_μ^{had} is found. . . .	93
6.13	The low \hat{Q}^2 extrapolation of $\Pi(\hat{Q}^2)$ for $a = 0.079$ fm using a dipole fit. Each $\Pi(\hat{Q}^2)$ has been fit to the dipole function (6.40) of \hat{Q}^2 , showing agreement for all data sets.	94
6.14	The low \hat{Q}^2 extrapolation of $\Pi(\hat{Q}^2)$ for $a = 0.063$ fm using a dipole fit. Each $\Pi(\hat{Q}^2)$ has been fit to the dipole function (6.40) of \hat{Q}^2 , showing agreement for all data sets.	94
6.15	The results for a_μ^{had} using a dipole fit. Within the rather large statistical errors, we do not find explicit lattice artifacts and finite size effects in the determination of a_μ^{had} using the dipole fit. Unfortunately, there is no clear quark mass dependence either.	96

CHAPTER I

INTRODUCTION

Within the framework of the field of high energy physics, the main research focus is to understand the nature of the elementary constituents of matter and the fundamental interactions between them. Our present knowledge about elementary particles is encoded in the *Standard Model* of high energy physics which has been developed over many years by mutual efforts in theory and experiment. A major role in these developments has been played by collider experiments such as BEPC at IHEP China, LEP and LHC at CERN, Hera at DESY and Tevatron at Fermilab. The high energy scattering experiments are essential in the discovery of the by now known spectrum of elementary particles.

To illustrate the importance of scattering experiments, let us have a look at an e^+e^- collider. Here, beams of electrons and positrons, once having reached their design energy with a squared center-of-mass energy s , are brought to collisions leading to the creation of hadrons, leptons and gauge bosons in the e^+e^- -annihilation process. These particles are identified in large and very complex detectors which record the number of the corresponding scattering events, N_{events} . N_{events} is proportional to the scattering cross section $\sigma(s)$ which in turn can be computed theoretically from the Standard Model Lagrangian. Although N_{events} depends on the machine characteristics, such as the luminosity, the cross section itself is solely determined by the properties of the fundamental interactions and is hence the relevant physical quantity. Thus measuring the energy, momentum, and angular dependence of the reaction cross section from experiments and comparing it to theoretical calculations will probe the nature of fundamental interactions.

As a result, we have identified four types of fundamental interactions among particles, the strong, weak, electromagnetic and gravitational forces. The focus of this thesis is the strong force. *Quantum Chromodynamics* (QCD) as the underlying theory of the strong interaction [5–7] asserts the existence of quarks and gluons which are supposed to bind

together to form the experimentally observed hadrons (e.g. the proton, neutron, pion and rho) with a phenomenon called *quark confinement*. The strong force also binds the protons and neutrons together to form the nucleus of the atoms or gives rise to the creation of neutron stars.

In order to give a particular example of an e^+e^- collision experiment to reveal properties of the strong interaction, we will now look at $e^+e^- \rightarrow$ hadrons. To eliminate the effects from e^+e^- initial states, it is advantageous to measure the hadronic to leptonic cross section ratio

$$R(s) \equiv \frac{\sigma(e^+e^- \rightarrow \text{hadrons})}{\sigma(e^+e^- \rightarrow \mu^+\mu^-)}, \quad (1.1)$$

with $\sigma(e^+e^- \rightarrow \mu^+\mu^-) = 4\pi\alpha^2/3s$ and $\alpha = e^2/4\pi$ being the *Quantum electrodynamic* (QED) fine structure constant. Experimental results for $R(s)$ in the range $1 \text{ GeV} < \sqrt{s} < 13 \text{ GeV}$ are shown in Fig. 1.1 [8]. As can be seen, $R(s)$ provides a very rich spectrum of physical states which has revealed important information on the strong interactions.

A quantity which is closely related to $R(s)$, given in Minkowski space-time, is the Adler function [9–11]. It is defined through the following dispersive relation

$$D(Q^2) = Q^2 \int_{4m_\pi^2}^{\infty} \frac{R(s)}{(s+Q^2)^2} ds, \quad (1.2)$$

where $Q^2 = -q^2$ is now the *squared Euclidean momentum transfer*. The Adler function can be studied both experimentally by transforming the e^+e^- -data to a Euclidean momentum transfer and theoretically by evaluating the Lagrangian of QCD.

We remark that the change from a Minkowskian to an Euclidean metric will become particularly important when we discuss later lattice field theory techniques as employed in this thesis.

To make the bridge between experiments and theory more clear, we give another form of the Adler function

$$D(Q^2) = -(12\pi^2)Q^2 \frac{d\Pi(Q^2)}{dQ^2}. \quad (1.3)$$

Here, the *vacuum polarization function* $\Pi(Q^2)$ appears and it is this quantity which can be computed directly from Lattice QCD. Through the momentum transfer Q^2 , a scale

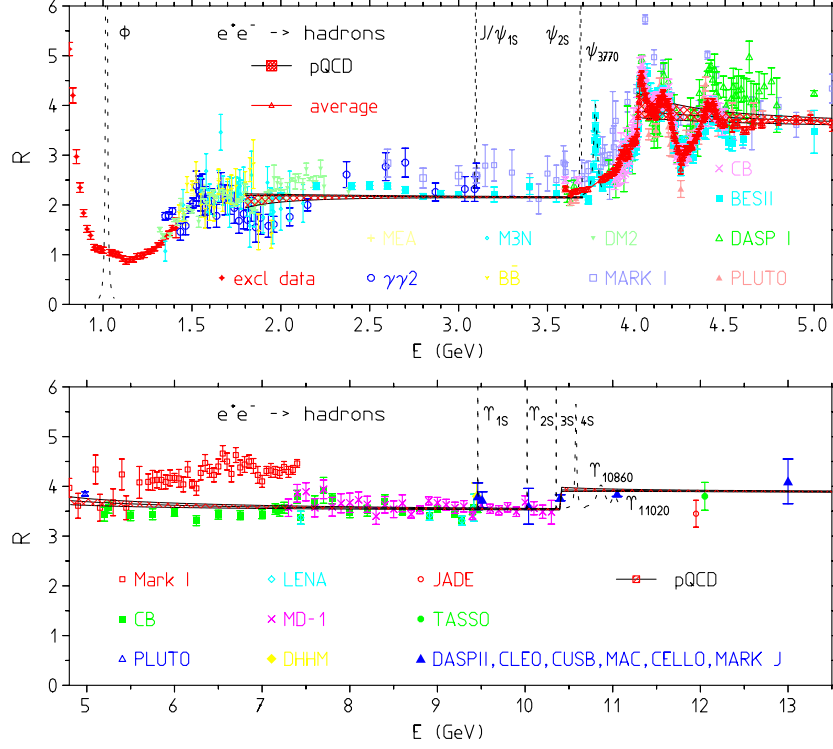


Figure 1.1: Experimental results for $R(s)$ in the range $1 \text{ GeV} < E = \sqrt{s} < 13 \text{ GeV}$ obtained at the various e^+e^- storage rings.

dependence is introduced with very large momenta corresponding to small physical distances while small momenta probe large distances. This momentum dependence can be used in the theoretical calculations by exploiting an important feature of QCD, namely *asymptotic freedom* [5, 12–14]. It means that the strong coupling becomes weaker and weaker with increasing energy scales. Thus from a certain high energy scale on, QCD is amenable to perturbation theory with a small coupling constant and the Feynman rules and diagrams of perturbative QCD (pQCD) can be used to compute $\Pi(Q^2)$.

This, of course, leaves open the question of how to treat the problem at small energy scales where the coupling constant is large and where we observe the spectrum of bound states, i.e. the experimentally determined hadrons. At these low energy scales, the confinement phenomenon sets in, pQCD fails to be applicable and the calculation of $\Pi(Q^2)$ requires a non-perturbative treatment. Such a non-perturbative method is provided by Lattice QCD and it is one of the subjects of this thesis to explain this method and to detail how it can be used to compute quantities related to scattering experiments.

To illustrate the importance of non-perturbative contributions, let us point out the computation of the muon anomalous magnetic moment, $a_\mu = (g_\mu - 2)/2$, a quantity that can be directly computed from $\Pi(Q^2)$. It is one of the most precisely measured quantities in high energy physics. Latest experiments at the Brookhaven National Laboratory [15] have reached an amazing accuracy of

$$a_\mu^{\text{EX}} = 11\,659\,208.9(6.3) \times 10^{-10} . \quad (1.4)$$

The theoretical calculations of a_μ based on the Standard Model have also reached a precision that matches the experimental one, giving [16, 17]

$$\begin{aligned} a_\mu^{\text{SM}} &= 11\,659\,183.4(4.9) \times 10^{-10} , & e^+e^- \text{-based} , \\ a_\mu^{\text{SM}} &= 11\,659\,193.2(5.2) \times 10^{-10} , & \tau \text{-based} . \end{aligned} \quad (1.5)$$

The discrepancy between experiments and the Standard Model value is 3.2σ (e^+e^- -based) or 1.9σ (τ -based). If this discrepancy remains or even gets larger with more precise experimental results and refined theoretical analysis, this would be a sign of a breakdown of the Standard Model and a hint for some unknown physics. However, it needs to be realized that among all the sources of the theoretical errors, the lowest order hadronic contribution, a_μ^{had} , is the dominant piece. This piece is of inherently non-perturbative nature and cannot be computed within pQCD. Thus, it is important to calculate a_μ^{had} accurately from first principles using only the QCD Lagrangian. It is here, where a lattice determination of $\Pi(Q^2)$ is essential to disentangle non-perturbative effects from those of new physics. The tool, how this can be achieved, is through the expression for a_μ^{had} ,

$$a_\mu^{\text{had}} = \alpha^2 \int_0^\infty \frac{dQ^2}{Q^2} F\left(\frac{Q^2}{m_\mu^2}\right) (\Pi(Q^2) - \Pi(0)) , \quad (1.6)$$

where m_μ is the muon mass and $F(\frac{Q^2}{m_\mu^2})$ is a known kernel [18]. Hence, once $\Pi(Q^2)$ has been determined non-perturbatively, also a_μ^{had} can be computed. The actual value of a_μ^{had} as computed from Lattice QCD will be one of the main results of this thesis. In the above discussion, we have shown some results of the e^+e^- scattering experiments. The ratio $R(s)$, given in Eq. (1.1), is then used as an example for a quantity that can be determined by

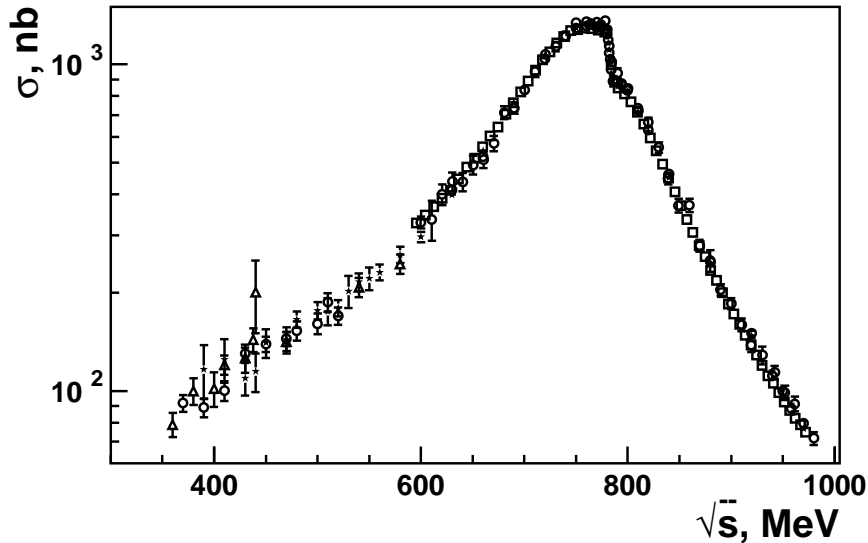


Figure 1.2: In the $I = 1$ channel the $e^+e^- \rightarrow \pi^+\pi^-$ cross section is shown. The ρ -resonance is formed in this channel.

such data and confronted with theoretical calculations and in particular to Lattice QCD computations to address non-perturbative effects.

Let us give a second example of such a bridge between experiment and Lattice QCD. To this end, we consider e^+e^- collisions at low energies. In this case, the final state consists necessarily of two pions. Focusing on the isospin $I = 1$ channel, the corresponding $e^+e^- \rightarrow \pi^+\pi^-$ cross section is shown in Fig. 1.2 [19]. The clearly visible peak in the cross section corresponds to the neutral and unstable $\rho(770)$ -meson. The peak position of the cross section can be identified with the mass of the $\rho(770)$ -meson, m_ρ , while the position where the cross section drops to half of its peak value can be related to the decay width, Γ_ρ .

Fig. 1.2 demonstrates that experimentally the mass of a hadron and its decay width, in case it is unstable as many hadrons are, can be determined rather accurately. The latest PDG [20] values of $m_\rho = 775.49(34)$ MeV and $\Gamma_\rho = 149.1(8)$ MeV show that such a determination can reach a precision of the 1 MeV level. Naturally, the question arises, whether we can compute hadron masses and decay widths, which are important quantities to understand the dynamics of the strong interaction, from QCD. Since hadrons are bound

states of quarks and gluons, their properties are of an inherently non-perturbative nature and cannot be computed within pQCD. One way to yield results for the masses and decay widths is to use again Lattice QCD. However, while a stable hadron mass can be straightforwardly computed in Lattice QCD, as shown below, the calculation of the decay width of a resonance encounters conceptual problems. Resonances are defined in Minkowski space and infinite volume, while Lattice QCD is formulated in Euclidean space. Furthermore, if we think of numerical simulations, necessarily a finite physical volume is to be used.

It is one subject of this thesis to show how these two conceptual difficulties can be circumvented and that the resonance properties of the ρ -meson can be analyzed utilizing lattice techniques, resulting in a determination of the ρ -meson mass and width from first principles.

The way to treat the ρ -meson on the lattice is to determine the pion-pion scattering phase from Lattice QCD using Lüscher's finite size methods [21–25], which establish relations between the discrete energy spectrum in a finite volume and the elastic scattering phase in the infinite volume. According to a partial wave analysis, the total cross section, σ , is related to l -th partial wave scattering phase, δ_l , through

$$\sigma \propto \sum_l (2l + 1) \sin^2 \delta_l . \quad (1.7)$$

Thus, a way to determine the resonance mass and width is to seek the position where the scattering phase, which dominates the contributions to the cross section, passes $\pi/2$ and $\pi/4$. Our ultimate goal is to determine the ρ -resonance mass and decay width from the P-wave $\pi^+\pi^-$ scattering phase in the $I = 1$ channel and compare the lattice results with experiments.

The case of the ρ -meson is used here as an ideal laboratory for lattice studies of resonances for two reasons. First, in the lattice calculations, the noise to signal ratio for a meson is proportional to $e^{m_M - m_\pi}$, where m_M is the meson mass. Since the ρ is one of the lightest mesons, the statistical error can be well controlled. Second, the principal decay channel of the ρ -meson is to a pair of pions with a branching rate of 99.9%. As a result, a two-pion scattering system provides an ideal laboratory for the study of ρ -resonance.

Besides the $I = 1$ channel, we perform a calculation of the S-wave pion-pion scattering phase in the $I = 2$ channel. Since no resonances are formed in this channel, the interest here is to calculate the corresponding scattering length which is important because it determines the leading low-energy behavior of the scattering phase. Furthermore, the pion mass dependence of the scattering length allows to determine a low energy constant (LEC) of chiral perturbation theory (χ PT) [26,27] that enters the quark mass dependence of the scattering length.

Above we have provided three examples, the vacuum polarization function and pion-pion scattering in the $I = 1$ and $I = 2$ channels, which are related to scattering experiments. We argued that quantities related to these experiments can be computed theoretically in a non-perturbative way using lattice field theory. In the following, we will demonstrate in detail how such a calculation can be carried through and provide a study of the systematic effects of the computation.

We remark that all calculations are performed using the two flavor maximally twisted mass fermion [28] ensembles from the European Twisted Mass Collaboration (ETMC) [29–32]. These ensembles, obtained at a number of lattice spacings, quark masses and volumes provide the necessary input for not only computing values for the quantities of interest, but also to allow a controlled estimate of the systematic effects appearing in the calculation.

The thesis is organized as follows. In Chapter 2, the lattice formalism of gauge and fermion fields are given. Here we also explain the formulation of maximally twisted mass fermions and how it reduces lattice artifacts to appear only at $O(a^2)$. In Chapter 3, the basic idea of Lüscher’s finite size method is described and its extension to the moving frame is given. In Chapter 4, a calculation of the S-wave pion-pion scattering length in the $I = 2$ channel is presented, together with the determination of relevant LEC. In Chapter 5, the P-wave pion-pion scattering phase in the isospin $I = 1$ channel is calculated, from which the ρ -meson resonance mass, its decay width and the effective $\rho \rightarrow \pi\pi$ coupling constant, $g_{\rho\pi\pi}$, are extracted. Finally, a chiral extrapolation is performed to extract the values of the ρ -meson mass and decay width at the physical point. In Chapter 6, a calculation of the vacuum polarization function is presented, which is finally used to determine the lowest

order hadronic contribution to the muon anomalous magnetic moment, a_μ^{had} .

CHAPTER II

LATTICE QCD FUNDAMENTALS

By now, Lattice QCD is a well established non-perturbative approach to study QCD. It allows to address questions which are relevant not only at large energies where, thanks to asymptotic freedom, perturbation theory works but also at low energies where non-perturbative phenomena take place. Indeed, Lattice QCD has been originally developed by K. G. Wilson in 1974 to understand quark confinement [33]. Soon after the formulation of Lattice QCD, numerical simulation techniques have been developed [34] which have turned out to be a particularly useful tool for Lattice QCD computations. However, due to the immense cost of such numerical simulations, the calculations were restricted to approximations such as infinitely heavy sea quark masses (*quenched approximation*). Fortunately, the last years have seen substantial improvements of the numerical algorithms employed and complemented by a tremendous increase of computing power with BG/P systems reaching Petaflops today. In addition, conceptual developments such as an acceleration of the continuum limit or non-perturbative renormalization have helped significantly to obtain phenomenologically relevant results. In fact, simulations are performed nowadays at small values of the lattice spacing, large volumes and almost realistic values of the quark masses. In this way, a real connection to experimental results can be established and in this thesis, we will discuss three particular applications as already outlined in the introduction.

In this chapter, I introduce first the basic theoretical scope of Lattice QCD before I turn to the the specific computations performed in this thesis. For more details, I refer the readers to the textbooks [35–38] and the review articles [39–41].

2.1 Euclidean correlation functions

Many quantities in Lattice QCD can be computed from the evaluation of suitable correlation functions. We therefore begin by discussing the construction of lattice correlation functions

as the basic objects from which physical quantities of interest can be computed.

Let us start from a standard correlation function in Minkowski space, i.e. time ordered two point function

$$C_M(t, \vec{k}) = \int d^3 \vec{x} e^{-i\vec{k}\cdot\vec{x}} \left\langle \Omega \left| T \left[\mathcal{O}_1(\vec{x}, t) \mathcal{O}_2^\dagger(\vec{0}, 0) \right] \right| \Omega \right\rangle \quad (2.1)$$

where the operator \mathcal{O}_2^\dagger represents the Heisenberg creation operator of a state with quantum numbers of \mathcal{O}_2 at space-time point $(\vec{0}, 0)$ and the Heisenberg operator \mathcal{O}_1 represents the annihilation operator of a state at space-time point (\vec{x}, t) . The integration over space-like coordinates constraints the state momentum to a certain momentum \vec{k} . The Heisenberg operator $\mathcal{O}_1(\vec{x}, t)$ can be written as

$$\mathcal{O}_1(\vec{x}, t) = e^{i\hat{H}t - i\hat{p}\cdot\vec{x}} \mathcal{O}_1(\vec{0}, 0) e^{-i\hat{H}t + i\hat{p}\cdot\vec{x}}, \quad (2.2)$$

so that

$$C_M(t, \vec{k}) = \int d^3 \vec{x} e^{-i\vec{k}\cdot\vec{x}} \left\langle \Omega \left| e^{i\hat{H}t - i\hat{p}\cdot\vec{x}} \mathcal{O}_1(\vec{0}, 0) e^{-i\hat{H}t + i\hat{p}\cdot\vec{x}} \mathcal{O}_2^\dagger(\vec{0}, 0) \right| \Omega \right\rangle. \quad (2.3)$$

In Eq. (2.3), it is assumed that $t > 0$ and the time ordered product is dropped. The Hamilton operator \hat{H} remains unspecified at this point with its particular form being dictated by the physical problem under consideration. Since the vacuum is time-space translation invariant, the correlation function can be simplified as

$$C_M(t, \vec{k}) = \int d^3 \vec{x} e^{-i\vec{k}\cdot\vec{x}} \left\langle \Omega \left| \mathcal{O}_1(\vec{0}, 0) e^{-i\hat{H}t + i\hat{p}\cdot\vec{x}} \mathcal{O}_2^\dagger(\vec{0}, 0) \right| \Omega \right\rangle. \quad (2.4)$$

In order to adopt the above Minkowski correlation function for Lattice QCD, a Wick rotation $t \rightarrow -it$ needs to be done, which corresponds to an analytical continuation from Minkowski to Euclidean space, where the two-point function is now given by

$$C_E(t, \vec{k}) = \int d^3 \vec{x} e^{-i\vec{k}\cdot\vec{x}} \left\langle \Omega \left| \mathcal{O}_1(\vec{0}, 0) e^{-\hat{H}t + i\hat{p}\cdot\vec{x}} \mathcal{O}_2^\dagger(\vec{0}, 0) \right| \Omega \right\rangle. \quad (2.5)$$

Under the condition of *Osterwalder-Schrader reflection positivity* [42] which amounts basically to demand the positivity of the Hamilton operator \hat{H} , it is guaranteed that the Euclidean correlation function contains the same physical information as its Minkowskian

counterpart. By inserting a complete set of energy eigenstates

$$\mathbf{1} = \sum_n \frac{1}{(2\pi)^3} \int d^3\vec{p} |E_n^{\vec{p}}, \vec{p}\rangle \langle E_n^{\vec{p}}, \vec{p}|, \quad (2.6)$$

one obtains

$$\begin{aligned} C_E(t, \vec{k}) &= \sum_n \int d^3\vec{p} \delta(\vec{k} - \vec{p}) \langle \Omega | \mathcal{O}_1(\vec{0}, 0) e^{-E_n^{\vec{p}} t} |E_n^{\vec{p}}, \vec{p}\rangle \langle E_n^{\vec{p}}, \vec{p}| \mathcal{O}_2^\dagger(\vec{0}, 0) | \Omega \rangle \\ &= \sum_n \langle \Omega | \mathcal{O}_1(\vec{0}, 0) |E_n^{\vec{k}}, \vec{k}\rangle \langle E_n^{\vec{k}}, \vec{k}| \mathcal{O}_2^\dagger(\vec{0}, 0) | \Omega \rangle e^{-E_n^{\vec{k}} t}. \end{aligned} \quad (2.7)$$

The eigenstates $|E_n^{\vec{k}}, \vec{k}\rangle$ are selected by the quantum numbers associated with the interpolating operators \mathcal{O}_1 and \mathcal{O}_2 . If $|n\rangle$ is a stable single-particle state with mass M_n , then its energy $E_n^{\vec{k}}$ is equal to $\sqrt{M_n^2 + \vec{k}^2}$.

In particular, in the zero momentum case, $\vec{k} = 0$, one can directly extract the mass of a particle with the quantum number of the state $|n\rangle$. In this way, it is possible in Lattice QCD to directly extract hadron masses from the computation of the Euclidean correlation functions. For example, consider the two-point function

$$C_\pi(t) = \int d^3\vec{x} \langle \Omega | \pi^+(\vec{x}, t) \pi^-(\vec{0}, 0) | \Omega \rangle \quad (2.8)$$

of the field

$$\pi^\pm = \bar{\psi} \gamma_5 \frac{\tau^\pm}{2} \psi, \quad \psi = \begin{pmatrix} u \\ d \end{pmatrix} \quad (2.9)$$

where u and d represent the up- and down-quark fields, and τ^\pm the isospin Pauli matrices.

The large-time behavior of correlation function $C_\pi(t)$ is given by

$$C_\pi(t) = e^{-m_\pi t} |\langle \Omega | \pi^+ | \pi^- \rangle|^2 + O(e^{-3m_\pi t}). \quad (2.10)$$

Asymptotically, for large enough Euclidean time separation t , $C_\pi(t)$ is dominated by the single-pion state and the pion mass m_π can be extracted from the exponential fall-off of the correlation function,

$$m_\pi = - \lim_{t \rightarrow \infty} \frac{\partial}{\partial t} \ln C_\pi(t). \quad (2.11)$$

It is important to stress that the so-obtained pion mass is identical to the corresponding one in Minkowski space. However, these arguments only hold for stable particles. Some

resonances, such as ρ and σ mesons or the Δ baryon have masses greater than the many-particle threshold. Thus they can no longer be extracted by simply measuring the ground state energy. How to calculate the resonance parameters such as the resonance mass and decay width is one of the major topics of this thesis which will be discussed in detail in Chapter 5. There, the ρ -resonance will be treated as an example, on one hand being interesting on its own and on the other hand serving as a laboratory case for eventual studies of other hadron resonances.

2.2 Lattice regularization

To actually compute the Euclidean correlation functions, one makes use of the path integral formulation of quantum field theories. Let us take QCD as an example. The expectation value of a two-point correlation function is then given by

$$\langle \mathcal{O}(x_1) \mathcal{O}^\dagger(x_2) \rangle = \frac{1}{\mathcal{Z}} \int \mathcal{D}\psi \mathcal{D}\bar{\psi} \mathcal{D}A \mathcal{O}(x_1) \mathcal{O}^\dagger(x_2) \exp(-\mathcal{S}[\bar{\psi}, \psi, A_\mu]) , \quad (2.12)$$

where normalization factor \mathcal{Z} is a path integral, named *partition function*

$$\mathcal{Z} = \int \mathcal{D}\bar{\psi} \mathcal{D}\psi \mathcal{D}A \exp(-\mathcal{S}[\bar{\psi}, \psi, A_\mu]) . \quad (2.13)$$

\mathcal{S} is the QCD action, and ψ and A_μ denote the quark and gluon fields. In order to evaluate the correlation function, the functional integral appearing in Eq. (2.12) needs to be computed. A conceptually clean way to perform this calculation is to consider it as a limit of a well-defined integral over a *discretized* Euclidean space-time lattice with lattice spacing a . One hence introduces a hypercubic lattice

$$\Lambda = a\mathbf{Z}^4 = \{x | x_\mu/a \in \mathbf{Z}\} . \quad (2.14)$$

In addition, we will consider the system in a *finite* volume with size La . Thus the allowed momenta are given by

$$p = \pm \frac{2\pi n}{La} , \quad n = 1, \dots, L/2 . \quad (2.15)$$

For a non-zero value of a , the maximal momentum that exists on the lattice is of the order $\sim \frac{\pi}{a}$, which serves as an ultraviolet cutoff. For a finite size L , the minimal momentum is

given by $2\pi/(La)$, which provides an infrared regulator of the theory. Thus, the functional integral is completely well-defined. The original functional integral can then be understood as a limit of sending the volume to infinity and the lattice spacing to zero. It is worth mentioning that this finite lattice regularization of the functional path integral has served as a mathematical basis to study fundamental properties of quantum field theories, see e.g. [43].

2.2.1 Lattice quark fields

In order to introduce the quark fields on the lattice, let us first consider the Euclidean free-quark field two-point function in the continuum,

$$\langle \psi(x)\bar{\psi}(0) \rangle = \int \frac{d^4p}{(2\pi)^4} \frac{e^{ipx}}{i\gamma p + m}, \quad (2.16)$$

where the 4-vector inner products px and γp are given as

$$px = p_0t + \vec{p} \cdot \vec{x}, \quad \gamma p = \gamma_0 p_0 + \sum_i \gamma_i p_i. \quad (2.17)$$

The Euclidean Dirac matrices γ_μ are hermitian and satisfy the anti-commutation relation

$$\gamma_\mu^\dagger = \gamma_\mu, \quad \{\gamma_\mu, \gamma_\nu\} = \delta_{\mu\nu}. \quad (2.18)$$

Using Eqs. (2.17) and (2.18) and integrating Eq. (2.16) in the p_0 direction we obtain

$$\langle \psi(x)\bar{\psi}(0) \rangle = \int \frac{d^3\vec{p}}{(2\pi)^3} \frac{-i\gamma p + m}{2E} e^{-Et + i\vec{p}\cdot\vec{x}}, \quad E = \sqrt{m^2 + \vec{p}^2}. \quad (2.19)$$

Besides, we find that the two-point correlation function fulfills the Dirac equation

$$(\gamma\partial + m) \langle \psi(x)\bar{\psi}(0) \rangle = \delta(x). \quad (2.20)$$

Let us now step to the anticipated discretized space-time and replace continuum space-time by a 4-dimensional hypercubic lattice Λ . The the quark fields $\psi(x)$ and $\bar{\psi}(x)$ are now defined only at discrete points $x \in \Lambda$. Furthermore, the continuum partial derivative operator is replaced by forward and backward lattice derivatives

$$\begin{aligned} \partial_\mu \psi(x) &= \{\psi(x + a\hat{\mu}) - \psi(x)\} / a \\ \partial_\mu^* \psi(x) &= \{\psi(x) - \psi(x - a\hat{\mu})\} / a. \end{aligned} \quad (2.21)$$

Performing the Fourier transform, in momentum space we have

$$\partial_\mu \rightarrow \frac{1}{a} \{e^{iap_\mu} - 1\} = ip_\mu \{1 + O(ap)\} \quad (2.22)$$

Although the so-defined lattice derivatives reproduce the continuum derivative operator in the limit of vanishing lattice spacing, it is not sufficient to use them as the kinetic operator for lattice fermions as they stand. As realized by Wilson in Ref. [33], this would lead to a proliferation of fermion modes in the continuum limit. The solution found by Wilson is to modify the kinetic term for fermions on a lattice and he proposed a lattice Dirac operator D_W which reads

$$D_W = \sum_{\mu=0}^3 \frac{1}{2} \{ \gamma_\mu (\partial_\mu^* + \partial_\mu) - ar \partial_\mu^* \partial_\mu \} \quad (2.23)$$

where $ar \partial_\mu^* \partial_\mu$ is the so-called *Wilson term*, which is added to decouple the unwanted additional fermion modes, named *doublers*. One can then show that this so-called Wilson-Dirac operator indeed describes only one fermion flavor in the continuum limit. We mention that this doubling problem is deeply connected to other fundamental properties of the theory such as locality and chiral symmetry as summarized in the Nielsen-Ninomiya theorem [44].

Let us set the Wilson parameter to be $r = 1$ and perform the Fourier transform

$$\begin{aligned} \frac{1}{2} (\partial_\mu^* + \partial_\mu) &\rightarrow \frac{i}{a} \sin(ap_\mu) \equiv i\hat{p}_\mu \\ \partial_\mu^* \partial_\mu &\rightarrow -\hat{p}_\mu \hat{p}_\mu, \quad \hat{p}_\mu \equiv \frac{2}{a} \sin\left(\frac{ap_\mu}{2}\right). \end{aligned} \quad (2.24)$$

In momentum space, the Wilson-Dirac operator is simply given by

$$D_W \rightarrow i\gamma\hat{p} + \frac{1}{2}a\hat{p}^2. \quad (2.25)$$

Solving the Dirac equation

$$(D_W + m) \langle \psi(x) \bar{\psi}(0) \rangle = a^{-4} \delta_{x0}, \quad (2.26)$$

one obtains the free-quark two-point function on the lattice

$$\begin{aligned} \langle \psi(x) \bar{\psi}(0) \rangle &= \int_{-\pi/a}^{\pi/a} \frac{d^4 p}{(2\pi)^4} \frac{e^{ipx}}{i\gamma\hat{p} + \frac{1}{2}a\hat{p}^2 + m} \\ &= \int_{-\pi/a}^{\pi/a} \frac{d^3 \vec{p}}{(2\pi)^3} e^{-Et + i\vec{p}\cdot\vec{x}} \rho(\vec{p}) \end{aligned} \quad (2.27)$$

where E is the energy of a lattice quark with 3-momentum \vec{p} and $\rho(\vec{p})$ is the associated spectral density. By expanding in powers of the lattice spacing a , E and $\rho(\vec{p})$ are given by

$$E = \sqrt{m^2 + \vec{p}^2} + O(am, a\vec{p}), \quad \rho(\vec{p}) = \frac{-i\gamma p + m}{2E} + O(am, a\vec{p}). \quad (2.28)$$

Comparing to Eq. (2.19) we find that the lattice two-point function agrees with the continuum two-point function as $a \rightarrow 0$, i.e. taking the continuum limit.

2.2.2 Lattice gauge fields

In the above section, we provide the construction of free quark fields on the lattice. However, in reality the gauge fields $A_\mu(x)$ have to be considered as they mediate the interactions between quarks. More specifically, a quark moving from site x to y in presence of a gauge fields $A_\mu(x)$ picks up a phase factor given by the path ordered product

$$\psi(y) = \mathcal{P} \exp \left\{ \int_x^y A_\mu(x) dx_\mu \right\} \psi(x). \quad (2.29)$$

The quantity

$$U(x, y) = \mathcal{P} \exp \left\{ \int_x^y A_\mu(x) dx_\mu \right\}, \quad (2.30)$$

is called the *parallel transporter*. It has been Wilson's fundamental observation that the parallel transporter can be used to define the gauge degrees of freedom on the lattice. To illustrate this, we consider for the QCD relevant SU(3) gauge transformations $\Lambda(x)$, which acts on the quark and gauge fields as follows

$$\begin{aligned} \psi(x) &\rightarrow \Lambda(x)\psi(x), \quad \Lambda(x) \in SU(3) \\ U(x, y) &\rightarrow \Lambda(x)U(x, y)\Lambda(y)^{-1}. \end{aligned} \quad (2.31)$$

In particular, for any closed curve \mathcal{C} starting from x and ending at $y = x$, the gauge transformation is

$$U(x, x; \mathcal{C}) \rightarrow \Lambda(x)U(x, x; \mathcal{C})\Lambda(x)^\dagger. \quad (2.32)$$

This means that a *Wilson loop* $W(\mathcal{C}) \equiv \text{tr} \{U(x, x; \mathcal{C})\}$ is in fact gauge-invariant under such transformations, given the cyclicity of the trace operation.

On the lattice, one makes use of the concept of the parallel transporter and defines the *link variable* $U_\mu(x) \equiv U(x, x + a\hat{\mu})$, pointing from x to its nearest neighbor in the μ direction

$$U_\mu(x) \in \text{SU}(3) , \quad U_\mu(x) \rightarrow \Lambda(x)U_\mu(x)\Lambda(x + a\hat{\mu})^{-1} . \quad (2.33)$$

For $a \rightarrow 0$, $U_\mu(x)$ can be represented as

$$U_\mu(x) = 1 + aA_\mu(x) + O(a^2) . \quad (2.34)$$

A Wilson loop $W(\mathcal{C})$ constructed from such link variables is still gauge invariant. The two simplest Wilson loops on the lattice are the plaquette ($\square_{1 \times 1}$) and the rectangle ($\square_{1 \times 2}$), from which one builds the so-called plaquette fields

$$P_{\mu\nu}(x) = \text{Re Tr} \{1 - U(x, x; \square_{1 \times 1})\} \quad (2.35)$$

and rectangle fields

$$R_{\mu\nu}(x) = \text{Re Tr} \{1 - U(x, x; \square_{1 \times 2})\} . \quad (2.36)$$

The introduction of the link fields allows in particular to define a gauge covariant forward and backward difference lattice operator

$$\begin{aligned} \nabla_\mu \psi(x) &= \frac{1}{a} \{U_\mu(x)\psi(x + a\hat{\mu}) - \psi(x)\} \\ \nabla_\mu^* \psi(x) &= \frac{1}{a} \left\{ \psi(x) - U_\mu^\dagger(x - a\hat{\mu})\psi(x - a\hat{\mu}) \right\} \\ \nabla_\mu \psi(x) &\rightarrow \Lambda(x)\nabla_\mu \psi(x) , \quad \nabla_\mu^* \psi(x) \rightarrow \Lambda(x)\nabla_\mu^* \psi(x) . \end{aligned} \quad (2.37)$$

As a consequence, based on the definition (2.37), a gauge-covariant Wilson operator can be constructed which reads

$$D_W + m_0 = \sum_{\mu=0}^3 \frac{1}{2} \{ \gamma_\mu (\nabla_\mu^* + \nabla_\mu) - ar \nabla_\mu^* \nabla_\mu \} + m_0 , \quad (2.38)$$

where m_0 is the bare quark mass parameter.

2.3 Lattice QCD action – Wilson action

The fundamental degrees of freedom of QCD are quark and gauge fields. Using the quark and gauge fields introduced in Sect. 2.2.1 and 2.2.2, one can construct the Lattice QCD

action. Early in 1974, the so-called Wilson action, for both quark and gauge fields, was developed [33]

$$\begin{aligned}
\mathcal{S} &= \mathcal{S}_G + \mathcal{S}_F \\
\mathcal{S}_G &= \frac{\beta}{3} \sum_x \sum_{\mu\nu} P_{\mu\nu}(x) , \quad \beta \equiv 6/g_0^2 \\
\mathcal{S}_F &= a^4 \sum_x \bar{\psi}(x) (D_W + m_0) \psi(x) .
\end{aligned} \tag{2.39}$$

This action is gauge-invariant for any lattice spacing. In other words, it is unaffected by a local gauge transformation in which the fermion and gauge fields are rotated by SU(3) group elements $\Lambda(x)$ defined at each point.

A more general form of gauge action is given by

$$\mathcal{S}_G = \frac{\beta}{3} \sum_x \sum_{\mu\nu} (b_0 P_{\mu\nu}(x) + b_1 R_{\mu\nu}(x)) \tag{2.40}$$

with normalization condition $b_0 = 1 - 8b_1$. Note that at $b_1 = 0$ this action becomes the usual Wilson plaquette gauge action. For $b_1 = -1.4088$, the action is so-called DBW2 gauge action [45] and for $b_1 = -1/12$ it is the tree-level Symanzik improved gauge action [46]. Tuning the coefficient b_1 , one expects to accelerate the convergence to the continuum limit.

We give this generalized form of the gauge action here, since this will be used later on in the numerical simulations for the generation of the gauge field configurations on which our physical quantities are evaluated.

In Wilson's fermionic action \mathcal{S}_F , the Wilson term protects from the existence of doublers in the continuum limit but it breaks chiral symmetry at $\mathcal{O}(a)$. Besides, the quark mass m_0 renormalizes both additively and multiplicatively. Hence, an $\mathcal{O}(1/a)$ counter term needs to be introduced to compensate the additive quark mass renormalization. It is useful and common to define a *subtracted bare mass* m_q by

$$m_q = m_0 - m_{\text{crit}} , \tag{2.41}$$

where m_{crit} is called the *critical mass parameter*. This leads to a fine tuning problem in Wilson Lattice QCD as the value of the Lagrangian parameter m_0 has to be adjusted very carefully to reach the chiral limit.

2.3.1 Computation of correlation functions

The partition function of the Wilson action can be expressed as

$$\mathcal{Z} = \int \mathcal{D}U \mathcal{D}\psi \mathcal{D}\bar{\psi} e^{-\mathcal{S}_G[U]} e^{-\bar{\psi} M \psi}, \quad (2.42)$$

where $M = D_W + m$ is the so-called *fermion matrix*. The integral over the fermion fields can be solved by using the usual integration rules of Grassmann variables [47]

$$\int \mathcal{D}\psi \mathcal{D}\bar{\psi} e^{-\bar{\psi} M \psi} \propto \det M. \quad (2.43)$$

The partition function is then given by

$$\mathcal{Z} = \int \mathcal{D}U \det M [U] e^{-\mathcal{S}_G[U]} = \int \mathcal{D}U e^{-\mathcal{S}_G[U] + \log \det M [U]} = \int \mathcal{D}U e^{-\mathcal{S}_{\text{eff}}[U]}, \quad (2.44)$$

where we have introduced the *effective gauge action* as

$$\mathcal{S}_{\text{eff}} [U] \equiv \mathcal{S}_G [U] - \log \det M [U] = \mathcal{S}_G [U] - \text{Tr} \log M [U]. \quad (2.45)$$

Any expectation value of a physical observable $\langle \mathcal{O} \rangle$, e.g. the correlation functions, can be computed in the path integral formalism as

$$\langle \mathcal{O} \rangle = \frac{1}{\mathcal{Z}} \int \mathcal{D}U \mathcal{D}\psi \mathcal{D}\bar{\psi} \mathcal{O} [U, \bar{\psi}, \psi] e^{-\mathcal{S}_G[U]} e^{-\bar{\psi} M \psi}. \quad (2.46)$$

After performing the Grassmann integral, it becomes a function depending only on gauge variables

$$\langle \mathcal{O} \rangle = \frac{1}{\mathcal{Z}} \int \mathcal{D}U \mathcal{O} [U] \det M [U] e^{-\mathcal{S}_G[U]} = \frac{1}{\mathcal{Z}} \int \mathcal{D}U \mathcal{O} [U] e^{-\mathcal{S}_{\text{eff}}[U]} \quad (2.47)$$

In practise, the above expectation value is evaluated as an ensemble average over gauge fields that are chosen according to the probability distribution given by

$$\rho[U] = e^{-\mathcal{S}_{\text{eff}}[U]}. \quad (2.48)$$

The details of the numerical simulation aspects to generate the above probability distribution can be found in [35–38]. For this thesis, we just assume that the gauge fields have been generated with a suitable numerical method and we will only employ them to compute the correlation functions of interest.

2.3.2 Continuum limit and Symanzik's improvement program

A very important aspect of lattice simulations is the approach to the continuum limit, i.e. the process of removing the initial lattice discretization and sending the lattice spacing a to zero. The continuum QCD Lagrangian can be obtained by an expansion of the Wilson action in the lattice spacing a ,

$$\begin{aligned}\mathcal{S}_G &\rightarrow \frac{1}{4} \int d^4x (F_{\mu\nu})^2 + O(a^2), & F_{\mu\nu} &= \partial_\mu A_\nu - \partial_\nu A_\mu + ig_0 [A_\mu, A_\nu] \\ \mathcal{S}_F &\rightarrow \bar{\psi} (\gamma_\mu D_\mu + m) \psi + O(a), & D_\mu &= \partial_\mu + igA_\mu.\end{aligned}\tag{2.49}$$

The expression in eq. (2.49) shows that the leading order correction to the Wilson gauge action is $O(a^2)$, while the fermion action suffers from larger lattice artifacts which appear at $O(a)$. We note in passing that the appearance of the lattice artifacts at $O(a)$ is related to the explicit breaking of chiral symmetry when using Wilson fermions. To reduce the lattice artifacts, we could, of course, perform calculations using small values of the lattice spacing, such that one is close enough to the continuum limit. However, the computational costs increase dramatically when decreasing a .

A better solution is to make use of the fact that the lattice formulation of the QCD action is not unique. Alternative versions of lattice actions leading to the same continuum action as the lattice spacing $a \rightarrow 0$ are equally valid. Improved lattice actions with smaller lattice spacing artifacts can be systematically developed by means of Symanzik's improvement program [48–50]. In this concept the lattice theory at finite values of a is mapped to an effective continuum theory,

$$\mathcal{S}_L = \mathcal{S}_C + a\mathcal{S}_1 + a^2\mathcal{S}_2 + \dots.\tag{2.50}$$

where \mathcal{S}_L and \mathcal{S}_C denote the lattice and continuum action. The correction terms \mathcal{S}_i correspond to continuum operators. Similarly, the operators used to probe physics can be expanded as

$$\mathcal{O}_L = \mathcal{O}_C + a\mathcal{O}_1 + a^2\mathcal{O}_2 + \dots.\tag{2.51}$$

Lattice expectation values are then given by the corresponding continuum expectation value

plus correction terms which are proportional to powers of the lattice spacing

$$\langle \mathcal{O}_L \rangle_{\text{latt}} = \langle \mathcal{O}_C \rangle_{\text{cont}} - a \langle \mathcal{O}_C \mathcal{S}_1 \rangle_{\text{cont}} + a \langle \mathcal{O}_1 \rangle_{\text{cont}} + O(a^2) . \quad (2.52)$$

The advantage of the Symanzik's improvement programme is that the correction terms \mathcal{S}_i and \mathcal{O}_i carry coefficients which can be computed in such a way that, e.g. the $\mathcal{O}(a)$ effects can be canceled. Such a computation has to be performed non-perturbatively and involves a large set of simulations. Nevertheless for the action itself and a number of operators this has indeed be performed [51]. One point to notice here is that in order to improve a physical expectation value to any given order in a , one has to improve both the action and the operators to the same order, unless the physical quantity is derived from the action it self, e.g. in the case of hadron masses. Thus, to establish a complete $\mathcal{O}(a)$ -improvement for many physical quantities of interest is a very demanding task.

2.4 Lattice QCD action – Wilson twisted mass action

Another way to achieve an $\mathcal{O}(a)$ -improvement of the lattice theory is to discretize the theory with Wilson twisted mass fermions taken at so-called *maximal twist*, as explained in this section. Indeed, all calculations reported in this thesis are based on two dynamical flavors maximally twisted mass QCD action. The gauge action used in our calculations is given in Eq. (2.40) and will not be discussed further. In the following, we will concentrate on the properties of the twisted mass fermion action and, in particular, how the wanted $\mathcal{O}(a)$ -improvement can be achieved.

2.4.1 Twisted mass fermion action

The twisted mass fermion action for two flavor mass degenerate quarks is introduced by adding a twisted mass term $i\mu\gamma_5\tau_3$ to the standard Wilson fermion action

$$\mathcal{S}_{tm} = a^4 \sum_x \bar{\chi}(x) [D_W + m_0 + i\mu\gamma_5\tau_3] \chi(x) = a^4 \sum_x \bar{\chi}(x) D_{tm} \chi(x) . \quad (2.53)$$

The twisted mass parameter μ serves as an infrared cutoff for the eigenvalues of the operator D_{tm}

$$\det [D_{tm}] = \det [D_W^2 + \mu^2] . \quad (2.54)$$

Thus the formulation avoids un-physically, so-called exceptional, small eigenvalues of the Wilson lattice Dirac operator which may lead to severe problems in the numerical simulations [52, 53].

In the continuum limit, the twisted mass fermion action reads as

$$\mathcal{S}_{tm} = \int d^4x \bar{\chi}(x) [\gamma_\mu D_\mu + m_q + i\mu\gamma_5\tau_3] \chi(x) \quad (2.55)$$

where the mass term can be rewritten as

$$m_q + i\mu\gamma_5\tau_3 \equiv M e^{i\alpha\gamma_5\tau_3}, \quad M = \sqrt{m_q^2 + \mu^2}, \quad \alpha = \arctan\left(\frac{\mu}{m_q}\right). \quad (2.56)$$

The form (2.55) can be obtained from the standard continuum fermion action

$$\mathcal{S} = \bar{\psi} [\gamma_\mu D_\mu + M] \psi \quad (2.57)$$

by an axial transformation

$$\psi \rightarrow e^{i\omega\gamma_5\tau_3/2} \chi, \quad \bar{\psi} \rightarrow \bar{\chi} e^{i\omega\gamma_5\tau_3/2}. \quad (2.58)$$

for a particular choice of the twist angle, namely $\omega = \alpha$. Since the transition from the standard to the twisted form of the action corresponds only to a change of fermionic variables leaving also the measure invariant, the physics remains completely un-altered when using the generalized form of the action with the twisted mass term included. In the following we call the basis $\{\bar{\chi}, \chi\}$ the twisted and $\{\bar{\psi}, \psi\}$ the physical basis.

A particularly interesting choice of the twisted mass fermion action, in particular when using twisted mass fermions on the lattice as we will see later, is the case with $m_q = 0$

$$\mathcal{S}_{tm} = \int d^4x \bar{\chi}(x) [\gamma_\mu D_\mu + i\mu\gamma_5\tau_3] \chi(x), \quad (2.59)$$

which can be achieved from the standard continuum action by using the twisting angle $\omega = \alpha = \pi/2$. This is referred to as the action at maximal twist.

2.4.2 O(a) improvement

The lattice Wilson twisted mass action (2.53) in the twisted mass basis can be translated into the physical basis by an axial transformation (2.58)

$$\mathcal{S}_{tm}^{ph} = a^4 \sum_x \bar{\psi}(x) e^{-i\omega\gamma_5\tau_3/2} [D_W + m_0 + i\mu\gamma_5\tau_3] e^{-i\omega\gamma_5\tau_3/2} \psi(x). \quad (2.60)$$

By replacing bare quark mass with critical mass and subtracted mass: $m_0 = m_{\text{crit}} + m_q$, the action reads

$$\mathcal{S}_{tm}^{ph} = a^4 \sum_x \bar{\psi}(x) \left[\frac{1}{2} \sum_{\mu} \gamma_{\mu} (\nabla_{\mu}^* + \nabla_{\mu}) + \left(-r \frac{a}{2} \sum_{\mu} \nabla_{\mu}^* \nabla_{\mu} + m_{\text{crit}} \right) e^{-i\omega \gamma_5 \tau_3} + M \right] \psi(x). \quad (2.61)$$

In order to proceed, we first remark that the critical mass is an odd function of the Wilson parameter r [28]

$$m_{\text{crit}}(-r) = -m_{\text{crit}}(r). \quad (2.62)$$

Using this fact, it can be shown that the action (2.61) is invariant under the combined transformation $\tilde{\mathcal{R}}_5$

$$\tilde{\mathcal{R}}_5 = \mathcal{R}_5 \times (r \rightarrow -r) \times (M \rightarrow -M), \quad (2.63)$$

where \mathcal{R}_5 is defined as

$$\mathcal{R}_5 : \begin{cases} \psi \rightarrow \psi' = \gamma_5 \psi \\ \bar{\psi} \rightarrow \bar{\psi}' = -\bar{\psi} \gamma_5 \end{cases}. \quad (2.64)$$

In this situation, it is proved that any multiplicatively renormalizable (m.r.) operator \mathcal{O} will be either even or odd under the parity transformation $\tilde{\mathcal{R}}_5$ which we express as $(-1)^{P_{\mathcal{R}_5}[\mathcal{O}]}$. The argument implies that the expectation value of \mathcal{O} must satisfy the relation

$$\langle \mathcal{O} \rangle|_{(r,M)} = (-1)^{P_{\mathcal{R}_5}[\mathcal{O}]} \langle \mathcal{O} \rangle|_{(-r,-M)}. \quad (2.65)$$

Making use of the Symanzik expansion and relation (2.65), it is proved in Ref. [28] that the Wilson average of an expectation value $\langle \mathcal{O} \rangle$ is $O(a)$ improved

$$\frac{1}{2} \left[\langle \mathcal{O} \rangle|_{(r,M)} + \langle \mathcal{O} \rangle|_{(-r,M)} \right] = \zeta(r) \langle \mathcal{O} \rangle|_M^{\text{cont}} + O(a^2). \quad (2.66)$$

In Eq. (2.66), the change of the Wilson parameter $r \rightarrow -r$ is equivalent to the change of $\omega \rightarrow \omega + \pi$. A particular choice is the maximal twist of $\omega = -\pi/2$, which is achieved by tuning m_0 to be m_{crit} since

$$m_q = m_0 - m_{\text{crit}} = 0 \rightarrow \omega = \arctan\left(\frac{\mu}{m_q}\right) = \pm\pi/2. \quad (2.67)$$

Thus it is proved that, at maximal twist, any quantity invariant under $\omega = \pm\pi/2$ is automatic $O(a)$ -improved. In this thesis, we could give only the basic arguments to demonstrate that twisted mass lattice fermions when taken at maximal twist are $O(a)$ -improved. For a detailed proof of this fact, we refer the readers to Ref. [28].

2.4.3 Isospin symmetry breaking

As mentioned above, the twisted mass fermion matrix protects against small eigenvalues, achieves automatic $O(a)$ improvement at maximal twist. It is also expected to simplify mixing problems in the renormalization process needed for a number of physical observables [28]. At the same time, its computational cost is comparable to standard Wilson fermions. The expense of having these good properties is that at non-zero lattice spacing, the twisted mass term explicitly breaks the full $SU(2)$ flavor symmetry down to $U(1)$, the conserved I_3 , but not I^2 , symmetry. A direct result of isospin symmetry breaking is that the neutral pion mass becomes smaller than the charged ones, and unphysical parity-breaking interactions among pions become possible.

This observation is especially relevant for this thesis since such isospin symmetry breaking effects could in principle contaminate pion-pion scattering as investigated here. Let us sketch here the mechanism of how this can appear. On the lattice, one determines the scattering phase for two-pion systems with Lüscher's method, by determining the interaction energy

$$\Delta E_{\pi\pi} = E_{\pi\pi} - 2m_{\pi} . \quad (2.68)$$

In the isospin zero limit, the $|I, I_3\rangle = |2, 0\rangle$ and $|0, 0\rangle$ states are given by

$$\begin{aligned} |2, 0\rangle &= \frac{1}{\sqrt{6}} (|\pi^+\pi^-\rangle + |\pi^-\pi^+\rangle - 2|\pi^0\pi^0\rangle) , \\ |0, 0\rangle &= \frac{1}{\sqrt{3}} (|\pi^+\pi^-\rangle + |\pi^-\pi^+\rangle + |\pi^0\pi^0\rangle) , \end{aligned} \quad (2.69)$$

including both neutral and charged pions. As said above, the isospin breaking leads to a particular lattice artifact in that the charged and neutral pion masses have different masses, in contrast to e.g. standard Wilson fermions where they are mass-degenerate. It turns out

in practical simulations [29] that this mass splitting is sizable. As a consequence, there is also a splitting in the energy shift $\Delta E_{\pi\pi}$ which can be either $E_{\pi\pi} - 2m_{\pi}^0$ or $E_{\pi\pi} - 2m_{\pi}^+$.

Furthermore, since I^2 is no longer a good quantum number, the two states in Eq. (2.69) do not carry definite isospin I anymore and they mix. A very important point is that the unphysical states that mix have lattice artifacts that appear at $\mathcal{O}(a)$. Hence, for these quantities the lattice artifacts can easily become sizable and need to be studied very carefully.

To deal with this problem, one needs to treat the combined states

$$|I, 0\rangle = \begin{pmatrix} |2, 0\rangle \\ |1, 0\rangle \end{pmatrix}, \quad (2.70)$$

which turns the pion-pion scattering to be a two-channel scattering process and a very complex analysis for the determination of the scattering matrix is required.

To avoid this complexity, we study the $\pi^+\pi^+$ scattering system with definite quantum number $I_3 = +2$ only. Since $I_3 = +2$ is already the maximal value, there is only one possible state $|2, +2\rangle$ allowed. Thus the mixing problem is avoided. Moreover, the scattering state can only consist of two charged pions leading to a unique value of the energy shift $\Delta E_{\pi\pi}$.

In the process of the $I = 1$ pion-pion scattering channel, in which the rho resonance appears, the possible mixing between different isospin states can also happen. We will therefore perform the calculations at different lattice spacings to explicitly check for any strong lattice artifacts for $I = 1$.

CHAPTER III

FINITE SIZE METHODS

As discussed in Sect. 2.1, LQCD allows us to directly extract the energy spectrum of a two-particle scattering system from the computation of the corresponding Euclidean correlation functions. However, when working in a finite box, it is not obvious how then the discrete energy spectrum can be related to experimentally interesting physical quantities such as a cross section or a scattering phase. To fill this gap, M. Lüscher developed a particular finite size method (FSM) which connects the scattering phase in infinite volume to the discrete energy spectrum in a finite box.

In this thesis, we will concentrate on calculations of the discrete energy spectrum related to pion-pion scattering in different isospin channels. In the $I = 2$ channel, the large Euclidean time limit yields a pion-pion ground state with energy

$$E_{\pi\pi}^{I=2} = 2m_\pi + \delta E = \sqrt{m_\pi^2 + \vec{p}^2} + \sqrt{m_\pi^2 + (-\vec{p})^2}. \quad (3.1)$$

As indicated in the following section, the energy shift δE appears at $O(1/L^3)$ in the lattice size, L . Therefore, it is allowed to extract the S-wave scattering length from the low relative momentum $p \sim L^{-3/2}$ expansion of the corresponding scattering phase $\delta_0(p)$ for a large lattice size L . In the $I = 1$ channel, due to the parity conservation, the wave function of a pion-pion state here is an odd function of the relative momentum. Consequently, the S-wave scattering amplitude vanishes and the ρ -meson appears in the dominant P-wave. Our target is to determine the ρ resonance parameters. i.e. the resonance mass and the decay width. Employing the FSM, we will calculate the scattering phase at different discrete energies with the aim to scan the resonance region. Clearly, the more scattering phases are calculated, the better the resonant behavior of the scattering phase can be mapped out. One method is to study $I = 1$ pion-pion scattering using different lattice sizes, which, however, requires substantial simulation efforts especially at large lattice sizes. An alternative way

is to use the moving frame (MF) technique provided by Rummukainen and Gottlieb [54], which generalizes Lüscher's original FSM from the center-of-mass frame (CMF) to the MF. The important point is that the energy spectrum calculated in the MF is different from the one obtained in the CMF. Thus combining the CMF and the MF allows to compute many scattering phases using the same lattice size and hence will increase the accuracy of the calculation of the desired resonance parameters.

In Ref. [54], the exact formulae to calculate the $I = 1$ pion-pion scattering phase for the MF with total momentum $\vec{P} = (2\pi/L)\vec{e}_3$ (MF1) are given. In our work, in addition to the CMF and the MF1, we further employ a second MF with $\vec{P} = (2\pi/L)(\vec{e}_1 + \vec{e}_2)$ (MF2). Note that the corresponding finite size formulae are not available in the literature and their derivation is part of this thesis.

The aim of this chapter is to explain how the connection between the scattering phase in the infinite volume and the energy spectrum in a finite box is established. In addition, we will provide the detailed expressions of the finite size formulae associated with the CMF, MF1 and MF2, which are used to calculate the pion-pion scattering phase. To introduce the FSM, our starting point is a Quantum Mechanical scattering system where we introduce the relevant finite size formulae. It is amazing that the same finite size formulae hold also in Quantum field theories. The prove of this statement, as established in Ref. [24], can be considered as a main theoretical breakthrough since it opens the path to compute scattering phenomena in lattice field theory in principle.

3.1 Scattering in the infinite volume

Following Ref. [24], let us consider two spinless bosons with mass m in the CMF and assume that the effective potential $V(r)$ describes the interaction between the two particles. The Hamiltonian operator \hat{H} is then taken to be

$$\hat{H} = -\frac{\nabla^2}{2\mu} + V(r), \quad r = |\vec{r}| = |\vec{x}_1 - \vec{x}_2|. \quad (3.2)$$

where $\mu = m/2$ is the reduced mass of the two-particle system, the vector \vec{r} indicates the relative position, and \vec{x}_1 and \vec{x}_2 are the spatial positions of the particles. If the interaction

is short-ranged, then the potential $V(r)$ becomes trivial for large distance r ,

$$V(r) = 0, \quad \text{for } r > R, \quad (3.3)$$

where R denotes the interaction range between two particles.

The wave function $\phi(\vec{r})$, which describes the eigenstate of the scattering system, is the solution of the Schrödinger Equation

$$\hat{H}\phi(\vec{r}) = E\phi(\vec{r}). \quad (3.4)$$

The large distance behavior of the wave function reads as

$$\phi(\vec{r}) \xrightarrow{r \rightarrow \infty} (2\pi)^{-3/2} \left\{ \exp(i\vec{p} \cdot \vec{r}) + A(p, \Omega) \frac{\exp(ipr)}{r} \right\}, \quad (3.5)$$

where the momentum \vec{p} is related to the energy E through the non-relativistic dispersion relation $\vec{p}^2 = 2\mu E$. Eq. (3.5) shows that, at large \vec{r} , the wave function of the scattering state can be expanded into two parts: the plain and the spherical wave function. In the case of a non-interacting two particle system, $\phi(\vec{r})$ is solely a plain wave function. This means in turn that all information on the interaction itself is contained in the spherical wave part and, more specifically, in the coefficient, $A(p, \Omega)$, which is referred to as the *scattering amplitude*, where Ω denotes the solid angle of \vec{r} .

The quantity of interest for experiments is the *differential cross section*, $d\sigma/d\Omega$, which is related to the scattering amplitude through

$$\frac{d\sigma}{d\Omega} = |A(p, \Omega)|^2. \quad (3.6)$$

According to a partial wave analysis, the wave function $\phi(\vec{r})$ can be expanded in terms of spherical harmonics $Y_{lm}(\theta, \varphi)$. In Eq. (3.5), the plane wave function then reads

$$\exp(i\vec{p} \cdot \vec{r}) = \sum_{l,m} 4\pi i^l j_l(pr) Y_{lm}^*(\theta_p, \varphi_p) Y_{lm}(\theta, \varphi) \quad (3.7)$$

where l indicates the angular momentum and $j_l(pr)$ denotes the spherical Bessel function.

The coefficient of the spherical wave function is expanded as

$$A(p, \Omega) = \sum_{l,m} 4\pi A_l(p) Y_{lm}^*(\theta_p, \varphi_p) Y_{lm}(\theta, \varphi) \quad (3.8)$$

where $A_l(p)$ is the *partial-wave amplitude*, related to the scattering phase $\delta_l(p)$ as

$$A_l(p) = \frac{\exp(2i\delta_l(p)) - 1}{2ip} = \frac{\exp(i\delta_l(p)) \sin \delta_l(p)}{p}. \quad (3.9)$$

Hence, we have established a link between the scattering phase $\delta_l(p)$, the scattering amplitude $A(p, \Omega)$ and the differential cross section $d\sigma/d\Omega$. Thus, computing the scattering phase, as it is possible on the lattice using the FSM, enables us to directly obtain information on the interaction details of the system under consideration.

For $r > R$, the potential vanishes and $\phi(\vec{r})$ is the solution of Helmholtz equation

$$-\frac{\nabla^2}{2\mu}\phi(\vec{r}) = E\phi(\vec{r}), \quad (3.10)$$

and thus can be expressed in terms of spherical harmonics and spherical Bessel functions

$$\phi(r) = \sum_{l,m} b_{lm} (\alpha_l(p)j_l(pr) + \beta_l(p)n_l(pr)) Y_{lm}(\theta, \varphi) \quad (3.11)$$

for some known constants b_{lm} . Note that the spherical Bessel functions $j_l(pr)$ and $n_l(pr)$ have asymptotical forms for $r \rightarrow \infty$ as

$$\begin{aligned} j_l(pr) &\rightarrow \frac{\sin(pr - \frac{l\pi}{2})}{pr}, & n_l(pr) &\rightarrow -\frac{\cos(pr - \frac{l\pi}{2})}{pr}, \\ j_l(pr) + in_l(pr) &\xrightarrow{r \rightarrow \infty} \frac{i^{l-1} \exp(ipr)}{pr}. \end{aligned} \quad (3.12)$$

We therefore make a comparison between Eq. (3.11) and (3.5), from which we find that the amplitudes $\alpha_l(p)$ and $\beta_l(p)$ are related to the scattering phase $\delta_l(p)$ through

$$\exp(2i\delta_l(p)) = \frac{\alpha_l(p) + i\beta_l(p)}{\alpha_l(p) - i\beta_l(p)}, \quad \text{or} \quad \tan \delta_l(p) = \frac{\beta_l(p)}{\alpha_l(p)}. \quad (3.13)$$

As $p \rightarrow 0$ the scattering phase $\delta_l(p)$ can be expanded as

$$\delta_l(p) = \nu_l \pi + a_l p^{2l+1} + O(p^{2l+3}) \quad (3.14)$$

for some integer ν_l , which denotes the *modulo π ambiguity* in $\delta_l(p)$ [55]. In the case of S-wave scattering, a_0 is the so-called *scattering length*, which determines the leading low-energy behavior of the scattering phase $\delta_0(p)$

$$p \tan^{-1} \delta_0(p) = a_0^{-1} + \frac{1}{2} r_{\text{eff}} p^2 + O(p^4), \quad (3.15)$$

where the coefficient r_{eff} is the *effective range parameter* which determines the next leading order behavior of $\delta_0(p)$. In Eq. (3.15), the ambiguity ν_0 is removed by the tan function.

In our work, we will use Eq. (3.15) to relate the scattering phase at sufficiently small momentum p to the scattering length which is the target of our calculation in the $I = 2$ channel of pion-pion scattering.

3.2 Scattering in a finite box

In Lattice QCD calculations, we consider the pion-pion scattering system in a finite box with box size L . As a consequence, we have to introduce some boundary condition. If we choose periodic boundary conditions, the finite box potential $V_L(\vec{r})$, describing the particle interaction, satisfies in the CMF

$$V_L(\vec{r}) = \sum_{\vec{n} \in \mathbf{Z}^3} V(|\vec{r} + \vec{n}L|). \quad (3.16)$$

The finite box Hamiltonian operator \hat{H}_L is constructed as

$$\hat{H}_L = -\frac{\nabla^2}{2\mu} + V_L(r) \quad (3.17)$$

with $\mu = m/2$ the reduced mass of the system. The wave function $\phi_L(\vec{r})$ is the solution of the Schrödinger equation, satisfying

$$\hat{H}_L \phi_L(\vec{r}) = E(L) \phi_L(\vec{r}), \quad (3.18)$$

and

$$\phi_L(\vec{r} + \vec{n}L) = \phi_L(\vec{r}), \quad \text{for all } \vec{n} \in \mathbf{Z}^3. \quad (3.19)$$

Due to the periodic boundary condition, the energy spectrum $E(L)$ of the scattering system is now discrete and related to the lattice size L .

Assume that the box is large enough compared to the interaction range R , say $L/2 > R$, to avoid significantly altering the two pion interaction. We can define the *exterior region*

$$\Omega = \{ \vec{r} \in \mathbf{R}^3 \mid |\vec{r} + \vec{n}L| > R \text{ for all } \vec{n} \in \mathbf{Z}^3 \} \quad (3.20)$$

where the potential $V_L(\vec{r})$ vanishes and the wave function $\phi_L(r)$ satisfies the Helmholtz equation

$$(\nabla^2 + p^2) \phi_L(r) = 0. \quad (3.21)$$

In Eq. (3.21), the momentum p is given by the non-relativistic dispersion relation $p^2 = 2\mu E(L)$ within the framework of Quantum Mechanics.

To solve the solution of the Helmholtz equation, one introduces the Green function

$$G(\vec{r}; p^2) = L^{-3} \sum_{\vec{k} \in \Gamma} \frac{\exp(i\vec{k} \cdot \vec{r})}{k^2 - p^2}, \quad (3.22)$$

where the sum runs over the lattice momenta

$$\Gamma = \left\{ \vec{k} \in \mathbf{R}^3 \left| \vec{k} = \frac{2\pi}{L} \vec{n} \text{ for some } \vec{n} \in \mathbf{Z}^3 \right. \right\}. \quad (3.23)$$

The Green function is a singular periodic solution of the Helmholtz equation

$$(\nabla^2 + p^2) G(\vec{r}, p^2) = - \sum_{\vec{n} \in \mathbf{Z}^3} \delta(\vec{r} + \vec{n}L). \quad (3.24)$$

Any further singular periodic solutions $G_{lm}(\vec{r}; p^2)$ can be generated from this Green function by introducing the harmonic polynomials

$$\mathcal{Y}_{lm}(\vec{r}) = r^l Y_{lm}(\theta, \varphi), \quad (3.25)$$

and defining

$$G_{lm}(\vec{r}, p^2) = \mathcal{Y}_{lm}(\vec{\nabla}) G(\vec{r}, p^2). \quad (3.26)$$

Thus, the general solution of the Helmholtz equation, $\phi_L(\vec{r})$, can be formed by a linear combination of $G_{lm}(\vec{r}; p^2)$

$$\phi_L(\vec{r}) = \sum_{l,m} \nu_{lm} G_{lm}(\vec{r}, p^2). \quad (3.27)$$

To perform a comparison with the wave function in the infinite volume case, we expand the function G_{lm} in terms of spherical harmonics and spherical Bessel functions

$$G_{lm}(\vec{r}, p^2) = \frac{(-1)^l}{4\pi} p^{l+1} \left\{ Y_{lm}(\theta, \varphi) n_l(pr) + \sum_{l', m'} \mathcal{M}_{lm, l'm'}(p) Y_{l'm'}(\theta, \varphi) j_{l'}(pr) \right\}, \quad (3.28)$$

where $\mathcal{M}_{lm,l'm'}(p)$ is given by

$$\mathcal{M}_{lm,l'm'}(p) = \frac{(-1)^l}{\pi^{3/2}} \sum_{j=|l-l'|}^{l+l'} \sum_{s=-j}^j \frac{i^j}{q^{j+1}} C_{lm,js,l'm'} \mathcal{Z}_{js}(1, q^2), \quad q = \frac{pL}{2\pi}. \quad (3.29)$$

The coefficient $C_{lm,js,l'm'}$ is related to the Wigner $3j$ -symbols through

$$C_{lm,js,l'm'} = (-1)^{m'} i^{l-j+l'} \sqrt{(2l+1)(2j+1)(2l'+1)} \\ \times \begin{pmatrix} l & j & l' \\ 0 & 0 & 0 \end{pmatrix} \begin{pmatrix} l & j & l' \\ m & s & -m' \end{pmatrix} \quad (3.30)$$

and the zeta function $\mathcal{Z}_{lm}(1, q^2)$ is given by

$$\mathcal{Z}_{lm}(1, q^2) = \int_0^1 dt e^{tq^2} \sum_{\vec{u} \in \mathbf{Z}^3, \vec{u} \neq 0} i^l \mathcal{Y}_{lm}(-\frac{\pi \vec{u}}{t}) (\frac{\pi}{t})^{3/2} \exp(-\frac{(\pi \vec{u})^2}{t}) \\ + \int_0^1 dt (e^{tq^2} - 1) \frac{1}{\sqrt{4\pi}} \delta_{l0} \delta_{m0} (\frac{\pi}{t})^{3/2} - \pi \delta_{l0} \delta_{m0} \\ + \sum_{\frac{2\pi}{L} \vec{n} \in \Gamma} \frac{\mathcal{Y}_{lm}(\vec{n})}{n^2 - q^2} \exp(-(n^2 - q^2)) \quad (3.31)$$

For the step by step deduction of Eq. (3.28), we refer the reader to Ref. [24].

3.3 Finite size formulae in the center-of-mass frame

Let us pause for a moment and summarize. In infinite volume, at any energy level E , the potential $V(\vec{r})$ determines the wave function $\phi(\vec{r})$ of the scattering state. From the large r behavior of $\phi(\vec{r})$, the scattering phase can then be extracted,

$$V(\vec{r}) \Rightarrow \phi(\vec{r}) \xrightarrow{r \rightarrow \infty} \delta_l(p). \quad (3.32)$$

In a finite box, both the potential $V_L(\vec{r})$ and the wave function $\phi_L(\vec{r})$ are chosen to be periodic. The boundary condition results in a discrete energy spectrum of $E(L)$

$$V_L(\vec{r}) \Rightarrow \phi_L(\vec{r}) \Rightarrow E(L). \quad (3.33)$$

As we have discussed above, at the exterior region, both of the wave function $\phi(\vec{r})$ and $\phi_L(\vec{r})$ can be formed by a linear combination of spherical wave functions, see Eq. (3.11) and

Only when the determinant of the coefficient matrix equals zero, this homogenous system (3.38) has a non-trivial solution,

$$\det \begin{pmatrix} A & M \\ B & \mathbf{1} \end{pmatrix} = 0 \quad \Rightarrow \quad \det (AB^{-1} - M) = 0, \quad (3.40)$$

where the matrix element of AB^{-1} is given by

$$(AB^{-1})_{lm,l'm'} = \frac{\alpha_l(p)}{\beta_l(p)} \delta_{ll'} \delta_{mm'} = (\tan^{-1} \delta_l(p)) \delta_{ll'} \delta_{mm'}. \quad (3.41)$$

In Eq. (3.40), we note that the $AB^{-1} - M$ is an infinitely large matrix. To reduce it to a finite matrix, one introduces the angular momentum cutoff Λ , which can be interpreted as a parameter. By varying the value of Λ , we are able to monitor the influence of the higher scattering phases $\delta_l(p)$. Considering the fact that the higher scattering phases are more suppressed in the low momentum region $\delta_l(p) \sim p^{2l+1}$, one can treat them as perturbations. Particularly, if we only focus on the lowest scattering phase $\delta_0(p)$, we can set $\Lambda = 0$ and then Eq. (3.40) is simplified as

$$\tan^{-1} \delta_0(p) = \frac{\alpha_0(p)}{\beta_0(p)} = \mathcal{M}_{00,00}(p) = (\pi^{3/2}q)^{-1} \mathcal{Z}_{00}(1; q^2), \quad q = \frac{pL}{2\pi}. \quad (3.42)$$

It is important to stress that in the above finite size formulae the detailed expression of the potential is not needed. Therefore, here the derived formulae are universal and independent from the particular form of the interaction considered.

Putting low momentum expansion (3.15) of the scattering phase $\delta_0(p)$ into Eq. (3.42), we have

$$\frac{\sqrt{\pi}}{2} \left(\frac{a_0}{L} \right)^{-1} = \mathcal{Z}_{00}(1; q^2) \quad \Rightarrow \quad q^2 = \mathcal{Z}_{00}^{-1} \left[\frac{\sqrt{\pi}}{2} \left(\frac{a_0}{L} \right)^{-1} \right]. \quad (3.43)$$

Assuming that the lattice size is much larger than the scattering length a_0 , the above equation can be expanded as

$$q^2 = -\frac{1}{\pi} \frac{a_0}{L} \left[1 + c_1 \frac{a_0}{L} + c_2 \left(\frac{a_0}{L} \right)^2 \right] + O(L^{-4}) \quad (3.44)$$

where $c_1 = -2.837297$ and $c_2 = 6.375183$ are numerical constants [22]. Using $q = pL/(2\pi)$,

the energy shift δE is then related to the scattering length a_0 through

$$\begin{aligned}\delta E &= 2\sqrt{m^2 + p^2} - 2m = \frac{p^2}{m} + O(p^4) \\ &= -\frac{4\pi a_0}{mL^3} \left[1 + c_1 \frac{a_0}{L} + c_2 \left(\frac{a_0}{L} \right)^2 \right] + O(L^{-6})\end{aligned}\quad (3.45)$$

Using Eq. (3.45) we can convert a lattice determination of the energy shift, δE , into a calculation of a_0 . The contribution from the effective range r_{eff} in expansion (3.15) appears at $O(L^{-6})$ in Eq. (3.45) and is then neglected from the determination of a_0 .

In Eq. (3.42), the S-wave scattering phase δ_0 appears on the left hand side and the momentum p , or equivalently the discrete energy spectrum $E(L)$, shows up on the right hand side. Hence, we have indeed established a finite size formula (3.42), or more generally (3.40), which serves as a bridge between the physical scattering phase and the discrete energy spectrum on a periodic lattice.

3.4 Generalization to the moving frame

As we have seen, having a finite volume in lattice simulations is not a disadvantage. On the contrary, Lüscher's method makes actually use of the finite box size. Calculations performed on several different volumes can help to determine the scattering phase shift $\delta_l(p)$ at different energies. Particularly, in the determination of the ρ resonance parameters in the process of pion-pion scattering, we need the information of the P-wave scattering phase $\delta_1(p)$ at an energy E close to the resonance peak

$$E = 2\sqrt{m_\pi^2 + p^2} \simeq m_\rho. \quad (3.46)$$

In the non-interacting case, a small momentum p and correspondingly a large lattice size L is needed,

$$\frac{2\pi}{L} = p \simeq \sqrt{m_\rho^2/4 - m_\pi^2}. \quad (3.47)$$

Since simulating with a large physical volume requires very large computer resources, Rummukainen and Gottlieb generalized Lüscher's formalism to the MF [54], where the total momentum of the two particles is non-zero. A simple example of the MF is that one pion

carries the momentum $\vec{p}_1 = (2\pi/L)\vec{e}_3$ while the other stays at rest with $\vec{p}_2 = 0$. We denote this setup as MF1 in this thesis. The total momentum is $\vec{P} = \vec{p}_1 + \vec{p}_2 = (2\pi/L)\vec{e}_3$.

In the MF, the center of mass is moving with velocity $\vec{v} = \vec{P}/(E_1 + E_2)$. The 4-momenta in the CMF, (E_i^*, \vec{p}_i^*) , are related to the 4-momenta (E_i, \vec{p}_i) in the MF through the standard Lorentz transformation

$$E_i^* = \gamma(E_i - \vec{v} \cdot \vec{p}_i), \quad \vec{p}_i^* = \vec{\gamma}(\vec{p}_i - \vec{v}E_i), \quad (3.48)$$

where γ is the Lorentz boost factor

$$\gamma = \frac{1}{\sqrt{1 - \vec{v}^2}} \quad (3.49)$$

and here we use the notation of the operators $\vec{\gamma}$ and $\vec{\gamma}^{-1}$ as

$$\vec{\gamma}\vec{p} = \gamma\vec{p}_{\parallel} + \vec{p}_{\perp}, \quad \vec{\gamma}^{-1}\vec{p} = \gamma^{-1}\vec{p}_{\parallel} + \vec{p}_{\perp}, \quad \vec{p}_{\parallel} = \frac{\vec{p} \cdot \vec{v}}{v^2}\vec{v}, \quad \vec{p}_{\perp} = \vec{p} - \vec{p}_{\parallel}. \quad (3.50)$$

It can then be derived that

$$E_1^* = E_2^* = \frac{1}{2}\gamma^{-1}(E_1 + E_2), \quad \vec{p}_1^* = -\vec{p}_2^* = \frac{1}{2}\vec{\gamma}^{-1}(\vec{p}_1 - \vec{p}_2). \quad (3.51)$$

Thus, one proves that, after a Lorentz transformation from the MF1 to the CMF, the two pions are moving in the opposite direction with momentum $p^* = (2\pi/L)/2\gamma$. The requirement (3.47) is now replaced by

$$\frac{1}{2\gamma} \frac{2\pi}{L} = p^* \simeq \sqrt{m_{\rho}^2/4 - m_{\pi}^2}. \quad (3.52)$$

In the existence of an interaction, the momentum p^* is not simply given by $(2\pi/L)/(2\gamma)$. Nevertheless, the conclusion still holds that, in the process of $\rho \rightarrow \pi\pi$, the avoided level crossing occurs for a smaller lattice size in the MF which helps to reduce the simulation costs.

In the MF with total momentum \vec{P} , the energy E we calculate from Euclidean correlation function is the energy eigenvalue of Hamiltonian operator \hat{H}_L

$$\hat{H}_L|E, \vec{P}\rangle = E|E, \vec{P}\rangle. \quad (3.53)$$

where $|E, \vec{P}\rangle$ is a two-particle scattering state with total 4-momentum (E, \vec{P}) and its wave function is defined as

$$\Psi_L(\vec{x}_1, t; \vec{x}_2, t) = \langle \Omega | \mathcal{O}(\vec{x}_1, t; \vec{x}_2, t) | E, \vec{P} \rangle . \quad (3.54)$$

Here $\mathcal{O}(\vec{x}_1, t; \vec{x}_2, t)$ is a two-particle interpolating operator defined on Euclidean space-time. Restricted by the finite size of the box with periodic boundary condition, $\Psi_L(\vec{x}_1, t; \vec{x}_2, t)$ satisfies

$$\Psi_L(\vec{x}_1 + \vec{n}_1 L, t; \vec{x}_2 + \vec{n}_2 L, t) = \Psi_L(\vec{x}_1, t; \vec{x}_2, t) , \quad \text{for all } \vec{n}_1, \vec{n}_2 \in \mathbf{Z}^3 . \quad (3.55)$$

By changing the variables

$$\vec{X} = \frac{\vec{x}_1 + \vec{x}_2}{2} , \quad \vec{r} = \vec{x}_1 - \vec{x}_2 , \quad (3.56)$$

we separate the wave function Ψ_L into two parts

$$\Psi_L(\vec{x}_1, t; \vec{x}_2, t) = e^{-Et + i\vec{P} \cdot \vec{X}} \phi_L(\vec{r}) . \quad (3.57)$$

Eq. (3.55) and (3.57) together yield the so-called \vec{d} -periodic boundary condition [54]

$$\phi_L(\vec{r}) = (-1)^{\vec{d} \cdot \vec{n}} \phi_L(\vec{r} + \vec{n}L) , \quad (3.58)$$

with the vector $\vec{d} = \vec{P}L/(2\pi)$. To establish the formula for the scattering phase, which is only defined in the CMF, we need to transform the scattering system in the MF to the one in the CMF using the Lorentz boost

$$\begin{aligned} (E, \vec{P}) &\rightarrow (E_{CM}, \vec{0}) \\ \phi_L(\vec{r}) &\rightarrow \phi_{L,CM}(\vec{r}) \end{aligned} \quad (3.59)$$

where E_{CM} is the total energy in the CMF with $E_{CM} = \gamma^{-1}E = \sqrt{E^2 - \vec{P}^2}$ and the wave function $\phi_{L,CM}(\vec{r})$ satisfies the boundary condition

$$\phi_{L,CM}(\vec{r}) = (-1)^{\vec{d} \cdot \vec{n}} \phi_{L,CM}(\vec{r} + \vec{\gamma} \vec{n}L) , \quad \text{for all } \vec{n} \in \mathbf{Z}^3 . \quad (3.60)$$

Any wave function with momentum p , given by dispersion relation $E_{CM} = 2\sqrt{m^2 + p^2}$ and boundary condition (3.60) can be generated from the following Green function

$$G^{\vec{d}}(\vec{r}, p^2) = \gamma^{-1} L^{-3} \sum_{\vec{k} \in \Gamma^{\vec{d}}} \frac{e^{i\vec{k} \cdot \vec{r}}}{k^2 - p^2} , \quad (3.61)$$

where the momentum space $\Gamma^{\vec{d}}$ is defined as

$$\Gamma^{\vec{d}} = \left\{ \vec{k} \in \mathbf{R}^3 \left| \vec{k} = \frac{2\pi}{L} \gamma^{-1} (\vec{m} + \frac{1}{2} \vec{d}) \text{ for } \vec{m} \in \mathbf{Z}^3 \right. \right\}. \quad (3.62)$$

By following the procedures in Sect. 3.2, we can expand the wave function $\phi_{L,CM}(\vec{r})$ in terms of spherical harmonics and spherical Bessel functions

$$\phi_{L,CM}(\vec{r}) = \sum_{l,m} \nu_{lm} \frac{(-1)^l}{4\pi} p^{l+1} \left\{ Y_{lm}(\theta, \varphi) n_l(pr) + \sum_{l',m'} \mathcal{M}_{lm,l'm'}^{\vec{d}}(p) Y_{l'm'}(\theta, \varphi) j_{l'}(pr) \right\} \quad (3.63)$$

where $\mathcal{M}_{lm,l'm'}^{\vec{d}}(p)$ is given by

$$\mathcal{M}_{lm,l'm'}^{\vec{d}}(p) = \frac{(-1)^l}{\pi^{3/2}} \sum_{j=|l-l'|}^{l+l'} \sum_{s=-j}^j \gamma^{-1} \frac{i^j}{q^{j+1}} C_{lm,js,l'm'} \mathcal{Z}_{js}^{\vec{d}}(1, q^2), \quad q = \frac{pL}{2\pi}. \quad (3.64)$$

The detailed expression for the modified zeta function $\mathcal{Z}_{lm}^{\vec{d}}(1, q^2)$ is given by

$$\begin{aligned} \mathcal{Z}_{lm}^{\vec{d}}(1, q^2) &= \gamma \int_0^1 dt e^{tq^2} \sum_{\vec{u} \in \mathbf{Z}^3, \vec{u} \neq 0} (-1)^{\vec{u} \cdot \vec{d}} i^l \mathcal{Y}_{lm}^* \left(-\frac{\pi \vec{\gamma} \vec{u}}{t} \right) \left(\frac{\pi}{t} \right)^{3/2} \exp \left(-\frac{(\pi \vec{\gamma} \vec{u})^2}{t} \right) \\ &+ \gamma \int_0^1 dt (e^{tq^2} - 1) \frac{1}{\sqrt{4\pi}} \delta_{l0} \delta_{m0} \left(\frac{\pi}{t} \right)^{3/2} - \gamma \pi \delta_{l0} \delta_{m0} \\ &+ \sum_{\frac{2\pi}{L} \vec{n} \in \Gamma^{\vec{d}}} \frac{\mathcal{Y}_{lm}^*(\vec{n})}{n^2 - q^2} \exp(-(n^2 - q^2)) \end{aligned} \quad (3.65)$$

Performing a comparison between $\phi_{L,CM}(\vec{r})$ and $\phi(\vec{r})$, which is the wave function in the infinite volume case and given by Eq. (3.11), we find

$$\phi(\vec{r})|_{r=R} = \phi_{L,CM}(\vec{r})|_{r=R} \Rightarrow b_{lm} \alpha_l(p) = \sum_{l',m'} b_{l'm'} \beta_{l'}(p) \mathcal{M}_{lm,l'm'}^{\vec{d}}(p). \quad (3.66)$$

Requiring the nontrivial solution of $\{b_{lm}\}$ in Eq. (3.66), we finally have

$$\det \left(AB^{-1} - M^{\vec{d}} \right) = 0, \quad (3.67)$$

with the matrix $M_{lm,l'm'}^{\vec{d}} = \mathcal{M}_{lm,l'm'}^{\vec{d}}(p)$. Thus, we establish the finite size formula for the MF with total momentum \vec{P} , which connects the discrete energy $E_{CM} = \sqrt{E^2 - \vec{P}^2}$ on the lattice with the scattering phase $\delta_l(p)$ in the finite volume.

In the case of $\vec{P} = \vec{0}$, with the properties

$$\begin{aligned} \vec{d} &= \vec{0}, \quad \gamma = 1, \\ \mathcal{Z}_{lm,l'm'}^{\vec{d}}(1; q^2) &= \mathcal{Z}_{lm,l'm'}(1; q^2), \\ \mathcal{M}_{lm,l'm'}^{\vec{d}}(p) &= \mathcal{M}_{lm,l'm'}(p), \end{aligned} \quad (3.68)$$

the Eq. (3.67) become the standard finite size formula established in the CMF.

3.5 Interpolating operators

In this section, we are going to discuss how to construct the interpolating operators for the pion-pion scattering system which project out the eigenstates associated with isospin number I and approximately angular momentum l .

The single pion states with 3-momentum \vec{p} form an isospin triplet $|I, I_3\rangle$ through

$$\begin{aligned} |1, +1\rangle &= |\pi^+\rangle = \pi^+(\vec{p}, t)|\Omega\rangle \\ |1, 0\rangle &= |\pi^0\rangle = \pi^0(\vec{p}, t)|\Omega\rangle \\ |1, -1\rangle &= |\pi^-\rangle = \pi^-(\vec{p}, t)|\Omega\rangle, \end{aligned} \quad (3.69)$$

with the interpolating operator $\pi^a(\vec{p}, t)$ defined as

$$\pi^a(\vec{p}, t) = \frac{1}{L^{3/2}} \sum_{\vec{x}} e^{-i\vec{p}\cdot\vec{x}} \left(\bar{\psi} \gamma_5 \frac{\tau^a}{2} \psi \right) (\vec{x}, t), \quad a = +, 0, - \quad (3.70)$$

For a two pion system, there are three possible isospin channels with $I = 0, 1, 2$

$$|\pi\pi\rangle = |\pi\rangle \otimes |\pi\rangle = |I=1\rangle \otimes |I=1\rangle = |I=2\rangle \oplus |I=1\rangle \oplus |I=0\rangle. \quad (3.71)$$

We construct the two-pion interpolating operators $\mathcal{O}_{\pi\pi}^{I, I_3}(\vec{p}_1, \vec{p}_2, t)$ to create the pion-pion scattering state with definite isospin number (I, I_3)

$$|\pi\pi; I, I_3\rangle = \mathcal{O}_{\pi\pi}^{I, I_3}(\vec{p}_1, \vec{p}_2, t)|\Omega\rangle. \quad (3.72)$$

and list the detailed expressions for operators $\mathcal{O}_{\pi\pi}^{I, I_3}(\vec{p}_1, \vec{p}_2, t)$ in Table. 3.1.

The next step to construct the operator with angular momentum l using $\mathcal{O}_{\pi\pi}^{I, I_3}(\vec{p}_1, \vec{p}_2, t)$ is however nontrivial, since the rotation symmetry denoted by the group $O(3)$ is broken by finite size effects and the angular momentum l is then not a good quantum number anymore. The symmetry conserved on the lattice is the so-called *hypercubic symmetry*. It is associated with the good quantum number Γ , which specifies the different irreducible representation (irrep) of the hyper-cubic group, G . Therefore, we construct the operator with definite quantum number Γ through

$$(\pi\pi)_\Gamma(t) = \frac{1}{N_G} \sum_{\hat{R} \in G} \chi_\Gamma(\hat{R}) \mathcal{O}_{\pi\pi}^{I, I_3}(\vec{P} + \hat{R}\vec{p}, -\hat{R}\vec{p}, t) \quad (3.73)$$

I_3	$I = 2$
+2	$\pi^+(\vec{p}_1, t)\pi^+(\vec{p}_2, t)$
+1	$\frac{1}{\sqrt{2}}(\pi^0(\vec{p}_1, t)\pi^+(\vec{p}_2, t) + \pi^+(\vec{p}_1, t)\pi^0(\vec{p}_2, t))$
0	$\frac{1}{\sqrt{6}}(2\pi^0(\vec{p}_1, t)\pi^0(\vec{p}_2, t) + \pi^-(\vec{p}_1, t)\pi^+(\vec{p}_2, t) + \pi^+(\vec{p}_1, t)\pi^-(\vec{p}_2, t))$
-1	$\frac{1}{\sqrt{2}}(\pi^0(\vec{p}_1, t)\pi^-(\vec{p}_2, t) + \pi^-(\vec{p}_1, t)\pi^0(\vec{p}_2, t))$
-2	$\pi^-(\vec{p}_1, t)\pi^-(\vec{p}_2, t)$
I_3	$I = 1$
+1	$\pi^+(\vec{p}_1, t)\pi^0(\vec{p}_2, t) - \pi^0(\vec{p}_1, t)\pi^+(\vec{p}_2, t)$
0	$\pi^+(\vec{p}_1, t)\pi^-(\vec{p}_2, t) - \pi^-(\vec{p}_1, t)\pi^+(\vec{p}_2, t)$
-1	$\pi^0(\vec{p}_1, t)\pi^-(\vec{p}_2, t) - \pi^-(\vec{p}_1, t)\pi^0(\vec{p}_2, t)$
I_3	$I = 0$
0	$\frac{1}{\sqrt{3}}(-\pi^0(\vec{p}_1, t)\pi^0(\vec{p}_2, t) + \pi^-(\vec{p}_1, t)\pi^+(\vec{p}_2, t) + \pi^+(\vec{p}_1, t)\pi^-(\vec{p}_2, t))$

Table 3.1: List of the pion-pion interpolating operators, $\mathcal{O}_{\pi\pi}^{I, I_3}$, classified by Isospin number I and I_3 .

where \vec{P} is the total momentum of the two-pion system and \hat{R} denotes the rotational operation acting momentum space. $\vec{P} + \hat{R}\vec{p}$ and $-\hat{R}\vec{p}$ are the momenta on the lattice and take the discrete values

$$\frac{L}{2\pi} (\vec{P} + \hat{R}\vec{p}) \in \mathbf{Z}^3, \quad \frac{L}{2\pi} (-\hat{R}\vec{p}) \in \mathbf{Z}^3. \quad (3.74)$$

The hyper-cubic group G is the sum of all rotational operations \hat{R} , which leave the total 4-momentum of the scattering system, (E, \vec{P}) , invariant

$$G = \left\{ \hat{R} \left| \sqrt{(\vec{P} + \hat{R}\vec{p})^2 + m_\pi^2} + \sqrt{(\hat{R}\vec{p})^2 + m_\pi^2} = E, \quad \hat{R}\vec{P} = \vec{P} \right. \right\}. \quad (3.75)$$

The normalization factor N_G denotes group element number of G . The constraints (3.74) and (3.75) together determine the rotational property of the group G . In the CMF, G is given by the cubic group O_h , while in the MF1 and MF2, G is given by the tetragonal group D_{4h} and the orthorhombic group D_{2h} , respectively.

The average over all the operations \hat{R} in the group G with the coefficient $\chi_\Gamma(\hat{R})$, which is the character of the irrep of Γ , projects out the scattering state with quantum number Γ on the lattice

$$|\pi\pi, \Gamma\rangle = (\pi\pi)_\Gamma(0)|\Omega\rangle. \quad (3.76)$$

The state $|\pi\pi, \Gamma\rangle$ can be formed by the linear combination of the scattering state in the infinite volume with exact quantum number l through

$$|\pi\pi, \Gamma\rangle = \sum_l C_{\Gamma,l} |\pi\pi, l\rangle, \quad C_{\Gamma,l} = \langle \pi\pi, l | \pi\pi, \Gamma \rangle, \quad (3.77)$$

where the coefficient $C_{\Gamma,l}$ determines how the scattering states in a finite box, $|\pi\pi, \Gamma\rangle$, couple to the states in the infinite volume, $|\pi\pi, l\rangle$, from which the l -th wave scattering phase $\delta_l(p)$ can be extracted. For example, in the CMF, the state $|\pi\pi, A_1^+\rangle$ consists of by

$$|\pi\pi, A_1^+\rangle = C_{\Gamma,0} |\pi\pi, l=0\rangle + C_{\Gamma,4} |\pi\pi, l=4\rangle + \dots \quad (3.78)$$

As we discussed in Sect. 3.3, we can treat the states with angular momenta $l \geq 4$ as perturbations and then have the approximation

$$|\pi\pi, A_1^+\rangle \approx C_{\Gamma,0} |\pi\pi, l=0\rangle. \quad (3.79)$$

It yields that the S-wave scattering phase can be determined by constructing the operator in the A_1^+ sector on the lattice.

In the $I = 2, I_3 = +2$ channel, our interest is to calculate the S-wave scattering length at vanishingly small relative momentum. Therefore, we construct the operator $(\pi\pi)_{A_1^+}(t)$ in the CMF using coefficients $\chi_{A_1^+}$, which is simply given by

$$(\pi\pi)_{A_1^+}(t) = \pi^+(\vec{0}, t) \pi^+(\vec{0}, t). \quad (3.80)$$

The corresponding finite size formula to calculate the scattering length is given by Eq. (3.45).

In the $I = 1, I_3 = 0$ channel, to obtain the maximal information on the scattering phase, we choose the irrep $\Gamma = T_1^-$ for the CMF, $\Gamma = A_2^-$ for the MF1 and $\Gamma = B_1^-$ for the MF2, so that in each frame, the energy eigenstate $|\pi\pi, \Gamma\rangle$ approximates to the P-wave state if one ignores the states with higher angular momentum.

The construction of the operator is performed using Eq. (3.73). Here we list the the expressions for the operators $(\pi\pi)(t)$ which will be used in our calculation of pion-pion scattering in the $I = 1$ channel. In the CMF, the operator is given by

$$(\pi\pi)_{T_1^-}(t) = \pi^+ \left(\frac{2\pi}{L} \vec{e}_3, t \right) \pi^- \left(-\frac{2\pi}{L} \vec{e}_3, t \right) - \pi^+ \left(-\frac{2\pi}{L} \vec{e}_3, t \right) \pi^- \left(\frac{2\pi}{L} \vec{e}_3, t \right). \quad (3.81)$$

In the MF1, it is

$$(\pi\pi)_{A_2^-}(t) = \pi^+ \left(\frac{2\pi}{L} \vec{e}_3, t \right) \pi^- (\vec{0}, t) - \pi^+ (\vec{0}, t) \pi^- \left(\frac{2\pi}{L} \vec{e}_3, t \right). \quad (3.82)$$

In the MF2, it is

$$(\pi\pi)_{B_1^-}(t) = \pi^+ \left(\frac{2\pi}{L} (\vec{e}_1 + \vec{e}_2), t \right) \pi^- (\vec{0}, t) - \pi^+ (\vec{0}, t) \pi^- \left(\frac{2\pi}{L} (\vec{e}_1 + \vec{e}_2), t \right). \quad (3.83)$$

From these interpolating operators, one can calculate the discrete energy spectrum from the corresponding Euclidean correlation functions. And, making use of the finite size formulae, it becomes finally possible to compute the P-wave scattering phase.

In the CMF, the finite size formula is given by Lüscher [25]

$$\tan^{-1} \delta_1(p) = (\gamma\pi^{3/2}q)^{-1} \mathcal{Z}_{00}^{\vec{d}}(1; q^2), \quad \text{for } \vec{d} = \vec{0} \text{ and } \Gamma = T_1^-, \quad (3.84)$$

in the MF1, it is provided by Rummukainen and Gottlieb [54]

$$\tan^{-1} \delta_1(p) = (\gamma\pi^{3/2}q)^{-1} (\mathcal{Z}_{00}^{\vec{d}} + \frac{2q^{-2}}{\sqrt{5}} \mathcal{Z}_{20}^{\vec{d}}), \quad \text{for } \vec{d} = \vec{e}_3 \text{ and } \Gamma = A_2^-, \quad (3.85)$$

while in the MF2, we have derived a similar relation by ourselves

$$\begin{aligned} \tan^{-1} \delta_1(p) = (\gamma\pi^{3/2}q)^{-1} (\mathcal{Z}_{00}^{\vec{d}} - \frac{q^{-2}}{\sqrt{5}} \mathcal{Z}_{20}^{\vec{d}} + i \frac{\sqrt{3}q^{-2}}{\sqrt{10}} (\mathcal{Z}_{22}^{\vec{d}} - \mathcal{Z}_{22}^{\vec{d}})) , \\ \text{for } \vec{d} = (\vec{e}_1 + \vec{e}_2) \text{ and } \Gamma = B_1^-. \end{aligned} \quad (3.86)$$

CHAPTER IV

I=2 CHANNEL: $\pi^+\pi^+$ SCATTERING LENGTH

4.1 *Physical background*

In the limit of massless up and down quarks a spontaneous breaking of chiral symmetry takes place in QCD,

$$SU(N_f)_R \times SU(N_f)_L \Rightarrow SU(N_f)_V, \quad N_f = 2. \quad (4.1)$$

Due to Goldstone's theorem [56] the meson spectrum contains three massless pseudo scalar Goldstone bosons, identified as the pion triplet: π^\pm and π^0 . Introducing an explicit mass term in the QCD Lagrangian lifts the masses of the pions, but they still remain much lighter than any other meson in QCD. Since the pions have an only small mass, their interactions are strongly determined by the underlying chiral symmetry and the scattering lengths are sensitive to the chiral dynamics of the strong interactions. For example, the S-wave pion-pion scattering lengths even vanish in the chiral limit when the quark masses are sent to zero. Non-perturbative calculations of the scattering lengths to probe the chiral dynamics, one of the subjects of this thesis, is an integral part of understanding the low energy properties of QCD.

As said above, in the real world, the masses of the quarks are not zero but small and induce an explicit but weak breaking of chiral symmetry. This breaking of chiral symmetry is systematically treated in χ PT [26,27] by considering the quark masses as perturbations. Furthermore, the pion-pion scattering lengths no longer vanish at non-zero quark masses and at leading order (LO) in χ PT are predicted by Weinberg [57] solely in terms of the pion mass, m_π , and the pion decay constant, f_π , as

$$m_\pi a_{\pi\pi}^{I=0} \approx \frac{7m_\pi^2}{16\pi f_\pi^2} = 0.160(1) \quad \text{and} \quad m_\pi a_{\pi\pi}^{I=2} \approx -\frac{m_\pi^2}{8\pi f_\pi^2} = -0.0456(1), \quad (4.2)$$

where $a_{\pi\pi}^{I=0}$ and $a_{\pi\pi}^{I=2}$ denote the isospin $I = 0$ and $I = 2$ S-wave scattering lengths, respectively. The next-to-leading order (NLO) corrections depend on unknown so-called low

energy constants (LECs), which can be determined from experimental measurements or lattice calculations.

The experimental measurement of $K^\pm \rightarrow \pi^+\pi^-e^\pm\nu$ (K_{e4}) decays by E865 at BNL [58] gives

$$m_\pi a_{\pi\pi}^{I=0} = 0.203 \text{ (33)} \quad \text{and} \quad m_\pi a_{\pi\pi}^{I=2} = -0.055 \text{ (23)}. \quad (4.3)$$

When combined with constraints from χ PT, these measurements yield

$$m_\pi a_{\pi\pi}^{I=0} = 0.216 \text{ (14)} \quad \text{and} \quad m_\pi a_{\pi\pi}^{I=2} = -0.0454 \text{ (34)}. \quad (4.4)$$

A combination of several experimental and theoretical inputs from Colangelo, Gasser and Leutwyler (CGL) [59, 60] produces a consistent but more precise result of

$$m_\pi a_{\pi\pi}^{I=0} = 0.220 \text{ (5)} \quad \text{and} \quad m_\pi a_{\pi\pi}^{I=2} = -0.0444 \text{ (10)}. \quad (4.5)$$

Additionally, the recent measurements of K_{e4} decays [61] and $K^\pm \rightarrow \pi^\pm\pi^0\pi^0$ decays [62] by NA48/2 at CERN [4] give, without making any use of χ PT constraints,

$$m_\pi a_{\pi\pi}^{I=0} = 0.221 \text{ (5)} \quad \text{and} \quad m_\pi a_{\pi\pi}^{I=2} = -0.0429 \text{ (47)}. \quad (4.6)$$

Including χ PT in their analysis, NA48/2 finds [63]

$$m_\pi a_{\pi\pi}^{I=0} = 0.220 \text{ (3)} \quad \text{and} \quad m_\pi a_{\pi\pi}^{I=2} = -0.0444 \text{ (9)}. \quad (4.7)$$

The results are all consistent with each other and the most precise results from NA48/2 are in agreement with the lattice results given shortly.

One obstacle to the non-perturbative determination of the pion-pion scattering length from Lattice QCD is the presence of disconnected diagrams that render the calculation of the $I = 0$ channel computationally demanding. On the other hand, the simpler $I = 2$ channel does not require such diagrams and consequently many lattice groups have focused their efforts on this case. Furthermore, most calculations of the scattering lengths to date have been carried out within the quenched approximation [64–85]. There have been only two previous calculations of $a_{\pi\pi}^{I=2}$ with dynamical fermions. The first such calculation was performed by CP-PACS with $N_f = 2$ tadpole-improved clover fermions at rather heavy

pion masses in the range $m_\pi = 0.5$ GeV to 1.1 GeV [3]. However, it is doubtful that χ PT at NLO, or any order, can be applied to such heavy pion masses. The other full QCD calculation was performed by NPLQCD with domain-wall valence quarks on the $N_f = 2+1$ asqtad-improved coarse MILC ensembles with $m_\pi = 290$ MeV to 590 MeV [1, 2]. Mixed-action χ PT at NLO was used to perform the chiral and continuum extrapolations. At the physical pion mass, NPLQCD finds

$$m_\pi a_{\pi\pi}^{I=2} = -0.04330(42) \quad \text{and} \quad l_{\pi\pi}^{I=2}(\mu = f_{\pi,\text{phy}}) = 6.2(1.2), \quad (4.8)$$

where $l_{\pi\pi}^{I=2}(\mu)$ is a LEC appearing in the χ PT description of the quark mass dependence of the scattering length. As discussed later, $l_{\pi\pi}^{I=2}(\mu)$ is evaluated at $\mu = f_{\pi,\text{phy}}$, where $f_{\pi,\text{phy}}$ is the physical value of the pion decay constant.

In this thesis we determine the S-wave $I = 2$ pion-pion scattering length and the corresponding $l_{\pi\pi}^{I=2}$. Compared to the previous calculations, we have more information in the low pion mass region (~ 300 MeV), which allows us to further probe the chiral properties of $a_{\pi\pi}^{I=2}$.

4.2 Method

4.2.1 Euclidean correlation function

As mentioned in Chapter 3, in the CMF, the finite size formula (3.45) establishes a relationship between the ground state energy shift $\delta E = E(L) - 2m$ in a finite box of size L and the corresponding S-wave scattering length a_0 . In the $I = 2$ pion-pion scattering channel, by inserting the variable changes

$$E(L) = E_{\pi\pi}^{I=2}, \quad m = m_\pi, \quad \delta E = \delta E_{\pi\pi}^{I=2}, \quad a_0 = a_{\pi\pi}^{I=2} \quad (4.9)$$

into Eq. (3.45), we can convert a lattice determination of the energy shift, $\delta E_{\pi\pi}^{I=2}$, into a calculation of $a_{\pi\pi}^{I=2}$.

To extract $\delta E_{\pi\pi}^{I=2}$, we construct the π^+ and $\pi^+\pi^+$ two-point correlation functions from the operators proposed in Ref. [74],

$$C_\pi(t) = \langle (\pi^+)^\dagger(t + t_s) \pi^+(t_s) \rangle \quad (4.10)$$

and

$$C_{\pi\pi}(t) = \langle (\pi^+\pi^+)^\dagger(t+t_s)(\pi^+\pi^+)(t_s) \rangle. \quad (4.11)$$

Here t_s is an arbitrary time slice, $\pi^+(t)$ is an interpolating operator given by Eq. (3.70) with zero 3-momentum and $(\pi^+\pi^+)(t)$ is an interpolating operator for the two pion state given by

$$(\pi^+\pi^+)(t) = \pi^+(t+a)\pi^+(t). \quad (4.12)$$

In order to avoid complications due to Fierz rearrangement of quark lines as discussed in Ref. [74], we use the π^+ interpolating fields at time slices separated by one lattice spacing. As we have discussed in Sect. 3.5, the operator $(\pi^+\pi^+)(t)$ projects out the scattering state $|\pi\pi, A_1^+\rangle$, which equals to the S-wave state in the infinite volume, ignoring the states with higher angular momentum.

As seen in Sect. 2.1, from the large time behavior of $C_\pi(t)$ and $C_{\pi\pi}(t)$, it is possible to extract the corresponding ground state energies as follows,

$$C_\pi(t) \rightarrow A_\pi \exp(-m_\pi t) \quad \text{and} \quad C_{\pi\pi}(t) \rightarrow A_{\pi\pi} \exp(-E_{\pi\pi}^{I=2} t), \quad (4.13)$$

where we assume that t is large enough to neglect excited states but still far enough from the boundaries to ignore boundary effects. Furthermore, constructing the following ratio of correlation functions we can determine $\delta E_{\pi\pi}^{I=2}$ directly as

$$\frac{C_{\pi\pi}(t)}{C_\pi^2(t)} \rightarrow \frac{A_{\pi\pi}}{A_\pi^2} \exp(-\delta E_{\pi\pi}^{I=2} t) \quad (4.14)$$

where t satisfies the same requirements as before. However, we use anti-periodic boundary conditions for the quarks in the time direction in order to match the sea quarks used in our calculation, and this leads to a more complicated time dependence for C_π and $C_{\pi\pi}$.

4.2.2 Anti-periodic boundary conditions

As mentioned above, in our calculation we employ anti-periodic boundary conditions in the time direction for the fermions. Using the transfer matrix formalism, the time dependence of our correlation functions is given by

$$\langle \mathcal{O}^\dagger(t)\mathcal{O}(0) \rangle = \text{Tr} \left(e^{-\hat{H}(T-t)} \mathcal{O}^\dagger(0) e^{-\hat{H}t} \mathcal{O}(0) \right) / Z, \quad Z = \text{Tr} \left(e^{-\hat{H}T} \right). \quad (4.15)$$

Here \hat{H} is the Hamiltonian operator, T is the total time extent of our lattice and $\mathcal{O}(t)$ represents either $\pi^+(t)$ or $(\pi^+\pi^+)(t)$. Inserting a complete set of eigenstates of \hat{H} into the above equation yields

$$\begin{aligned}\langle \mathcal{O}^\dagger(t)\mathcal{O}(0) \rangle &= \sum_{m,n} |\langle n|\mathcal{O}|m \rangle|^2 e^{-E_m(T-t)} e^{-E_n t} / Z \\ &= \sum_{m,n} |\langle n|\mathcal{O}|m \rangle|^2 e^{-(E_m+E_n)T/2} \cosh((E_m - E_n)(t - T/2)) / Z.\end{aligned}$$

The terms in the above series are thermally suppressed by factors of $e^{-E_m T}$ or $e^{-E_n T}$. Only those terms with $E_m = 0$ or $E_n = 0$ remain in the zero temperature, $T \rightarrow \infty$, limit. However, the effects of the suppressed contributions can still distort the behavior of correlation functions for finite values of T , particularly in the large t region.

This phenomenon does indeed occur here for the two pion operator. Intermediate states $\langle n| = \langle \pi^+|$ and $\langle m| = \langle \pi^-|$ give a constant, in t , contribution to $C_{\pi\pi}$,

$$|\langle \pi^+|\pi^+\pi^+|\pi^- \rangle|^2 e^{-m_\pi T} / Z. \quad (4.16)$$

This is comparable to the standard contribution,

$$|\langle \pi^+\pi^+|\pi^+\pi^+|\Omega \rangle|^2 e^{-E_{\pi\pi}^{I=2}T/2} \cosh(E_{\pi\pi}^{I=2}(t - T/2)) / Z, \quad (4.17)$$

when t approaches $T/2$. To be precise, for large enough volumes $E_{\pi\pi}^{I=2} = 2m_\pi + \delta E_{\pi\pi}^{I=2} \approx 2m_\pi$, and hence these two contributions to $C_{\pi\pi}$, $e^{-m_\pi T}$ and $e^{-E_{\pi\pi}^{I=2}T/2} \cosh(E_{\pi\pi}(t - T/2))$ are in fact nearly equal for $t = T/2$. Additionally, the factor $C_\pi(t)^2$ has similar problems. The correlator $C_\pi(t)$ itself has a simple spectral representation. However, the square is more complicated and also contains a constant, in t , contribution as well.

To eliminate these contaminations, we use the derivative method [86] and define a modified ratio, $R(t)$, in the following way

$$R(t + a/2) = \frac{C_{\pi\pi}(t) - C_{\pi\pi}(t + a)}{C_\pi^2(t) - C_\pi^2(t + a)}. \quad (4.18)$$

The asymptotic form for $R(t)$, ignoring terms suppressed relative to the leading contribution, is

$$R(t + a/2) = A_R \left(\cosh(\delta E_{\pi\pi}^{I=2} t') + \sinh(\delta E_{\pi\pi}^{I=2} t') \coth(2m_\pi t') \right) \quad (4.19)$$

β	$a\mu$	L/a	m_π	m_π/f_π	N	$a\delta E_{\pi\pi}^{I=2} \cdot 10^3$	$m_\pi a_{\pi\pi}^{I=2}$
3.90	0.0100	24	520	2.77(2)	479	7.23(59)(41)	-0.297(20)(16)
3.90	0.0085	24	480	2.61(1)	487	7.66(65)(33)	-0.269(17)(10)
3.90	0.0064	24	420	2.40(1)	553	9.6(1.3)(.6)	-0.252(22)(13)
3.90	0.0040	32	330	2.02(1)	490	3.96(36)(22)	-0.165(14)(08)
3.90	0.0030	32	290	1.85(1)	562	4.05(42)(21)	-0.130(12)(06)
4.05	0.0030	32	320	2.08(2)	375	7.1(1.2)(.9)	-0.171(18)(22)

Table 4.1: Ensembles used in the $I = 2$ pion-pion scattering. Only dimensionless quantities are needed in this calculation, but for guidance we give the value of m_π rounded to the nearest MeV for each ensemble indicated by β , $a\mu$ and L/a . We also list the ratio m_π/f_π , the number, N , of configurations used, the energy shift $a\delta E_{\pi\pi}^{I=2}$ and the scattering length $m_\pi a_{\pi\pi}^{I=2}$. The first uncertainty is statistical and, when present, the second one is systematic.

where A_R is a combination of amplitudes in C_π and $C_{\pi\pi}$ and $t' = t + a/2 - T/2$. Since m_π is the most accurately calculated component of our calculation, $R(t)$ provides a nearly direct determination of $\delta E_{\pi\pi}^{I=2}$ and cleanly eliminates the unwanted thermal contributions that spoil the simple ratio given earlier.

4.3 Lattice calculation

4.3.1 Ensemble information

Most of the results presented here are from a sequence of ensembles with a lattice spacing of $a = 0.079$ fm and a box size of $L = 1.9$ fm. The pion masses range from $m_\pi = 290$ MeV to 520 MeV. For the lower pion masses the volume is increased to $L = 2.5$ fm, and there is one calculation using a finer lattice spacing of $a = 0.063$ fm. The parameters relevant to this calculation are given in Table 4.1, and further details can be found in Refs. [29–32].

4.3.2 Stochastic sources

For the calculation of pion correlation functions, it is known that the stochastic source method is more efficient than the point source method. Therefore, in the present work, we employ Z_4 stochastic noise with two noise sources generated on each source time slice. Since we place the source on two time slices for the $\pi^+\pi^+$ correlation function, t_s and $t_s + a$, we therefore perform four inversions for each configuration. We remark that we also use the one-end trick in this work for the evaluation of correlation functions [87–89] leading to

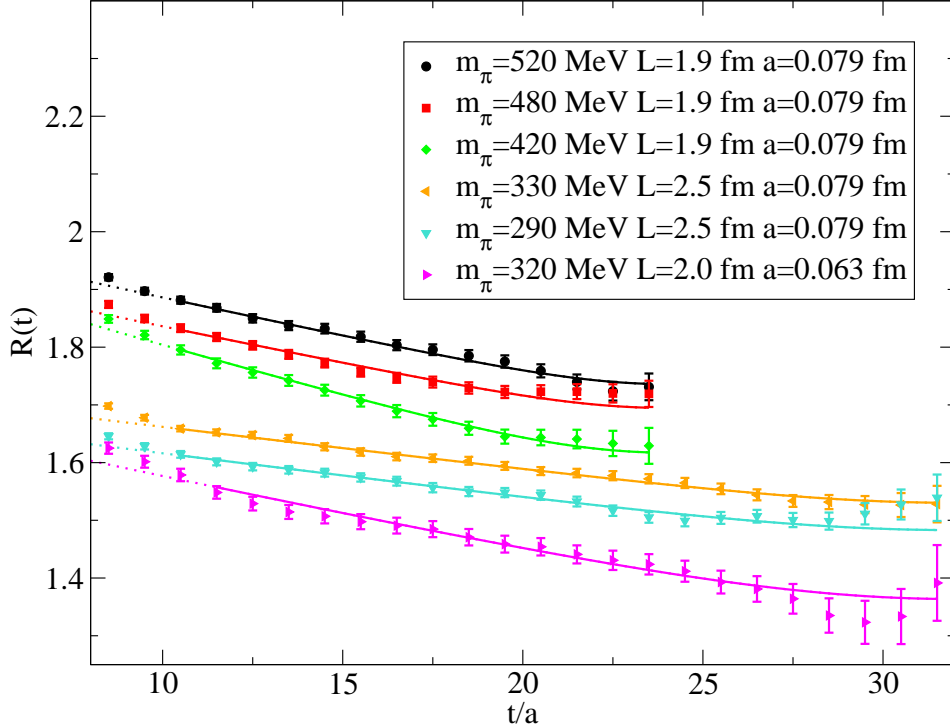


Figure 4.1: The ratio $R(t)$ as a function of t . The solid lines are correlated fits to Eq. (4.19), from which the energy shifts $a\delta E_{\pi\pi}^{I=2}$ are extracted. The ensembles have been shifted vertically to facilitate easier comparison.

a further improvement in the signal-to-noise ratio. Additionally, the source time slices, t_s , are chosen randomly to reduce the autocorrelation between consecutive trajectories.

4.4 Results

4.4.1 Calculation of $m_\pi a_{\pi\pi}^{I=2}$

In Fig. 4.1 we show our lattice results for $R(t)$, defined in Eq. (4.18), as a function of the time t together with a correlated fit¹ to the asymptotic form given in Eq. (4.19). All the ensembles shown in Fig. 4.1 visibly agree with the corresponding fit and lead to reasonable values of χ^2 per degree of freedom (dof), where χ^2 is the *correlated figure-of-merit function*. To further verify these fits, we examined several possible sources of systematic error. First, the ratio could suffer from bias at large t , so we examined the jackknife estimate of bias

¹The lattice results for $R(t)$ at time slice $t = t_1$ and $t = t_2$ are correlated. The correlated fit takes full consideration of such effects into account.

but found it to be significantly smaller than the errors for all the ensembles. Second, we considered the possibility that we underestimated the errors due to autocorrelations. However, both the gamma method [90] and standard binning showed no significant signs of autocorrelation for $R(t)$ in any of the ensembles. The possibility of π^0 mixing, due to the breaking of parity at non-zero lattice spacing for twisted mass fermions, is considered in Sect. 4.4.2. But as described there in more detail, we find no statistically significant indications of the π^0 contributions.

There is one further possible systematic error due to the contributions from excited states in the small t region or from unphysical π^0 states in the large t region. To ensure that the fits for these ensembles are safe from such effects, we study the systematic errors caused by choosing a fitting window in which to match to the asymptotic form for $R(t)$. First we ensure that the results exhibit clear plateaus when we increase the minimum t or decrease the maximum t used in the fits. However, to provide a quantitative estimate of the systematic error, we perform the following distribution method. We collect the results for $a\delta E_{\pi\pi}^{I=2}$ from all fitting intervals with $\chi^2/\text{dof} < 2$. This includes varying both the minimum and maximum time extent for the fitting range and results in 30 to 60 values of $a\delta E_{\pi\pi}^{I=2}$ for each ensemble. We then make the distribution of these selected results and choose the median of this distribution for the central value. Then we take the central, and symmetric about the median, 68% region of the distribution to define the systematic error. Finally, we use the jackknife method to determine the statistical error on the central values. This method is also applied to $m_\pi a_{\pi\pi}^{I=2}$, and the results for $a\delta E_{\pi\pi}^{I=2}$ and $m_\pi a_{\pi\pi}^{I=2}$ are given in Table 4.1. As shown in this table, the resulting estimates of the systematic errors are typically smaller than the corresponding statistical errors, and are at worst of the same order as the statistical errors. Since the distribution method used to estimate the systematic errors is itself subject to statistical errors, this is precisely what is expected if there are no substantial systematic effects. However, since the final statistical precision for the value of $m_\pi a_{\pi\pi}^{I=2}$ at the physical limit turns out to be quite small, we decided, in order to avoid underestimating our final error, to carefully propagate these systematic errors through to the final result as described later in Sect. 4.4.5.

4.4.2 π^0 contamination

Twisted mass fermions violate parity and isospin at non-zero values of the lattice spacing. Therefore the spectral representation of the π^+ and $\pi^+\pi^+$ correlators can admit states that would not be present in the continuum limit. In particular, unphysical contributions from the π^0 , which has a mass m_{π^0} different, and smaller, than the mass m_π of the π^\pm , may enter the C_π and $C_{\pi\pi}$ correlators in several ways [89]. Furthermore, these effects are believed to be more noticeable in pion-pion scattering, so the successful calculation of all three isospin channels, $I = 0, 1$ and 2 , would test the twisted mass formulation of lattice QCD.

The π^0 can enter the C_π correlator through intermediate states of the form $\langle \pi^+ | \pi^+ | \pi^0 \rangle$ and $\langle \pi^+ \pi^0 | \pi^+ | \Omega \rangle$. The former contribution is thermally suppressed by a factor of $e^{-m_{\pi^0} T}$, however it leads to a time dependence with an energy of $m_\pi - m_{\pi^0}$ that is lighter than the usually expected m_π ground state. The second contribution is not thermally suppressed but corresponds to the first excited state with energy $E_{\pi^+\pi^0} \approx m_\pi + m_{\pi^0}$. This is lighter than the first physical excited state with energy near $3m_\pi$. Similarly, $C_{\pi\pi}$ contains unphysical contributions from $\langle \pi^+\pi^+ | \pi^+\pi^+ | \pi^0 \rangle$ and $\langle \pi^+\pi^+\pi^0 | \pi^+\pi^+ | \Omega \rangle$. Again there is an additional light state that is thermally suppressed by $e^{-m_{\pi^0} T}$ but has an energy of $E_{\pi^+\pi^+} - m_{\pi^0} \approx 2m_\pi - m_{\pi^0}$ that is lower than the physical ground state near $2m_\pi$, and the first excited state is lowered to $E_{\pi^+\pi^+\pi^0} \approx 2m_\pi + m_{\pi^0}$ rather than the expected energy of approximately $2\sqrt{m_\pi^2 + (2\pi/L)^2}$.

The parity violating matrix elements responsible for these effects are $O(a)$ in the lattice spacing, even at maximal twist, however the matrix elements appear squared in the correlators. Therefore these unphysical states make an $O(a^2)$ contribution. The question, however, is not about the scaling in the lattice spacing, but about the size of this contribution at the lattice spacings used in this work. A detailed discussion of this issue can be found in Ref. [91]. Here, our focus is more practical. We want to ensure that the scattering lengths calculated in this work are not significantly distorted due to these effects.

First, the naive estimate for the suppression factor for the additional light contributions, $m_\pi - m_{\pi^0}$ in C_π and $E_{\pi^+\pi^+} - m_{\pi^0}$ in $C_{\pi\pi}$, is $(a\Lambda_{\text{QCD}})^2 e^{-m_{\pi^0} T}$. The value of m_{π^0} is difficult to calculate precisely, but it is clear from Ref. [91] that m_{π^0} is never more than 20% lighter

than m_π for the ensembles in this work. Therefore we will simply use m_π and a value of $\Lambda_{\text{QCD}} = 250$ MeV to set the order of magnitude for these suppression factors. We find that for the ensembles used here, the largest value of $(a\Lambda_{\text{QCD}})^2 e^{-m_{\pi^0} T}$ is $9 \cdot 10^{-6}$ for the $\beta = 4.05$, $a\mu = 0.0030$ ensemble in Table 4.1. Using the actual value of m_{π^0} from [91] raises this to $2 \cdot 10^{-5}$. This value is small, but it is not too far beyond the statistical precision of the correlators used to calculate $a\delta E_{\pi\pi}^{I=2}$, hence we must carefully check for these contributions.

Second, there are the additional states that are only suppressed by $(a\Lambda_{\text{QCD}})^2$. However, these states are heavier than the physical state and hence would occur in the correlators as excited states. The naive suppression factors are $1 \cdot 10^{-2}$ and $7 \cdot 10^{-3}$ for $a = 0.079$ fm and 0.063 fm respectively. These simple estimates are larger than for the other states, however these contributions are also more strongly suppressed by their own energies.

In the light of these arguments, we made a significant effort to attempt to find such effects anyway. We tried fitting the individual $C_\pi(t)$ and $C_{\pi\pi}(t)$ correlators as well as the ratio $R(t)$ to various functional forms including the physical state and both the additional heavier and lighter states, just the lighter state or just the heavier state. We fit the most general forms, keeping all energies as free parameters, and additionally constrained forms, in which we constrained m_{π^0} based on known values. And we also explored several minimization methods. The net result was that one could indeed lower the χ^2 value for each fit, but the χ^2 per degree of freedom still increased, indicating no statistically significant contribution from the unwanted π^0 states.

However, we must offer a few words of caution. While we could not find any compelling evidence for these contributions, we of course can not rule out their presence at a level beneath our statistical resolution. We should further note that there are visible excited states in the correlators. However, the accuracy of the correlators for the ensembles studied here does not allow us to distinguish the physical excited states, near $3m_\pi$ for C_π and $2\sqrt{m_\pi^2 + (2\pi/L)^2}$ for $C_{\pi\pi}$, from the unphysical excited states, near $m_\pi + m_{\pi^0} \approx 2m_\pi$ for C_π and $2m_\pi + m_{\pi^0} \approx 3m_\pi$ for $C_{\pi\pi}$. The extensive study of systematic errors due to the fitting range discussed in the previous section was partially motivated by these issues. It provides the quantitative statement that these effects do not rise to the level of our statistical

precision and gives an estimate of the systematic error.

Additionally, there are two reasons that these contributions may be smaller than anticipated. First, the unphysical contributions correspond to scattering states that may be suppressed by a power of the volume. Second, the construction of $R(t)$ in Eq. (4.18) forms a discrete approximation to the ratio of derivatives of $C_{\pi\pi}$ and C_{π}^2 and may further suppress the nearly constant light state contributions.

4.4.3 Finite volume effects

The dominant finite size effect in this calculation is, of course, the shift in $\delta E_{\pi\pi}^{I=2}$ due to the interactions of two pions in a finite volume. Additionally, there are the exponentially small, as opposed to the merely power suppressed, finite volume corrections to $I = 2$ pion-pion scattering that have been determined for scattering near threshold in Ref. [92]. The resulting finite size corrections for the scattering length are given there as,

$$(m_{\pi}a_{\pi\pi}^{I=2})_L = (m_{\pi}a_{\pi\pi}^{I=2})_{\infty} + \Delta_{FV} \quad (4.20)$$

where

$$\begin{aligned} \Delta_{FV} &= -\frac{m_{\pi}^2}{8\pi f_{\pi}^2} \left\{ \frac{m_{\pi}^2}{f_{\pi}^2} \frac{\partial}{\partial m_{\pi}^2} i\Delta\mathcal{I}(m_{\pi}) + \frac{2m_{\pi}^2}{f_{\pi}^2} i\Delta\mathcal{J}_{exp}(4m_{\pi}^2) \right\} \\ &= \frac{1}{2^{13/2}\pi^{5/2}} \left(\frac{m_{\pi}}{f_{\pi}} \right)^4 \sum_{|\mathbf{n}| \neq 0} \frac{e^{-|\mathbf{n}|m_{\pi}L}}{\sqrt{|\mathbf{n}|m_{\pi}L}} \left\{ 1 - \frac{17}{8} \frac{1}{|\mathbf{n}|m_{\pi}L} + O(L^{-2}) \right\}. \end{aligned}$$

Using the above result, we calculate the corrections to $m_{\pi}a_{\pi\pi}^{I=2}$. Compared to the statistical errors, the finite volume corrections are negligible. To be precise, they are never more than 6% of the corresponding statistical error and are hence ignored in the following analysis.

There is a second finite size effect originating from Eq. (3.15), which is used to relate the scattering phase $\delta(p)$ at vanishingly small momentum p to the scattering length. As argued in Sect. 3.3, the dependence on the effective range r_{eff} is very small and gives rise to the corrections at $O(L^{-6})$ in Eq. (3.45). Assuming that the effective range is at most twice the scattering length, this correction can be estimated using the measured values of m_{π} and $\delta E_{\pi\pi}^{I=2}$. We find that this correction is never more than 9% of the corresponding statistical error of $m_{\pi}a_{\pi\pi}^{I=2}$. Hence, this finite size effect is also sufficiently small to be ignored as well.

4.4.4 Lattice artifacts

Most of the calculations presented here use a single lattice spacing of 0.079 fm, but we have also performed an additional calculation of $\delta E_{\pi\pi}^{I=2}$ and $m_\pi a_{\pi\pi}^{I=2}$ at a second lattice spacing of 0.063 fm and at a pion mass of 320 MeV. This pion mass lies very close to that of the one obtained at $a = 0.079$ fm and $m_\pi = 330$ MeV. The physical volumes of these two ensembles differ, so the values of $\delta E_{\pi\pi}^{I=2}$ cannot be directly compared. However, assuming that FSM correctly accounts for the finite volume dependence of $\delta E_{\pi\pi}^{I=2}$ for these two ensembles, we can compare $m_\pi a_{\pi\pi}^{I=2}$ for the two lattice spacings, and indeed we do find statistical agreement between the two ensembles as indicated in Table 4.1. Furthermore, as described in the next section, we note that the expected $O(a^2)$ corrections from maximally twisted mass Lattice QCD are actually weakened to $O(m_\pi^2 a^2)$ for the $I = 2$, $I_3 = \pm 2$ channel as shown using twisted mass χ PT [93], thus suggesting further that the lattice spacing dependence of $m_\pi a_{\pi\pi}^{I=2}$ is mild for the calculations in this work.

4.4.5 Chiral extrapolation

The pion-pion scattering lengths have recently been calculated in twisted mass χ PT [93]. This is an expansion of twisted mass lattice QCD in both the quark masses and the lattice spacing. There it is shown that at NLO the lattice spacing corrections to the $I = 2$, $I_3 = \pm 2$ scattering lengths are proportional to $\cos(\omega)$, where ω is the twist angle. Thus at maximal twist, $\omega = \pi/2$, the explicit discretization errors vanish exactly, and the scattering length can be simply represented by the continuum NLO χ PT formula [26, 94].

As suggested in Refs. [1, 2], we perform the chiral extrapolation of $m_\pi a_{\pi\pi}^{I=2}$ in terms of m_π/f_π instead of m_π . Additionally, the χ PT renormalization scale is fixed as $\mu = f_{\pi,\text{phy}}$. The resulting NLO expression is then

$$m_\pi a_{\pi\pi}^{I=2} = -\frac{m_\pi^2}{8\pi f_\pi^2} \left\{ 1 + \frac{m_\pi^2}{16\pi^2 f_\pi^2} \left[3 \ln \frac{m_\pi^2}{f_\pi^2} - 1 - l_{\pi\pi}^{I=2}(\mu = f_{\pi,\text{phy}}) \right] \right\}, \quad (4.21)$$

where $l_{\pi\pi}^{I=2}(\mu)$ is related to the Gasser-Leutwyler coefficients \bar{l}_i as [95]

$$l_{\pi\pi}^{I=2}(\mu) = \frac{8}{3}\bar{l}_1 + \frac{16}{3}\bar{l}_2 - \bar{l}_3 - 4\bar{l}_4 + 3 \ln \frac{m_{\pi,\text{phy}}^2}{\mu^2}. \quad (4.22)$$

It is important to note that extrapolating in m_π/f_π instead of simply m_π does indeed change the expression for $m_\pi a_{\pi\pi}^{I=2}$ but only at the next-to-next-to-leading order (NNLO). The advantage of this form is that m_π/f_π is calculated directly on the lattice with small errors and the chiral extrapolation does not require fixing a physical value for the lattice spacing.

We now fit our lattice results for $m_\pi a_{\pi\pi}^{I=2}$ from Table 4.1 to the functional form in Eq. (4.21) in order to extrapolate $m_\pi a_{\pi\pi}^{I=2}$ to the physical point and also extract the low energy constant $l_{\pi\pi}^{I=2}(\mu = f_{\pi,\text{phy}})$. The calculated values for the scattering length and the resulting χ PT fit curve are shown in Fig. 4.2. In the same figure, we also provide

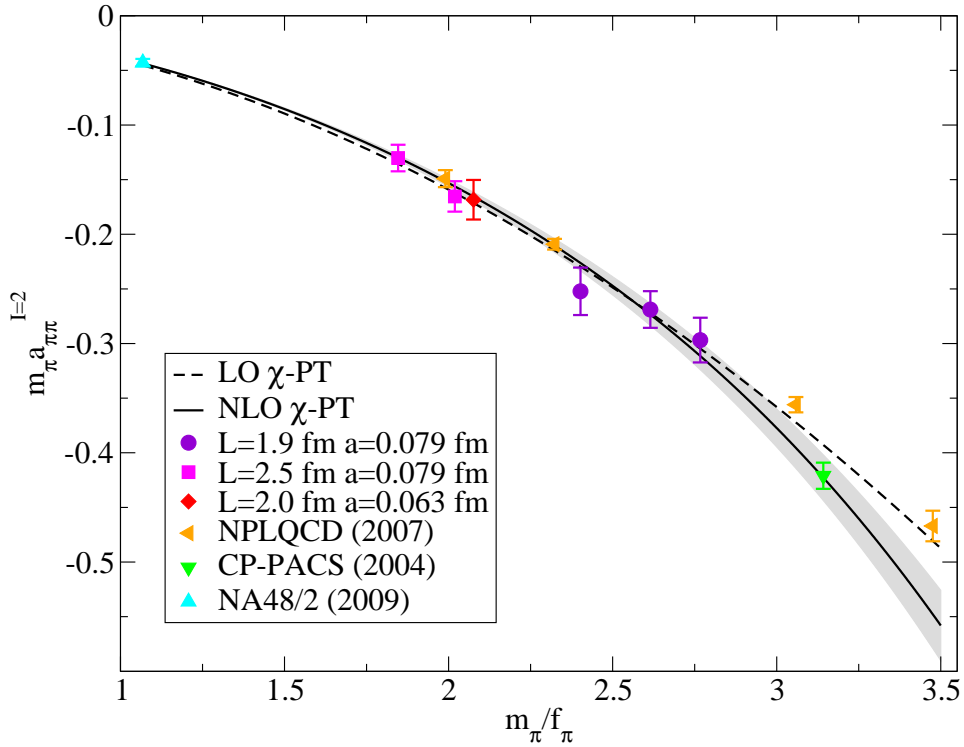


Figure 4.2: Chiral extrapolation for the $I=2$ pion-pion scattering length. The results in this work are shown together with the lattice calculations of NPLQCD [1, 2] and CP-PACS [3] and the direct measurement from NA48/2 at CERN [4].

a comparison to the lattice results of NPLQCD [1, 2] and CP-PACS [3] and the direct measurement from NA48/2 at CERN [4]. We find general agreement between our calculation and the results of NPLQCD at similar pion masses. In particular, the agreement between our results and NPLQCD suggests that the effect of the missing strange quark in our current

calculation is small.

To highlight the impact of the NLO terms in the χ PT description of the pion mass dependence of $m_\pi a_{\pi\pi}^{I=2}$ and to understand the role of yet higher order terms, we show the difference between the lattice calculations of the scattering length and the LO χ PT prediction in Fig. 4.3. We find that the scattering lengths statistically agree with the LO

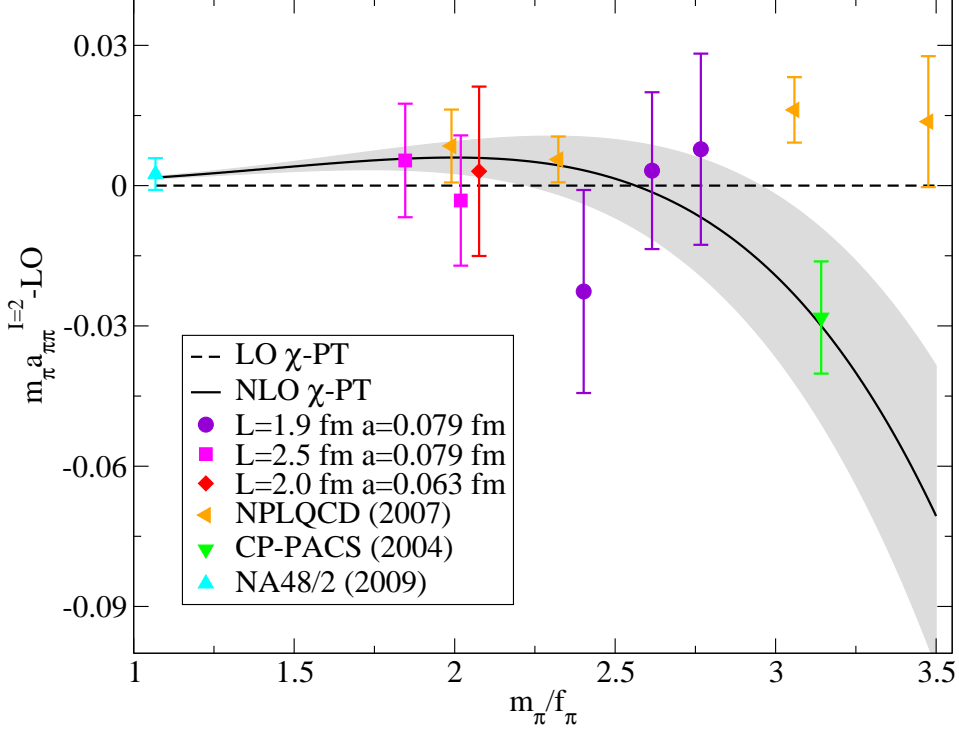


Figure 4.3: Difference between the lattice calculation of the scattering lengths and the LO χ PT prediction. The scattering lengths agree statistically with the LO χ PT prediction for $m_\pi = 290$ MeV to 520 MeV.

χ PT result for all lattice calculations with $m_\pi < 520$ MeV. Accordingly, the NLO χ PT functional form provides a reasonable description of the lattice results in the same region of m_π . As a further check, we fit our calculations to the NNLO form for $m_\pi a_{\pi\pi}^{I=2}$ [60, 95] and found $m_\pi a_{\pi\pi}^{I=2} = -0.041(12)$ at the physical point. The statistical error is large, as one would expect given that our results already agree statistically with the LO χ PT form, but the resulting NNLO extrapolation of $m_\pi a_{\pi\pi}^{I=2}$ does agree with the NLO fit. Given the size of the statistical errors, we are unable to make any meaningful estimate of the NNLO LECs, however, the effects from truncating the χ PT series to NLO is included in our estimate of

systematic errors.

The systematic error on the extrapolated value of $m_\pi a_{\pi\pi}^{I=2}$ and $l_{\pi\pi}^{I=2}$ has several components. First, the systematic errors of the $m_\pi a_{\pi\pi}^{I=2}$ that we obtain for each ensemble are propagated through the chiral extrapolation. This is accomplished by again collecting all fit ranges for each ensemble with $\chi^2/\text{dof} < 2$ as earlier. This gives approximately 10^{10} χ PT fits from which we randomly choose 2000 to sample the distribution of the extrapolated values of $m_\pi a_{\pi\pi}^{I=2}$. As for the individual $m_\pi a_{\pi\pi}^{I=2}$, we use the distribution method to determine an estimate of the systematic error due to the fit ranges from each ensemble. The second systematic uncertainty arises from the chiral fit itself. This is estimated by taking the difference in the extrapolated values from the NLO χ PT fit to all six and just the lightest five ensembles. Finally, the extrapolation to the physical point requires the experimental value for m_π/f_π . The experimental error on this quantity introduces an error that is nearly 50% of the corresponding statistical error and hence is also included. All three effects are added in quadrature to form the total estimated systematic error. Using the latest PDG [20] values of $m_{\pi^+} = 139.5702(4)$ MeV and $f_{\pi^+} = 130.4(2)$ MeV to determine the physical limit, we obtain the final result

$$m_\pi a_{\pi\pi}^{I=2} = -0.04385(28)(38) \quad \text{and} \quad l_{\pi\pi}^{I=2}(\mu = f_{\pi,\text{phy}}) = 4.65(0.85)(1.07). \quad (4.23)$$

This agrees with the previously mentioned results: the lattice calculation from NPLQCD [1, 2], the so-called CGL analysis [59,60] and the E865 [58] and NA48/2 [4] measurements and represents agreement among the experimental and theoretical determinations of $m_\pi a_{\pi\pi}^{I=2}$ at the 1% level.

CHAPTER V

I=1 CHANNEL: ρ RESONANCE PARAMETERS

5.1 *Physical background*

The calculation of the hadron spectrum from first principles is of particular interest not only because it would provide a test of the underlying theory, QCD, but also because it would lead to a deeper understanding of the physics of the strong interaction. An important observation is that many of these hadrons exist only as resonances. Although studied theoretically for many years, the determination of the corresponding resonance parameters is afflicted with many difficulties since the computation of resonance masses and decay widths is essentially a non-perturbative problem. The only known way to extract the resonance parameters non-perturbatively from first principles is the use of Lattice QCD.

On a fundamental level, the appearance of a resonance is primarily a dynamical phenomenon, which is reflected in the observed scattering processes. Hence, to extract the resonance parameters, one needs to study particle scattering. Experimentally, one can get the information on the nature of the considered resonance from the experimental measurement of the scattering cross section or equivalently the scattering phase. Theoretically, the procedure used in Lattice QCD is similar. Using the FSMs proposed in Refs. [21–25, 54], the scattering phase can be computed numerically and then used to determine the values of the resonance mass and the decay width.

The experimental measurements of the decay width for some resonances have reached a precision of a few MeVs¹, while the masses are typically several hundred MeVs. However, the lattice study of the decay width is still far away from such accuracy. Therefore, at the current stage, our study is more of a conceptual and basic nature to understand how resonances can be treated and understood within lattice field theory. We believe that in

¹For example, the latest PDG [20] value of the ρ -meson decay width is $\Gamma_\rho = 149.1(8)$ MeV

the future, with the increase of computing power and the acceleration of algorithms, the Lattice QCD technique can provide a competitive result to experiment.

As we have discussed in Chapter 1, the case of the ρ -meson decaying into two pions in the P-wave serves as an ideal laboratory for lattice studies of resonances and is of fundamental importance in understanding the underlying dynamics of hadronic interactions. Moreover, the results for the ρ -resonance mass and decay width can directly be used in applications such as the calculation of the vacuum polarization tensor that is part of the QCD corrections to $g_\mu - 2$ [96,97] and the comparison of the electromagnetic form factor of the pion with the vector exchange model [98]. Pioneering attempts were made to study ρ -meson decay in quenched QCD [99,100] where no actual decay takes place. The first full QCD calculation [101] evaluated the decay width from the $\rho \rightarrow \pi\pi$ transition amplitude $\langle \rho | \pi\pi \rangle$, which, however, was carried out with large quark masses that do not allow for a physical decay since the requirement for ρ decay, $m_\pi/m_\rho < 0.5$, had not been fulfilled. So far, only a few lattice calculations [102–104] had quark masses light enough to address the ρ -meson decay directly. All these studies concentrated on only one or two scattering phases for each ensemble thus generating too few data points to map out the resonance region.

In this thesis we calculate the P-wave pion-pion scattering phase in the isospin $I = 1$ channel fulfilling the physical kinematics of $m_\pi/m_\rho < 0.5$. As discussed in Chapter 3, we perform the calculation in the CMF, the MF1 and the MF2, respectively. In each frame, we evaluate the scattering phase from the energy eigenvalues of the ground state and the first excited state. Using three frames allows us to obtain six points for the scattering phase for each ensemble.

We think that therefore our calculations have several advantages compared to the earlier works. First, using the FSMs in different frames provides a check of the accuracy of the FSMs themselves. Second, extracting the resonance parameters from six data points allows us to obtain more accurate results. Third, some of the scattering phases are measured at energies which lie directly in the resonance region $[m_\rho - \Gamma_\rho/2, m_\rho + \Gamma_\rho/2]$, allowing us to directly map out the resonance region. Additionally, we compute the ρ resonance parameters at several values of the quark mass thus obtaining the quark mass dependence

of the resonance mass and decay width.

5.2 Method

5.2.1 Correlation matrix

In determining the resonance parameters, we will concentrate on the $I = 1, I_3 = 0$ channel. The reason is simply that in this channel, by neglecting the isospin symmetry breaking effects, we do not have to consider the computationally demanding disconnected diagrams that would appear in the $I = 1, I_3 = \pm 1$ channel. In the $I = 1, I_3 = 0$ channel, the ρ^0 meson decays into a π^+ and π^- in the P-wave. In each of the frames we will be using, the energy eigenstate $|\pi\pi, \Gamma\rangle$ approximates the P-wave state if one ignores the states with higher angular momentum. This is feasible if we construct the states $|\pi\pi, \Gamma\rangle$ using the irreducible representation $\Gamma = T_1^-$ for the CMF, $\Gamma = A_2^-$ for the MF1 and $\Gamma = B_1^-$ for the MF2, respectively.

The finite size formulae, which relate the center-of-mass energy E_{CM} on the lattice to the P-wave scattering phase $\delta_1(p)$ in the infinite volume, are given by Eq. (3.84–3.86) in Sect. 3.5. In the CMF, the value of E_{CM} is directly given by the discrete energy eigenvalue E extracted from the large time behavior of the corresponding correlation function. In the MF, E_{CM} is related to E through the Lorentz transformation

$$E_{CM}^2 = E^2 - \vec{P}^2, \quad (5.1)$$

where \vec{P} is the total momentum of the MF.

In order to calculate the energy eigenvalue E , we construct a 2×2 correlation matrix through

$$C_{2 \times 2}(t) = \begin{pmatrix} \langle (\pi\pi)(t) (\pi\pi)^\dagger(0) \rangle & \langle (\pi\pi)(t) \rho^\dagger(0) \rangle \\ \langle \rho(t) (\pi\pi)^\dagger(0) \rangle & \langle \rho(t) \rho^\dagger(0) \rangle \end{pmatrix}, \quad (5.2)$$

where the $\pi\pi$ two-point correlation function is constructed from the interpolating operators detailed in Sect. 3.5. In the CMF, the interpolating operator for two pions is given by

$$(\pi\pi)(t) = \pi^+ \left(\frac{2\pi}{L} \vec{e}_3, t \right) \pi^- \left(-\frac{2\pi}{L} \vec{e}_3, t \right) - \pi^+ \left(-\frac{2\pi}{L} \vec{e}_3, t \right) \pi^- \left(\frac{2\pi}{L} \vec{e}_3, t \right). \quad (5.3)$$

This operator belongs to the T_1^- representation of the cubic group O_h on the lattice. In the two MFs, the $\pi\pi$ operator can be given in a unified form through

$$\pi\pi(t) = \pi^+ \left(\vec{P}, t \right) \pi^- \left(\vec{0}, t \right) - \pi^+ \left(\vec{0}, t \right) \pi^- \left(\vec{P}, t \right), \quad (5.4)$$

where \vec{P} is the total momentum of the MF system. In the MF1, $\vec{P} = (2\pi/L)\vec{e}_3$ and the operator belongs to the A_2^- representation of the tetragonal group D_{4h} . In the MF2, $\vec{P} = (2\pi/L)(\vec{e}_1 + \vec{e}_2)$ and the operator belongs to the B_1^- representation of the orthorhombic group D_{2h} . All these operators belong to the isospin representation $(I, I_3) = (1, 0)$ as desired.

The interpolating operator for the neutral ρ -meson is constructed through a local vector current,

$$\rho(t) = \rho^0(\vec{P}, t) = \frac{1}{L^{3/2}} \sum_{\vec{x}} e^{-i\vec{P}\cdot\vec{x}} \left(\bar{\psi}(\vec{a}\cdot\vec{\gamma}) \frac{\tau^0}{2} \psi \right) (\vec{x}, t), \quad \vec{a}\cdot\vec{\gamma} = \sum_i a_i \gamma_i, \quad (5.5)$$

where \vec{a} indicates the polarization of the vector current. To guarantee total momentum conservation, the summation is taken over spatial position \vec{x} with a factor $e^{i\vec{P}\cdot\vec{x}}$, which constrains the considered states to those with momentum \vec{P} .

With the available operators $(\pi\pi)(t)$ and $\rho(t)$, one can construct the off-diagonal correlator $\langle (\pi\pi)(t) \rho^\dagger(0) \rangle$. Ignoring boundary condition effects for a moment, this off-diagonal correlation function can be written as

$$\langle \Omega | (\pi\pi)(t) \rho^\dagger(0) | \Omega \rangle = \langle \Omega | (\pi\pi)(0) e^{-\hat{H}t} \rho^\dagger(0) | \Omega \rangle = \sum_n a_n \langle \pi\pi, E_n | \rho^\dagger(0) | \Omega \rangle e^{-E_n t}. \quad (5.6)$$

Here the energy eigenstates of the Hamilton operator \hat{H} , $|\pi\pi, E_n\rangle$, are created by acting with the operator $(\pi\pi)^\dagger(0)$ on the vacuum $|\Omega\rangle$. a_n is a coefficient which depends on the way the operator $\pi\pi$ is constructed. The eigenstates $|\pi\pi, E_n\rangle$ of the operator $(\pi\pi)^\dagger(0)$ can be represented as

$$|\pi\pi, E_n\rangle = \frac{1}{\sqrt{2}} (|\pi^+(\vec{p}_{1n})\pi^-(\vec{p}_{2n})\rangle - |\pi^+(\vec{p}_{2n})\pi^-(\vec{p}_{1n})\rangle) \quad (5.7)$$

where \vec{p}_{1n} and \vec{p}_{2n} are the momenta of the interacting two pions.

The Ward identity in the continuum

$$\partial_\mu \langle \pi^+(\vec{p}_{1n})\pi^-(\vec{p}_{2n}) | \bar{\psi}\gamma_\mu\psi | \Omega \rangle = 0 \quad (5.8)$$

together with the equation

$$\langle \pi^+(\vec{p}_{1n})\pi^-(\vec{p}_{2n})|\bar{\psi}\gamma_0\psi|\Omega\rangle = 0 \quad (5.9)$$

yields

$$(\vec{p}_{1n} + \vec{p}_{2n}) \cdot \langle \pi^+(\vec{p}_{1n})\pi^-(\vec{p}_{2n})|\bar{\psi}\vec{\gamma}\psi|\Omega\rangle = 0 . \quad (5.10)$$

This equation can be equivalently written as

$$\langle \pi^+(\vec{p}_{1n})\pi^-(\vec{p}_{2n})|\bar{\psi}\vec{\gamma}\psi|\Omega\rangle = F(\vec{p}_{1n}, \vec{p}_{2n})(\vec{p}_{1n} - \vec{p}_{2n}) , \quad (5.11)$$

where $F(\vec{p}_{1n}, \vec{p}_{2n})$ is a form factor. Eq. (5.5) and (5.11) together yield

$$\langle \pi^+(\vec{p}_{1n})\pi^-(\vec{p}_{2n})|\rho^\dagger(0)|\Omega\rangle = F(\vec{p}_{1n}, \vec{p}_{2n})(\vec{a} \cdot (\vec{p}_{1n} - \vec{p}_{2n})) . \quad (5.12)$$

Using Eq. (5.12), one can rewrite the off-diagonal correlator as

$$\begin{aligned} \langle \Omega|(\pi\pi)(t)\rho^\dagger(0)|\Omega\rangle &= \sum_n \frac{1}{\sqrt{2}} a_n (\vec{a} \cdot (\vec{p}_{1n} - \vec{p}_{2n})) \\ &\quad \times (F(\vec{p}_{1n}, \vec{p}_{2n}) - F(\vec{p}_{2n}, \vec{p}_{1n})) e^{-E_n t} . \end{aligned} \quad (5.13)$$

Eq. (5.13) shows that, to get the best signal, one should choose the vector \vec{a} parallel to the relative momentum $\vec{p}_{1n} - \vec{p}_{2n}$, $n = 1, 2$ in order to have an optimal overlap with the state to be extracted. However, in the case of interacting particles, we do not know $\vec{p}_{1n} - \vec{p}_{2n}$ in advance. Considering the fact that the momentum shift δp is proportional to $L^{-3/2}$, which is a small correction to free lattice momentum $\sim 2\pi/L$ for large lattice size L , we use the relative momentum of free particles instead. Therefore, the polarization vector \vec{a} is taken to be parallel to \vec{e}_3 in the CMF, \vec{e}_3 in the MF1 and $\vec{e}_1 + \vec{e}_2$ in the MF2, respectively.

5.2.2 Extraction of energies

The construction of the correlation matrix (5.2) provides us an effective approach to calculate both the ground state energy E_1 and the first excited state energy E_2 . Here we describe how this is achieved.

Inserting a complete set of eigenstates of \hat{H} into the correlation matrix $C_{2 \times 2}(t)$ yields

$$C_{ij}(t) = \langle \Omega|\mathcal{O}_i(t)\mathcal{O}_j^\dagger(0)|\Omega\rangle = \sum_{n=1}^2 V_{in} e^{-E_n t} V_{jn}^\dagger + O(e^{-E_n > 2t}) , \quad (5.14)$$

where $\mathcal{O}_i(t)$ ($i = 1, 2$) represents $\pi\pi(t)$ and $\rho(t)$, respectively. The 2×2 matrix V_{in} is defined as

$$V_{in} = \langle \Omega | \mathcal{O}_i(t) | n \rangle , \quad (5.15)$$

where $|n\rangle$ ($n = 1, 2$) denotes the n -th eigenstate, which are normalized such that $\langle m | n \rangle = \delta_{mn}$.

A variational principle [23] is formulated by ($t > t_R$)

$$R(t, t_R) = C_{2 \times 2}(t) C_{2 \times 2}^{-1}(t_R) = V \bar{R}(t, t_R) V^{-1} + O(e^{-E_{n>2} t_R}) \quad (5.16)$$

where t_R is a reference time slice. It is assumed to be large enough such that the contributions to the matrix $R(t, t_R)$ from the excited states with $E_{n>2}$ can be ignored. $\bar{R}(t, t_R)$ is a diagonal matrix

$$\bar{R}(t, t_R) = \begin{pmatrix} R_1(t, t_R) & & \\ & R_2(t, t_R) & \\ & & \dots \end{pmatrix} = \begin{pmatrix} e^{-E_1(t-t_R)} & & \\ & e^{-E_2(t-t_R)} & \\ & & \dots \end{pmatrix} . \quad (5.17)$$

Therefore, by diagonalizing the matrix $R(t, t_R)$, one can extract the energy eigenvalues of E_n ($n = 1, 2$) from the Euclidean time dependence of the matrix elements $R_n(t, t_R)$

$$V^{-1} R(t, t_R) V \Rightarrow \bar{R}(t, t_R) \Rightarrow R_n(t, t_R) = \exp(-E_n(t - t_R)) , \quad n = 1, 2 , \quad (5.18)$$

where we assume that t is far enough from the boundaries to ignore boundary effects.

Using the variational method we are able to isolate the ground state and first excited state in a clean way. This is of particular importance in the resonance region, where the avoided level crossing occurs and the first excited state is possibly close to the ground state. Such a situation renders the extraction of the ground state energy unsuccessful when only a single exponential fit ansatz is used.

5.2.3 Anti-periodic boundary conditions

In the present work we use anti-periodic boundary conditions for quarks in the time direction, which results in a more complicated time dependence for the correlation matrix $C_{2 \times 2}(t)$.

Here, we follow the analysis made in Sect. 4.2.2. Due to the boundary condition effects, the matrix elements $C_{ij}(t)$ are then given by

$$\begin{aligned} C_{ij}(t) &= \text{Tr} \left(e^{-\hat{H}(T-t)} \mathcal{O}_i(0) e^{-\hat{H}t} \mathcal{O}_j^\dagger(0) \right) / Z \\ &= \sum_{m,n} V_{imn} V_{jmn}^\dagger e^{-(E_m+E_n)T/2} \cosh((E_m - E_n)(t - T/2)) / Z, \end{aligned} \quad (5.19)$$

where the elements V_{imn} are defined by

$$V_{imn} = \langle m | \mathcal{O}_i(t) | n \rangle. \quad (5.20)$$

Among the two states $|m\rangle$ and $|n\rangle$, if one is the vacuum state and the other is a physical state, e.g. $E_m = 0$ and $E_n > 0$, then from the t dependence of the correlator, $\cosh(E_n(t - T/2))$, we extract the energy of the physical state, E_n . If neither of them is the vacuum state ($E_m > 0$, $E_n > 0$), then from the correlator, we extract the energy of $E_m - E_n$, which is not the energy of any physical state. In the case with a finite time extent T , those terms with $E_m > 0$ and $E_n > 0$ (although thermally suppressed) do not vanish and they can distort the behavior of the correlation functions $C_{ij}(t)$, particularly in the large t region.

This phenomenon does indeed occur here for the operator \mathcal{O}_i ($i = 1, 2$). In the CMF, intermediate states $\langle n | = \langle \pi^+, (2\pi/L)\vec{e}_3 |$ and $\langle m | = \langle \pi^+, (2\pi/L)\vec{e}_3 |$ give a constant, in t , contribution to the correlation matrix because the energies of $|m\rangle$ and $|n\rangle$ are equal,

$$\langle m | \mathcal{O}_i | n \rangle \langle n | \mathcal{O}_j^\dagger | m \rangle e^{-E_{\pi\pi}^0 T/2} / Z, \quad E_{\pi\pi}^0 = 2E_\pi(\vec{p}), \quad \vec{p} = (2\pi/L)\vec{e}_3, \quad (5.21)$$

where $E_\pi(\vec{p})$ denotes the energy of a pion with momentum \vec{p}

$$E_\pi(\vec{p}) = \sqrt{m_\pi^2 + \vec{p}^2}. \quad (5.22)$$

In the MFs, intermediate states $\langle n | = \langle \pi^+, \vec{P} |$ and $\langle m | = \langle \pi^+, \vec{0} |$ give a contribution to the correlation matrix through

$$\langle m | \mathcal{O}_i | n \rangle \langle n | \mathcal{O}_j^\dagger | m \rangle e^{-E_{\pi\pi}^0 T/2} \cosh((E_\pi(\vec{P}) - m_\pi)(t - T/2)) / Z, \quad E_{\pi\pi}^0 = m_\pi + E_\pi(\vec{P}). \quad (5.23)$$

On the other hand, the standard contributions are given by

$$\langle \Omega | \mathcal{O}_i | E_n \rangle \langle E_n | \mathcal{O}_j^\dagger | \Omega \rangle e^{-E_n T/2} \cosh(E_n(t - T/2)) / Z. \quad (5.24)$$

The lowest two energy eigenvalues are approximately the ρ -resonance energy and the energy of a pion-pion scattering state

$$E_1 = E_\rho(\vec{P}) , \quad E_2 = E_{\pi\pi} \quad \text{or} \quad E_1 = E_{\pi\pi} , \quad E_2 = E_\rho(\vec{P}) . \quad (5.25)$$

For large enough volumes $E_{\pi\pi} = E_{\pi\pi}^0 + \delta E \approx E_{\pi\pi}^0$, and hence the thermally suppressed contributions to the correlation matrix are comparable to the standard ones when t approaches $T/2$.

Since in the MFs, the t dependence of the thermally suppressed contributions is not a constant but a cosh function, the derivative method used in Sect. 4.2.2 fails here. To eliminate unwanted contributions, we remove the data points at very large t -values from our analysis. In this case, the variational method is not spoiled and it yields

$$R_n(t, t_R) \rightarrow A_n \cosh(-E_n(t - T/2)) , \quad n = 1, 2 , \quad \text{for} \quad 0 \ll t \ll T/2 . \quad (5.26)$$

5.3 Lattice calculation

5.3.1 Ensemble information

Most of the results presented here are from a sequence of ensembles with a lattice spacing of $a = 0.079$ fm. The pion masses range from $m_\pi = 480$ MeV to 290 MeV. At all pion masses the physical kinematics of $m_\pi/m_\rho < 0.5$ is satisfied, which indicates that it is physically possible for the ρ to decay into two pions. We will analyze the higher two pion masses at a box size of $L = 1.9$ fm and the lower two pion masses for a larger volume with $L = 2.5$ fm. In addition, we will also perform one calculation at a finer lattice spacing of $a = 0.063$ fm to check for possible lattice spacing artifacts. The parameters relevant for this calculation are given in Table 5.1, and further details concerning the ensembles used can be found in Refs. [29–32].

5.3.2 Various source methods

For the calculation of pion correlation functions, it is known that the stochastic source method is more efficient than the point source method. Therefore, we employ a Z_4 stochastic noise with one noise source ($N_s = 1$) generated on all the time slices $t_s = 0, \dots, T - 1$. We

Ensemble	β	$a\mu$	L/a	m_π	m_π/m_ρ	N
A_1	3.90	0.0085	24	480	0.43(1)	176
A_2	3.90	0.0064	24	420	0.40(1)	278
A_3	3.90	0.0040	32	330	0.32(1)	124
A_4	3.90	0.0030	32	290	0.30(1)	129
B_1	4.05	0.0030	32	320	0.32(2)	138

Table 5.1: Ensembles used in the $I = 1$ pion-pion scattering. We give the ensemble name i.e. A_i, B_1 , the inverse bare coupling $\beta = 6/g_0^2$, the bare quark mass $a\mu$, the lattice size L/a and the value of m_π in units of MeV. We also list the ratio m_π/m_ρ and the number N of configurations used.

perform T inversions for each configuration and each momentum mode. With the available propagators, the correlator $C_{11}(t)$ can be calculated as

$$C_{11}(t) = \left\langle (\pi\pi)(t) (\pi\pi)^\dagger(0) \right\rangle = \frac{1}{T} \sum_{t_s} \left\langle (\pi\pi)(t+t_s) (\pi\pi)^\dagger(t_s) \right\rangle. \quad (5.27)$$

The rather large effort to generate propagators on all the time slices pays off because with these propagators we obtain the correlators with high precision.

In the calculation of the off-diagonal correlator, $C_{21}(t)$, the contraction of the quark fields leads to a three-point diagram. Since the two pion interpolating operators are located at the same source time slice t_s , we use the sequential propagator method to construct the correlator. We calculate $C_{21}(t)$ as

$$C_{21}(t) = \left\langle \rho(t) (\pi\pi)^\dagger(0) \right\rangle = \frac{1}{T} \sum_{t_s} \left\langle \rho(t+t_s) (\pi\pi)^\dagger(t_s) \right\rangle, \quad (5.28)$$

and average the correlator over all time slices t_s . For the other off-diagonal correlator $C_{12}(t)$, the two pion interpolating operators are placed at the sink time slice $t+t_s$ which would require T sequential propagators for each source time slice, leading to another large computational effort. However, using the relation $C_{12}(t) = C_{21}^\dagger(t)$, we can substitute $C_{12}(t)$ by $C_{21}^\dagger(t)$ in our calculations thus saving a lot of computer time.

For the rho-rho correlator, $C_{22}(t)$, we performed a comparison between the Z_4 stochastic source method and the point source method and found that the results look similar in terms of the required computational effort for a given signal to noise ratio. Historically, we started our work with the calculation of the hadronic vacuum polarization, see Chapter 6. In that

work, we have generated point source propagators at the parameters listed in Table 5.1. Since we did not observe any advantage of stochastic Z_4 sources, we used these available propagators to construct the rho-rho correlator

$$C_{22}(t) = \left\langle \rho^\dagger(t + t_s)\rho(t_s) \right\rangle, \quad (5.29)$$

where the source time slices, t_s , are chosen randomly to reduce the autocorrelation between consecutive trajectories.

Due to the isospin symmetry breaking effects at non-zero lattice spacing, the disconnected diagram does not vanish. To address its contribution to the neutral ρ -meson, we need to generate additional all-to-all propagators. However, the disconnected diagram correction has been studied in Ref. [105], and found to be negligible. Therefore, we neglect it also here in the rho-rho correlator. In the calculation of correlator $\langle(\pi\pi)(\pi\pi)^\dagger\rangle$, we are able to address the disconnected diagram since we put stochastic sources on each time slice. We find that the disconnected diagram makes only a small contribution to the correlator but brings in a significant noise. Since from all existing investigations it appears that the disconnected contributions are negligibly small, we leave them out in the whole 2×2 correlation matrix.

5.4 Results

5.4.1 Energy eigenvalues

In Fig. 5.1–5.5 we show our lattice results for $R_n(t, t_R)$ ($n = 1, 2$) defined in Eq. (5.18) in the CMF, MF1 and MF2, as a function of the time t together with a correlated fit to the asymptotic form given in Eq. (5.26). There are two main sources of systematic errors. One originates from the higher excited states and affects the correlator in the low- t region. The other arises from the unwanted thermal contributions, which distorts the correlator in the large- t region. By tuning the beginning t_{\min} and the end t_{\max} of the fitting window, we can control the systematic errors effectively and ensure the fitting results are safe from these systematic effects. In our calculations, we set t_{\min} to be $t_R + 1$, where t_R is the reference time slice given in Eq. (5.16), and increase t_R to reduce the higher excited state contaminations. Besides this, we set t_{\max} to be sufficiently far away from the time

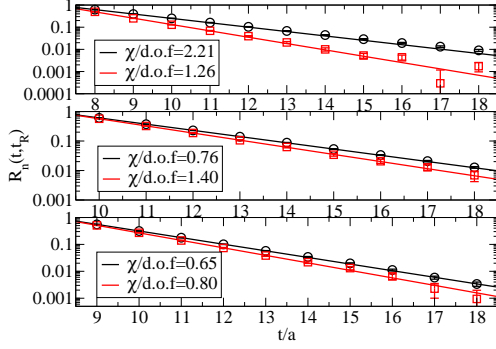


Figure 5.1: For ensemble A_1 , the correlator $R_n(t, t_R)$ ($n = 1, 2$) as a function of t . From top to bottom, the three plots present the lattice calculations in the CMF, MF1 and MF2, respectively. The solid lines are correlated fits to Eq. (5.26), from which the energy eigenvalues E_n are extracted.

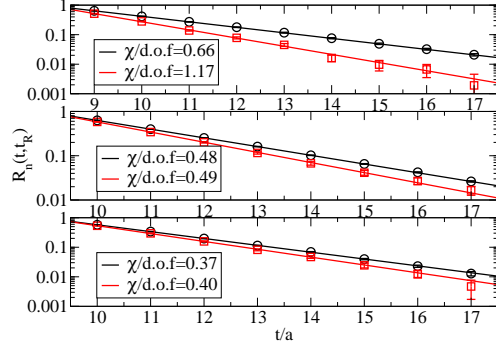


Figure 5.2: For ensemble A_2 , the correlator $R_n(t, t_R)$ ($n = 1, 2$) as a function of t . From top to bottom, the three plots present the lattice calculations in the CMF, MF1 and MF2, respectively. The solid lines are correlated fits to Eq. (5.26), from which the energy eigenvalues E_n are extracted.

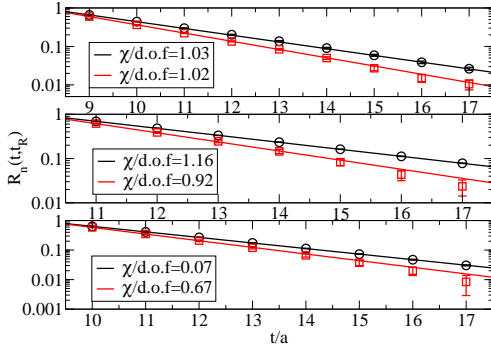


Figure 5.3: For ensemble A_3 , the correlator $R_n(t, t_R)$ ($n = 1, 2$) as a function of t . From top to bottom, the three plots present the lattice calculations in the CMF, MF1 and MF2, respectively. The solid lines are correlated fits to Eq. (5.26), from which the energy eigenvalues E_n are extracted.

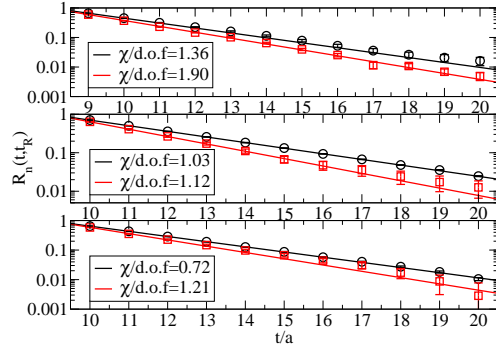


Figure 5.4: For ensemble A_4 , the correlator $R_n(t, t_R)$ ($n = 1, 2$) as a function of t . From top to bottom, the three plots present the lattice calculations in the CMF, MF1 and MF2, respectively. The solid lines are correlated fits to Eq. (5.26), from which the energy eigenvalues E_n are extracted.

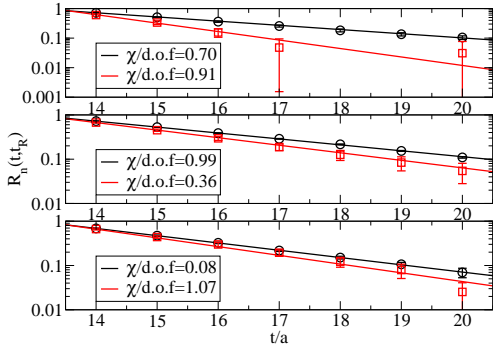


Figure 5.5: For ensemble B_1 , the correlator $R_n(t, t_R)$ ($n = 1, 2$) as a function of t . From top to bottom, the three plots present the lattice calculations in the CMF, MF1 and MF2, respectively. The solid lines are correlated fits to Eq. (5.26), from which the energy eigenvalues E_n are extracted.

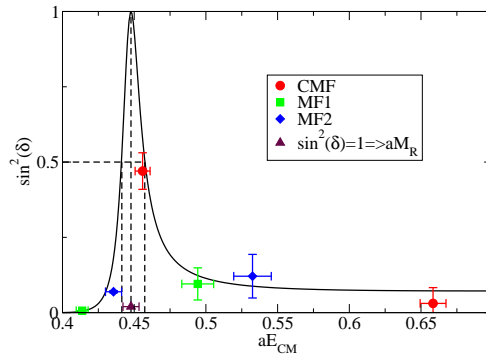


Figure 5.6: For ensemble A_1 , the scattering phases calculated in the CMF, MF1 and MF2 together with the effective range formula fit. At the positions where the scattering phase passes $\pi/2$ and $\pi/4$, the resonance mass m_ρ and the decay width Γ_ρ can be determined.

slice $t = T/2$ in order that the fitting results are protected from the unwanted thermal contributions. The corresponding parameters t_R , t_{\min} and t_{\max} used in this work are listed in Table. 5.4. All the ensembles shown in Fig. 5.1–5.5 visibly agree with the corresponding fit and lead to reasonable values of χ^2/dof . The fit quality χ^2/dof together with the fit results for E_n ($n = 1, 2$) are also given in Table 5.4.

5.4.2 Lattice discretization effects

In the continuum limit, the center-of-mass energy E_{CM} is simply related to the energy spectrum E_n ($n = 1, 2$) through the Lorentz transformation (5.1). On the lattice, the discretization effects explicitly break the Lorentz symmetry and the determination of E_{CM} suffers from such discretization errors. Another source of discretization errors arises from the FSM. It uses the continuum dispersion relation

$$E_{CM} = 2\sqrt{m_\pi^2 + p^2} \quad (5.30)$$

to relate energy E_{CM} to the relative momentum p between the two interacting particles. On the lattice, such relation should be modified.

These two sources of systematic errors have been studied in Ref. [54], where the authors

suggest to use the lattice modified relations

$$\begin{aligned}\cosh(E_{CM}) &= \cosh(E_n) - 2 \sum_i \sin^2(P_i/2), \quad n = 1, 2, \\ \cosh(E_{CM}/2) &= 2 \sin^2(p/2) + \cosh(m_\pi),\end{aligned}\tag{5.31}$$

instead of the continuum ones to reduce the systematic errors. Following this suggestion, we calculate the energy E_{CM} and the momentum p from the energy eigenvalues E_n using Eq. (5.31) and then estimate the P-wave scattering phase $\delta_1(p)$ by putting p into Eq. (3.84–3.86). The results for E_{CM} , p , $\delta_1(p)$ and $\sin^2 \delta_1$ are given in Table 5.5.

Here, we want to add a word of caution. The FSMs are valid for *elastic* scattering processes. In a situation with too high energy, i.e. when $E_{CM} > 4m_\pi$, the *inelastic scattering* channel will open and an unknown systematic error will affect the determination of the scattering phase. In our calculations, we exclude the results with energy $E_{CM} \gtrsim 4m_\pi$ and thus make use of the finite size formula in a safe way.

5.4.3 Extraction of resonance parameters

So far, we collected the P-wave scattering phases at six different energy levels, two from each of the three Lorentz frames employed. In order to interpret these results, we still need an analytic expression that describes the dependence of the scattering phase on the center-of-mass energy E_{CM} . Usually, one employs the effective range formula [106] to meet this demand

$$\tan \delta_1(p) = \frac{g_{\rho\pi\pi}^2}{6\pi} \frac{p^3}{E_{CM}(m_\rho^2 - E_{CM}^2)}, \quad p = \sqrt{E_{CM}^2/4 - m_\pi^2},\tag{5.32}$$

where $g_{\rho\pi\pi}$ is the effective $\rho \rightarrow \pi\pi$ coupling constant, which largely determines the size of the ρ -meson decay width through

$$\Gamma_\rho = \frac{g_{\rho\pi\pi}^2}{6\pi} \frac{p_\rho^3}{m_\rho^2}, \quad p_\rho = \sqrt{m_\rho^2/4 - m_\pi^2}.\tag{5.33}$$

In Eq. (5.32), the center-of-mass energy E_{CM} and the momentum p satisfy the dispersion relation in the continuum. Since we are working on the lattice, this relation does not hold due to discretization effects and we therefore employ the lattice dispersion relation (5.31), as described earlier.

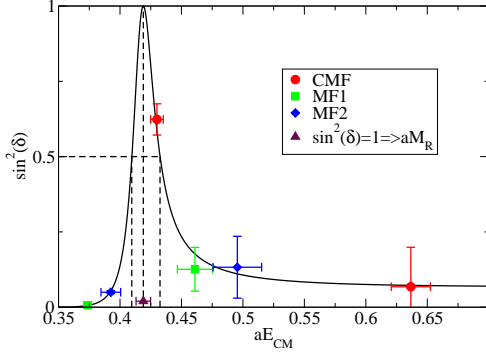


Figure 5.7: For ensemble A_2 , the scattering phases calculated in the CMF, MF1 and MF2 together with the effective range formula fit. At the positions where the scattering phase passes $\pi/2$ and $\pi/4$, the resonance mass m_ρ and the decay width Γ_ρ can be determined.

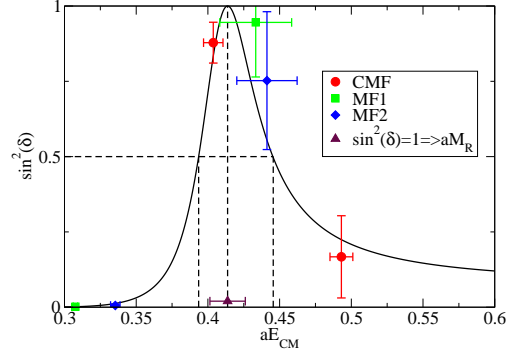


Figure 5.8: For ensemble A_3 , the scattering phases calculated in the CMF, MF1 and MF2 together with the effective range formula fit. At the positions where the scattering phase passes $\pi/2$ and $\pi/4$, the resonance mass m_ρ and the decay width Γ_ρ can be determined.

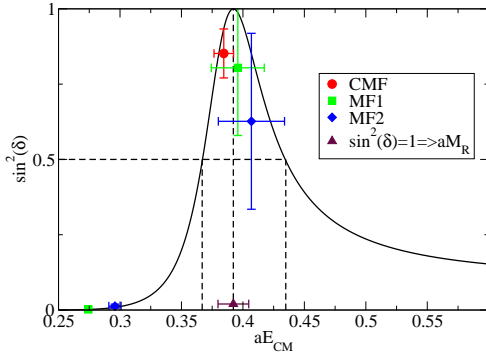


Figure 5.9: For ensemble A_4 , the scattering phases calculated in the CMF, MF1 and MF2 together with the effective range formula fit. At the positions where the scattering phase passes $\pi/2$ and $\pi/4$, the resonance mass m_ρ and the decay width Γ_ρ can be determined.

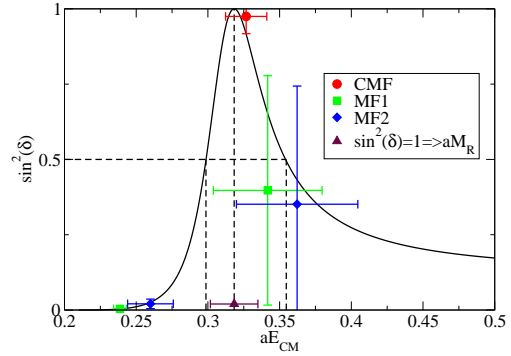


Figure 5.10: For ensemble B_1 , the scattering phases calculated in the CMF, MF1 and MF2 together with the effective range formula fit. At the positions where the scattering phase passes $\pi/2$ and $\pi/4$, the resonance mass m_ρ and the decay width Γ_ρ can be determined.

	m_π (MeV)	m_ρ (MeV)	Γ_ρ (MeV)	$g_{\rho\pi\pi}$
A_1	480	1118(14)	39.5(8.2)	6.46(40)
A_2	420	1047(15)	55(11)	6.19(42)
A_3	330	1033(31)	123(43)	6.31(87)
A_4	290	980(31)	156(41)	6.77(67)
B_1	320	997(52)	158(68)	7.3(1.1)

Table 5.2: The results for the ρ -resonance mass m_ρ , the decay width Γ_ρ and the effective $\rho \rightarrow \pi\pi$ coupling $g_{\rho\pi\pi}$ at pion masses ranging from 480 MeV to 290 MeV.

We fit the results for the scattering phase with the effective range formula and show the corresponding fits in Figs. 5.6–5.10. At the position where the scattering phase passes $\pi/2$, the resonance mass m_ρ is determined. Additionally, the values of $g_{\rho\pi\pi}$ and hence Γ_ρ are also evaluated from the fit. The corresponding results are given in Table 5.2.

5.4.4 Isospin symmetry breaking

As we have mentioned in the previous chapters, twisted mass Lattice QCD violates the isospin and parity symmetries at any non-vanishing value of the lattice spacing. As a result, for any value of $a \neq 0$ it is possible for the ρ -meson to decay into three pions, which means that at non-zero lattice spacing the upper bound of the elastic scattering region is lowered to $3m_\pi$. Additionally, the isospin symmetry breaking causes a mixing between states in the $I = 1$ channel and those in $I = 0$ and $I = 2$ channels. If this effect would be large in our calculation, it would be necessary to adapt Lüscher’s method to the isospin mixing case.

In order to test for possible isospin symmetry breaking effects, we therefore performed our calculations of the ρ resonance parameters at two different lattice spacings. To this end, we have –besides the so far used value of $a = 0.079$ fm– performed an additional calculation of m_ρ and Γ_ρ at a second lattice spacing of $a = 0.063$ fm at a pion mass of 320 MeV. This pion mass lies very close to that of the one obtained at $a = 0.079$ fm and $m_\pi = 330$ MeV. The physical volumes of these two ensembles differ, so the results cannot be directly compared. However, assuming that the FSM correctly accounts for the finite volume dependence of the energy eigenvalues for these two ensembles, we can

compare the results for the two lattice spacings. We find statistical agreement between the two ensembles as indicated in Table 5.2. So far, this is only a single check and we need to eventually examine the effects of isospin symmetry breaking more carefully, but in this thesis, due to the large statistical errors of our results in Table 5.2, we assume that such systematic errors are small compared to the statistical ones.

5.4.5 Quark mass dependence

We now discuss the quark mass dependence of the ρ resonance parameters. There are several references from effective field theory (EFT) for the quark mass dependence of the ρ -meson [107–110], that can guide the extrapolation of m_ρ and Γ_ρ in quark mass through

$$\begin{aligned} m_\rho &= M_\rho^0 + C_{m1}M_\pi^2 + C_{m2}M_\pi^3 + C_{m3}M_\pi^4 \ln(M_\pi^2) + O(M_\pi^4), \\ \Gamma_\rho &= \Gamma_\rho^0 + C_{\Gamma1}M_\pi^2 + C_{\Gamma2}M_\pi^3 + C_{\Gamma3}M_\pi^4 \ln(M_\pi^2) + O(M_\pi^4). \end{aligned} \quad (5.34)$$

Note that m_ρ and Γ_ρ are not only statistically correlated, but also inherently related to each other, suggesting that the coefficients C_{mi} and $C_{\Gamma i}$ ($i=1,2,3$) might not be completely independent (see the following EFT description as an example). In this work we will follow the EFT [111] description where m_ρ and Γ_ρ are considered as the real and imaginary part of the complex pole of the ρ -meson propagator. We therefore introduce the complex pole parameter Z defined through

$$Z = (m_\rho - i\Gamma_\rho/2)^2. \quad (5.35)$$

The power counting in the EFT is addressed by using the complex-mass renormalization scheme, under which Z is written perturbatively as a loop expansion

$$Z = Z^{(0)} + Z^{(1)} + Z^{(2)} + \dots. \quad (5.36)$$

Each of these terms has its own chiral expansion. Up to third order in the chiral expansion, they read [111]

$$\begin{aligned} Z^{(0)} &= Z_\chi + C_\chi M_\pi^2, \quad Z_\chi = (M_\chi - i\Gamma_\chi)^2, \quad C_\chi = C_1 + iC_2 \\ Z^{(1)} &= \frac{g^2 M_\pi^4}{16\pi^2 Z_\chi} \left(3 - 2 \ln \frac{M_\pi^2}{M_\chi^2} - 2i\pi \right) - \frac{g_{\omega\rho\pi}^2 M_\pi^3 (M_\chi - i\Gamma_\chi/2)}{24\pi} - \frac{g_{\omega\rho\pi}^2 M_\pi^4 \left(\ln \frac{M_\pi^2}{M_\chi^2} - 1 \right)}{32\pi^2} \end{aligned} \quad (5.37)$$

with the real parameters M_χ , Γ_χ , C_1 , C_2 , $g_{\omega\rho\pi}^2$ and g^2 . Using the pion mass dependence of Z , we can determine Z_{phy} at the physical point, which can be converted to the physical resonance mass $m_{\rho,\text{phy}}$ and decay width $\Gamma_{\rho,\text{phy}}$.

In our calculation, the statistical errors of our lattice determination of the ρ resonance parameters are still large. In addition, the lightest pion mass used in our calculations is about 300 MeV where it is unclear whether the formulae derived in the EFTs are applicable. Thus, as a starting point, we consider only the leading term $Z^{(0)}$ in expansion (5.36) and study the quark mass dependence of the ρ -meson using the simplest linear polynomial in M_π^2

$$Z = Z_\chi + C_\chi M_\pi^2 . \quad (5.38)$$

The fitting results are listed in Table 5.3.

Fit	$m_{\rho,\text{phy}}$	$\Gamma_{\rho,\text{phy}}$	M_χ	Γ_χ	C_1	C_2	$g_{\omega\rho\pi}$
Eq. (5.38)	0.91(3)	0.18(3)	0.89(04)	0.19(4)	2.0(0.3)	0.6(2)	—
Eq. (5.39)	0.90(8)	0.18(3)	0.88(11)	0.19(4)	2.3(3.9)	0.5(4)	7(39)

Table 5.3: The ρ mass and decay width from the chiral extrapolations of different models. The values of $m_{\rho,\text{phy}}$, $\Gamma_{\rho,\text{phy}}$, M_χ , Γ_χ are given in units of GeV and $g_{\omega\rho\pi}$ in units of GeV^{-1} .

In the left panel of Fig. 5.11 we plot the mass of the ρ -meson as a function of the square of the pion mass together with the linear fit (5.38). Using this simple linear extrapolation, our lattice result turns out to lie high relative to the PDG value of the ρ -meson. We try a more sophisticated fit, in which we include the term $Z^{(1)}$ in Eq. (5.36). Note that in the chiral expansion (5.37) of $Z^{(1)}$, the dominant term is M_π^3 and the terms $M_\pi^4 \ln(M_\pi^2/M_\chi^2)$ and M_π^4 are more suppressed in the chiral limit. We therefore fit our lattice results to the asymptotic form

$$Z = Z_\chi + C_\chi M_\pi^2 - \frac{1}{24\pi} g_{\omega\rho\pi}^2 Z_\chi^{1/2} M_\pi^3 . \quad (5.39)$$

The fit results are also listed in Table 5.3. We find that the signal-to-noise ratio of $g_{\omega\rho\pi}$ is terribly poor. Therefore it is impossible to include even higher order terms in the fit. We plot the mass of the ρ -meson as a function of the square of the pion mass together

with the fit to Eq. (5.39) in the right panel of Fig 5.11. Although the result for the ρ mass is still high relative to the PDG value, the error band becomes much larger compared to the linear fit, especially in the low pion mass region. It suggests that the study of the ρ -resonance at yet lighter quark masses is very important to understand the chiral dynamics of the ρ -resonance. Besides this, it also indicates that a more precise comparison with experiment will require reducing the statistical errors and fitting the lattice results to more sophisticated chiral extrapolation formulae.

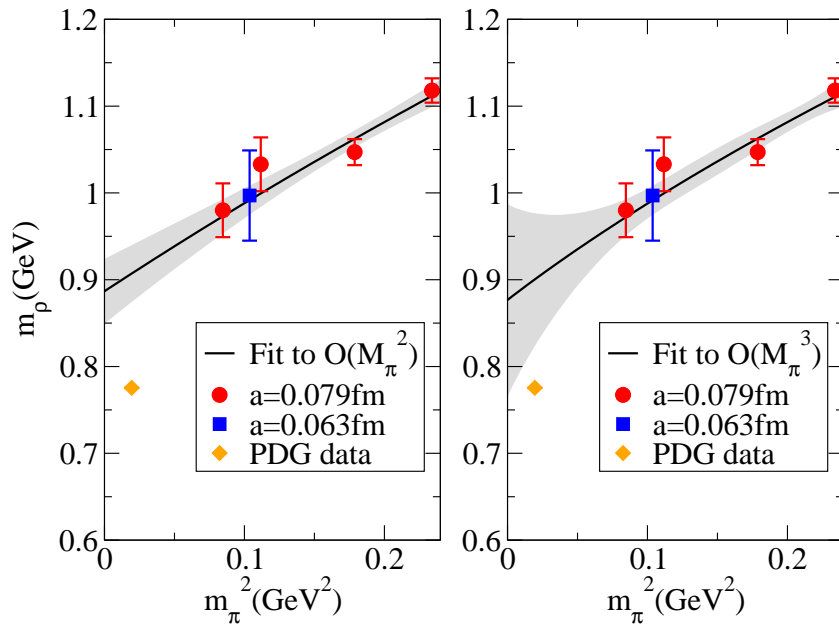


Figure 5.11: The ρ -meson mass as a function of the square of the pion mass. In the left panel, we fit the lattice results to Eq. (5.38). On the right panel, we fit them to Eq. (5.39).

In Fig. 5.12, we plot the coupling $g_{\rho\pi\pi}$ as a function of the square of the pion mass and find that $g_{\rho\pi\pi}$ is almost independent of the pion mass. Moreover, the value of $g_{\rho\pi\pi}$ is consistent with the PDG value. Since the decay width is largely determined by the coupling $g_{\rho\pi\pi}$, the consistency of $g_{\rho\pi\pi}$ with the experimental value also implies that the lattice determination of the decay width $\Gamma_{\rho,\text{phy}}$ should agree with the PDG value. This can indeed be inferred from Fig. 5.13, where we show the lattice results for Γ_ρ as a function of

the square of the pion mass together with the linear fit (5.38) in the left panel and with the fit to Eq. (5.39) in the right panel. We find that including the M_π^3 term has only a slight effect on the determination of Γ_ρ . At the physical point, the decay width Γ_ρ turns out to be the same for the two fits and is given as

$$\Gamma_{\rho,\text{phy}} = 178(32) \text{ MeV} , \quad (5.40)$$

which is consistent with the PDG value within 1σ

$$\Gamma_{\rho,\text{PDG}} = 149.1(0.8) \text{ MeV} . \quad (5.41)$$

Note, however, that the value determined from our lattice calculation is much less accurate than the one extracted from experimental measurements. Therefore, we consider the present work more as an initial study of whether and how resonance parameters can be extracted from non-perturbative lattice calculations and not as a precise determination of these parameters. The results we have obtained here demonstrate, however, that resonances can indeed be analyzed on finite size lattices with numerical calculations. This is very promising, given the number of hadrons that appear in the physical spectrum in QCD as resonances.

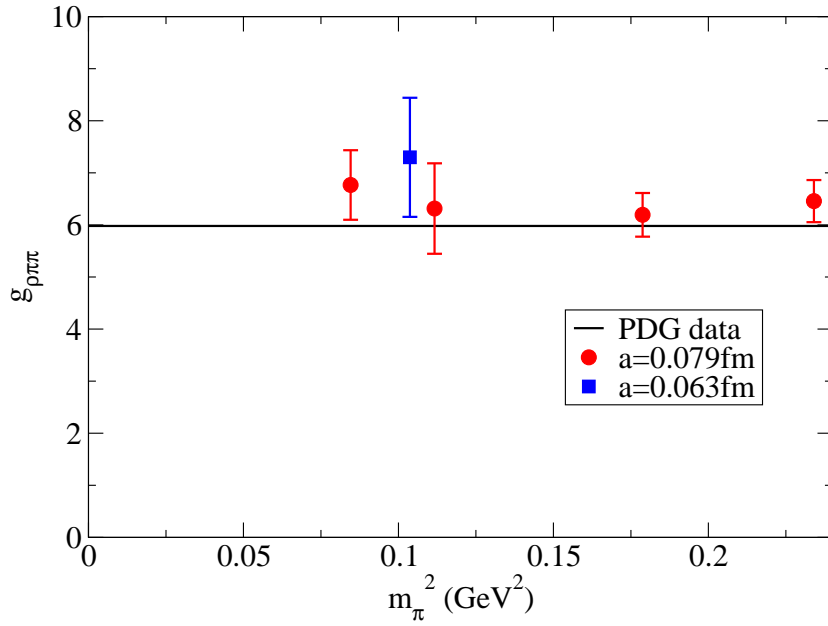


Figure 5.12: The effective coupling $g_{\rho\pi\pi}$ as a function of the square of the pion mass.

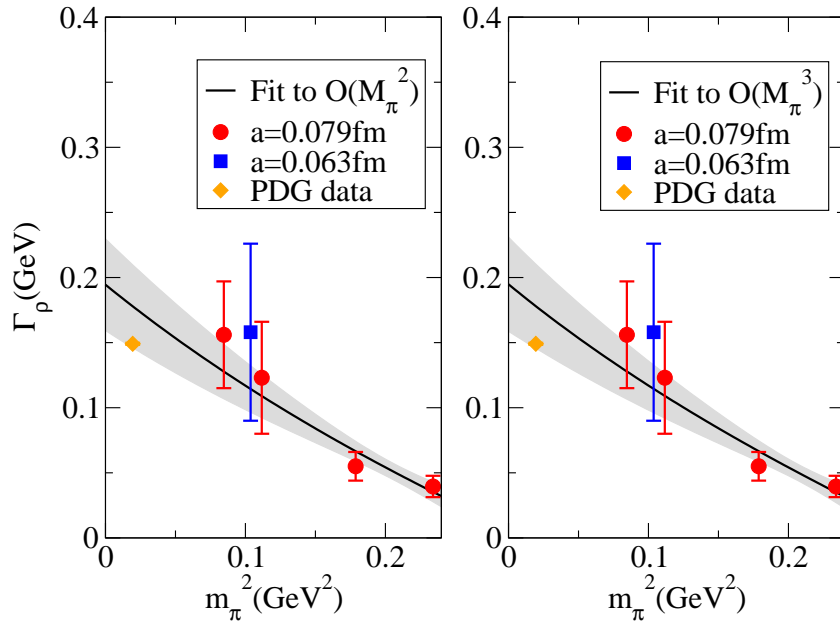


Figure 5.13: The ρ decay width as a function of the square of the pion mass. In the left panel, we fit the lattice results to Eq. (5.38). On the right panel, we fit them to Eq. (5.39).

	Frame	t_R/a	t_{\min}/a	t_{\max}/a	n	χ^2/dof	aE_n
A_1	CMF	7	8	18	1	2.21	0.4559(52)
					2	1.26	0.6584(90)
	MF1	9	10	18	1	0.76	0.4869(35)
					2	1.40	0.5563(98)
	MF2	8	9	18	1	0.65	0.5660(42)
					2	0.80	0.642(11)
A_2	CMF	8	9	17	1	0.66	0.4301(52)
					2	1.17	0.637(16)
	MF1	9	10	17	1	0.48	0.4537(25)
					2	0.49	0.527(12)
	MF2	9	10	17	1	0.37	0.5343(57)
					2	0.40	0.612(16)
A_3	CMF	8	9	17	1	1.03	0.4037(68)
					2	1.02	0.4931(80)
	MF1	10	11	17	1	1.16	0.3638(13)
					2	0.92	0.474(23)
	MF2	9	10	17	1	0.07	0.4330(25)
					2	0.67	0.518(18)
A_4	CMF	8	9	20	1	1.36	0.3844(79)
					2	1.90	0.4591(86)
	MF1	9	10	20	1	1.03	0.3363(14)
					2	1.12	0.440(19)
	MF2	9	10	20	1	0.72	0.4035(36)
					2	1.21	0.490(22)
B_1	CMF	13	14	20	1	0.70	0.327(14)
					2	0.91	0.66(14)
	MF1	13	14	20	1	0.99	0.3081(34)
					2	0.36	0.393(33)
	MF2	13	14	20	1	0.08	0.378(11)
					2	1.07	0.454(33)

Table 5.4: Extraction of energy eigenvalues for the ground state and the first excited state in the CMF, MF1 and MF2. In the table we list the ensemble number, the reference time t_R , the beginning and end of the fitting window, t_{\min} and t_{\max} , the fit quality χ^2/dof and the fit results for energy eigenvalues E_n ($n = 1, 2$).

Frame	n	aE_n	aE_{CM}	ap	$\delta_1(^{\circ})$	$\sin^2 \delta_1$	
A_1	CMF	1	0.4559(52)		0.1207(50)	136.7(3.5)	0.470(61)
		2	0.6584(90)		0.2686(57)	169.9(8.7)	0.031(52)
	MF1	1	0.4869(35)	0.4137(41)	0.0729(61)	4.66(29)	0.00661(83)
		2	0.5563(98)	0.494(11)	0.1543(91)	162.0(5.2)	0.095(53)
	MF2	1	0.5660(42)	0.4356(56)	0.1000(62)	15.28(40)	0.0694(36)
		2	0.642(11)	0.533(13)	0.1838(97)	159.6(6.4)	0.121(72)
A_2	CMF	1	0.4301(52)		0.1331(42)	127.9(3.1)	0.623(52)
		2	0.637(16)		0.2719(96)	165(15)	0.07(13)
	MF1	1	0.4537(25)	0.3737(31)	0.0794(36)	4.425(41)	0.00595(11)
		2	0.527(12)	0.461(14)	0.157(11)	159.2(6.3)	0.126(73)
	MF2	1	0.5343(57)	0.3925(80)	0.0997(79)	12.89(65)	0.0497(49)
		2	0.612(16)	0.495(20)	0.182(14)	158.6(8.7)	0.13(10)
A_3	CMF	1	0.4037(68)		0.1516(46)	69.6(5.9)	0.878(68)
		2	0.4931(80)		0.2081(48)	156(10)	0.17(14)
	MF1	1	0.3638(13)	0.3076(15)	0.0761(16)	2.40(42)	0.00176(61)
		2	0.474(23)	0.433(25)	0.171(16)	103(22)	0.95(18)
	MF2	1	0.4330(25)	0.3354(33)	0.1013(27)	4.3(1.5)	0.0057(40)
		2	0.518(18)	0.441(21)	0.176(13)	120(15)	0.75(23)
A_4	CMF	1	0.3844(79)		0.1534(50)	67.4(6.6)	0.852(81)
		2	0.4591(86)*				
	MF1	1	0.3363(14)	0.2743(17)	0.0726(15)	2.43(33)	0.00180(49)
		2	0.440(19)	0.396(22)	0.161(13)	116(16)	0.80(22)
	MF2	1	0.4035(36)	0.2959(50)	0.0915(40)	6.5(1.7)	0.0128(66)
		2	0.490(22)	0.407(27)	0.167(17)	128(17)	0.63(29)
B_1	CMF	1	0.327(14)		0.1272(93)	99(11)	0.975(57)
		2	0.66(14)*				
	MF1	1	0.3081(34)	0.2387(44)	0.0607(43)	3.55(30)	0.00384(64)
		2	0.393(33)	0.342(38)	0.137(24)	141(22)	0.40(38)
	MF2	1	0.378(11)	0.260(16)	0.080(13)	8.2(3.2)	0.021(16)
		2	0.454(33)	0.362(42)	0.149(26)	144(24)	0.35(39)

Table 5.5: P-wave scattering phase $\delta_1(p)$ at the energies of the ground state and the first excited state in the CMF, MF1 and MF2. We list the ensemble number, the energy eigenvalue E_n , the center-of-mass energy E_{CM} , the momentum p , the scattering phase $\delta_1(p)$ in units of degree and $\sin^2 \delta_1(p)$. The results marked by a star denotes that the corresponding energy E_{CM} is above the $4m_\pi$ threshold. We therefore exclude them from our calculations.

CHAPTER VI

VACUUM POLARIZATION AND HADRONIC MUON ANOMALOUS MAGNETIC MOMENT

6.1 *Physical background*

In Chapter 1, we discussed the basic motivations for the lattice calculation of the hadronic vacuum polarization function, $\Pi(Q^2)$. First, it can be used to determine the Adler function [9–11], which provides a direct comparison to experimental data of hadronic cross sections. Second, it can be used to compute the hadronic contribution to the muon anomalous magnetic moment, a_μ [18, 96, 97, 112]. Third, combined with a perturbative calculation, it can be used to extract the strong coupling constant, α_s [113, 114]. In this thesis, we will calculate $\Pi(Q^2)$ for pion masses from 640 MeV to 290 MeV using $N_f = 2$ maximally twisted mass fermions [29–32] at two lattice spacings and two physical lattice volumes to address lattice artifacts and finite size effects. Using the lattice determination of $\Pi(Q^2)$, we will then present results for the leading order hadronic contribution to the muon anomalous magnetic moment a_μ .

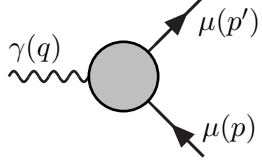
Similar to the electron, the muon is a Dirac fermion with intrinsic spin 1/2. Its magnetic dipole moment is related to its spin through

$$\vec{\mu} = g_\mu \frac{e\hbar}{2m_\mu c} \vec{S}, \quad (6.1)$$

where $\vec{\mu}$ is the magnetic dipole moment, \vec{S} the spin vector and m_μ the mass of the muon. The Dirac theory predicts the value of the Landé g factor for the muon as $g_\mu = 2$ [115, 116]. If one takes relativistic quantum fluctuations (also called *radiative corrections*) into consideration, then g_μ deviates from 2. The difference is the *muon anomalous magnetic moment*. It is defined as

$$a_\mu = (g_\mu - 2)/2. \quad (6.2)$$

Theoretically, the muon anomalous magnetic moment is extracted from the vertex function that describes the electromagnetic interaction of the muon with the photon,



$$\begin{aligned}
 &= (-ie) \bar{u}(p') \Gamma_\mu(q) u(p) \\
 &= (-ie) \bar{u}(p') \left[\gamma^\mu F_1(q^2) + i \frac{\sigma^{\mu\nu} q_\nu}{2m_\mu} F_2(q^2) \right] u(p) , \quad (6.3)
 \end{aligned}$$

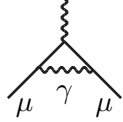
where $q = p' - p$ is the photon momentum, and p and p' are the incoming and outgoing momenta of the muon. The Dirac spinor $u(p)$ denotes the relativistic wave function of a free muon, and the matrix $\sigma^{\mu\nu}$ is given by $\sigma^{\mu\nu} = \frac{i}{2}[\gamma^\mu, \gamma^\nu]$. $F_1(q^2)$ is the *electric charge* or *Dirac form factor* and $F_2(q^2)$ is the *magnetic* or *Pauli form factor*. These form factors describe how the muon interacts with the electromagnetic field. In the static limit, $q^2 \rightarrow 0$, we have

$$g_\mu = 2F_1(0) + 2F_2(0) = 2 + 2F_2(0) , \quad (6.4)$$

where we have used the charge normalization condition $F_1(0) = 1$. Eq. (6.2) and Eq. (6.4) together yield the relation for the anomalous magnetic moment

$$a_\mu = F_2(0) . \quad (6.5)$$

At tree level, $F_2(0)$ is zero. The one-loop correction to $F_2(0)$ originates from quantum fluctuations via the virtual photon-lepton interaction in QED [117]



$$\Rightarrow a_\mu^{\text{QED}(1)} = \frac{\alpha}{2\pi} ,$$

where α is the QED fine structure constant. The higher order corrections, in the perturbative expansion, involve effects from all sectors of the Standard Model (SM) as well as unknown new physics (NP) contributions

$$a_\mu = a_\mu^{\text{SM}} + a_\mu^{\text{NP}} = a_\mu^{\text{QED}} + a_\mu^{\text{Weak}} + a_\mu^{\text{QCD}} + a_\mu^{\text{NP}} . \quad (6.6)$$

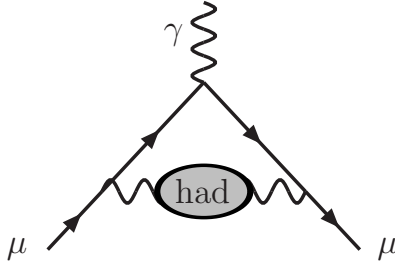


Figure 6.1: Leading hadronic contribution to $g - 2$.

In Eq. (6.6) the NP contributions to a_μ are proportional to

$$\frac{a_\mu^{\text{NP}}}{a_\mu} \propto \frac{m_\mu^2}{M_{\text{NP}}^2}, \quad (6.7)$$

where M_{NP} is the mass of a hypothetical heavy state for some new physics. Eq. (6.7) shows that a_μ is much more sensitive to contributions from new physics than the anomalous magnetic moment of the electron, a_e , since a^{NP} grows quadratically with the considered lepton mass and is hence magnified in a_μ relative to a_e by a factor $(m_\mu/m_e)^2 \sim 4 \times 10^4$. This is what drives a_μ to be a very important quantity for probing new physics.

Today, the anomalous magnetic moment of the muon, a_μ , has been both measured and calculated to high precision. The measurement of the Muon ($g - 2$) Collaboration is $a_\mu^{\text{EX}} = 11\,659\,208.9(6.3) \times 10^{-10}$ [15] and has a fractional accuracy of 0.54×10^{-6} . The Standard Model value a_μ^{SM} has been estimated by many authors. Recent calculations present a discrepancy between a_μ^{SM} and a_μ^{EX} of 3.2σ (e^+e^- -based) [16] or 1.9σ (τ -based) [17]. The dominant source of this variation is the leading order hadronic contribution a_μ^{had} represented in diagram 6.1. This quantity is a pure QCD observable and has been shown to be calculable in Lattice QCD calculations even in Euclidean space-time [18].

The hadronic contribution a_μ^{had} has previously been calculated on the lattice using quenched domain wall fermions [18], quenched improved Wilson fermions [112] and dynamical rooted asqtad improved staggered fermions [96]. In this thesis we present our calculation of a_μ^{had} using two-flavor maximally twisted mass fermions. Since in this calculation we use a different discretization as in Ref. [96], it provides a very important cross-check of the earlier obtained results. In addition, our work is the first to examine finite size effects and lattice artifacts. This allows for a control of most sources of systematic error, which is

necessary for a reliable calculation of a_μ^{had} .

6.2 Determination of a_μ^{had}

6.2.1 Traditional method in Minkowski space

As can be seen in Fig. 6.1, the leading order hadronic contribution a_μ^{had} originates from the hadronic vacuum polarization tensor, which is given by



$$\Rightarrow \Pi_{\mu\nu}(q) = (q_\mu q_\nu - q^2 g_{\mu\nu})\Pi(q^2),$$

where q_μ is the 4-momentum in Minkowski space. Traditionally $\Pi(q^2)$ is calculated for time-like momenta $q^2 > 0$ by using the dispersion relation and the optical theorem. The dispersion relation allows for an analytic continuation from the real part of $\Pi(q^2)$ to its imaginary part

$$\Pi(q^2) - \Pi(0) = \frac{q^2}{\pi} \int_0^\infty ds \frac{\text{Im}\Pi(s)}{s(s - q^2 - i\varepsilon)}, \quad (6.8)$$

and the optical theorem relates the imaginary part of $\Pi(s)$ to the experimental data of the total cross section of e^+e^- annihilation

$$\text{Im}\Pi(s) = \frac{\alpha}{3} R(s), \quad (6.9)$$

where $R(s)$ is the cross section ratio defined in Eq. (1.1). Using Eq. (6.8) together with Eq. (6.9), the leading order hadronic correction a_μ^{had} can be directly calculated in terms of $R(s)$ via the following relation (see Ref. [118] for a review)

$$a_\mu^{\text{had}} = \frac{\alpha^2}{3\pi^2} \int_{4m_\pi^2}^\infty \frac{ds}{s} K\left(\frac{s}{m_\mu^2}\right) R(s), \quad (6.10)$$

where

$$K\left(\frac{s}{m_\mu^2}\right) = \int_0^1 dx \frac{x^2(1-x)}{x^2 + (1-x)s/m_\mu^2}. \quad (6.11)$$

Using recent high-precision $e^+e^- \rightarrow \pi^+\pi^-$ cross section data from the BABAR experiment [119], Ref. [16] obtains for the e^+e^- -based evaluation of

$$a_\mu^{\text{had}} = (695.5 \pm 4.1) \times 10^{-10}, \quad e^+e^- \text{-based}. \quad (6.12)$$

Besides the e^+e^- -data, the experimental data of hadronic τ -decays can also be used to calculate a_μ^{had} . Including the recent $\tau^- \rightarrow \pi^- \pi^0 \nu_\tau$ data from the Belle experiment [120], Ref. [17] reports the following result for a_μ^{had}

$$a_\mu^{\text{had}} = (705.3 \pm 4.5) \times 10^{-10}, \quad \tau\text{-based}. \quad (6.13)$$

Hence, a 1.6σ discrepancy between the e^+e^- - and the τ -based determinations of a_μ^{had} is found. In both cases, the error of a_μ^{had} alone represents 60% of the theoretical error. It is exactly here where lattice calculations are desirable to provide a theoretical determination of a_μ^{had} from first principles.

6.2.2 Lattice determination in Euclidean space

On the lattice, the vacuum polarization function $\Pi(Q^2)$ is calculated in Euclidean space with $Q^2 = -q^2 > 0$ (space-like momentum) via the relation

$$\Pi_{\mu\nu}(Q) = (Q_\mu Q_\nu - Q^2 \delta_{\mu\nu}) \Pi(Q^2). \quad (6.14)$$

It is proved in Ref. [18] that $\Pi(Q^2)$, calculated on the lattice and in Euclidean space, can be directly inserted into the one-loop diagram for a_μ^{had} without analytically continuing $\Pi(Q^2)$ back to Minkowski space, or requiring its value in the region $Q^2 < 0$ which would not be accessible to lattice calculations. The hadronic contribution a_μ^{had} can then be calculated from the vacuum polarization function at space-like momenta through the relation [18]

$$a_\mu^{\text{had}} = \alpha^2 \int_0^\infty \frac{dQ^2}{Q^2} F\left(\frac{Q^2}{m_\mu^2}\right) (\Pi(Q^2) - \Pi(0)), \quad (6.15)$$

where the kernel F is given by

$$F\left(\frac{Q^2}{m_\mu^2}\right) = \frac{64}{(Q^2/m_\mu^2)^2 \left(1 + \sqrt{1 + 4m_\mu^2/Q^2}\right)^4 \sqrt{1 + 4m_\mu^2/Q^2}}. \quad (6.16)$$

Here we remark that the integrand in Eq. (6.15) is peaked at small momenta and the kernel, $F(\frac{Q^2}{m_\mu^2})$, attains a maximal value at $Q^2 = (\sqrt{5} - 2)m_\mu^2 \approx 0.003 \text{ GeV}^2$ with a muon mass of $m_\mu = 105.7 \text{ MeV}$. (The inverse power of Q^2 in Eq. (6.15) is canceled by the subtraction $\Pi(Q^2) - \Pi(0)$, which is proportional to Q^2 .)

The smallest momentum accessible in our finite volume calculation is $Q^2 = (2\pi/T)^2 \approx 0.06 \text{ GeV}^2$. Therefore a reliable low Q^2 extrapolation is essential to calculate $\Pi(Q^2)$. In particular the ultra-violet subtraction at $Q^2 = 0$, required to renormalize $\Pi(Q^2)$, induces larger uncertainties than naively expected.

6.3 Determination of $\Pi(Q^2)$

6.3.1 Conserved current in the continuum

In the above section, the relation between the leading order hadronic contribution to the muon anomalous magnetic moment a_μ^{had} and the hadronic vacuum polarization function $\Pi(Q^2)$ in Euclidean space is established via Eq. (6.15). We will now discuss how to compute $\Pi(Q^2)$ itself. In the continuum limit, the vacuum polarization tensor $\Pi_{\mu\nu}(Q)$ is defined as

$$\Pi_{\mu\nu}(Q) = i \int d^4x e^{iQ \cdot (x-y)} \langle 0 | T J_\mu(x) J_\nu(y) | 0 \rangle \quad (6.17)$$

where J_μ is the hadronic electromagnetic current

$$\begin{aligned} J_\mu(x) &= \sum_f e_f \bar{\psi}_f(x) \gamma_\mu \psi_f(x) \\ &= \frac{2}{3} \bar{u}(x) \gamma_\mu u(x) - \frac{1}{3} \bar{d}(x) \gamma_\mu d(x) - \frac{1}{3} \bar{s}(x) \gamma_\mu s(x) + \dots \\ &= \bar{\psi}(x) \gamma_\mu \tau \psi(x) - \frac{1}{3} \bar{s}(x) \gamma_\mu s(x) + \dots \end{aligned} \quad (6.18)$$

Here, τ is a matrix in the $N_f = 2$ flavor space

$$\tau = \begin{pmatrix} 2/3 & 0 \\ 0 & -1/3 \end{pmatrix} = \frac{1}{6} \mathbf{1} + \frac{1}{2} \tau^3. \quad (6.19)$$

In the continuum, the local vector current given in Eq. (6.18) is conserved, satisfying the Ward identity

$$\partial_\mu J_\mu(x) = 0 \quad \Rightarrow \quad Q_\mu \Pi(Q)_{\mu\nu} = 0. \quad (6.20)$$

Eq. (6.20) together with Lorentz symmetry indicates that $\Pi_{\mu\nu}(Q)$ is proportional to the projector $Q_\mu Q_\nu - Q^2 \delta_{\mu\nu}$. By eliminating the factor $Q_\mu Q_\nu - Q^2 \delta_{\mu\nu}$, one can hence extract the vacuum polarization function $\Pi(Q^2)$.

6.3.2 Conserved current on the lattice

On the lattice, due to discretization effects, the local vector current is not conserved any more. In this work, we will use twisted mass fermions. Its fermionic action \mathcal{S}_{tm} is given by

$$\mathcal{S}_{tm} = \sum_x \bar{\chi}(x) [D_W + m_0 + i\mu\gamma_5\tau_3] \chi(x) . \quad (6.21)$$

The *Noether theorem* tells us that there is a one-to-one correspondence between a given continuous transformation symmetry and a corresponding conservation law. Let us look at a vector flavor transformation under which the fermion fields behave according to

$$\delta_V \chi(x) = i\epsilon_V(x)\tau\chi(x) , \quad \delta_V \bar{\chi}(x) = -i\bar{\chi}(x)\tau\epsilon_V(x) . \quad (6.22)$$

We call such a transformation a symmetry if it leaves the action invariant

$$\delta_V \mathcal{S}_{tm} = 0 \Rightarrow \sum_x i\epsilon_V(x) \left(-\partial_\mu^* J_\mu^{tm}(x) + \bar{\chi}(x)[m_0, \tau]\chi(x) + \bar{\chi}(x)i\mu\gamma_5[\tau^3, \tau]\chi(x) \right) = 0 , \quad (6.23)$$

where ∂_μ^* is the backward lattice derivative given in Eq. (2.21) and the vector current $J_\mu^{tm}(x)$ is defined as

$$J_\mu^{tm}(x) = \frac{1}{2} \left(\bar{\chi}(x)\tau(\gamma_\mu - r)U_\mu(x)\chi(x + \hat{\mu}) + \bar{\chi}(x + \hat{\mu})\tau(\gamma_\mu + r)U_\mu^\dagger(x)\chi(x) \right) . \quad (6.24)$$

Since the flavor matrix τ defined in Eq. (6.19) commutes with both m_0 and τ^3 , the action invariance condition $\delta_V \mathcal{S}_{tm} = 0$ directly yields the Ward identity

$$\partial_\mu^* J_\mu^{tm}(x) = 0 . \quad (6.25)$$

In this way, we construct the conserved current (6.24) in the twisted basis for twisted mass fermions. Performing the axial transformation of Eq. (2.58), we can translate the conserved current to the physical basis. From the simple property

$$\tau\gamma_\mu = \exp(-i\omega\gamma_5\tau_3/2)\tau\gamma_\mu\exp(-i\omega\gamma_5\tau_3/2) , \quad (6.26)$$

we find that the conserved vector current in the physical basis retains the same form as for standard Wilson fermions.

In our calculations, we will use the conserved Noether current in the twisted basis (6.24) instead of the local current. This has the advantage that no renormalization factor is required and ensures that the Ward identity holds even for non-zero lattice spacing.

6.3.3 Ward identities

Eq. (6.25) is only one example of the Ward identities. A more general form of such Ward identities involving flavor currents and general local operators $\mathcal{O}(x_1, \dots, x_n)$ is derived as [121]

$$\langle \delta_V \mathcal{O}(x_1, \dots, x_n) \rangle - \langle \mathcal{O}(x_1, \dots, x_n) \delta_V \mathcal{S}_{tm} \rangle = 0. \quad (6.27)$$

When $\mathcal{O} = 1$, Eq. (6.27) takes the form of Eq. (6.25). In the case of $\mathcal{O} = J_\nu^{tm}(y)$, Eq. (6.27) yields

$$\sum_x -i\epsilon_V(x) \langle \partial_\mu^* J_\mu^{tm}(x) J_\nu^{tm}(y) \rangle = \langle \delta_V J_\nu^{tm}(y) \rangle = i(\epsilon_V(y) - \epsilon_V(y + \hat{\nu})) \langle J_\nu^{(2)}(y) \rangle, \quad (6.28)$$

or equivalently

$$\langle \partial_\mu^* J_\mu^{tm}(x) J_\nu^{tm}(y) \rangle = (\delta(x - y - \hat{\nu}) - \delta(x - y)) \langle J_\nu^{(2)}(y) \rangle \quad (6.29)$$

where the contact term $J_\nu^{(2)}(y)$ is defined by

$$J_\nu^{(2)}(y) = \frac{1}{2} \left(-\bar{\chi}(y) \tau(\gamma_\nu - r) U_\mu(y) \chi(y + \hat{\nu}) + \bar{\chi}(y + \hat{\nu}) \tau(\gamma_\nu + r) U_\nu^\dagger(y) \chi(y) \right). \quad (6.30)$$

Eq. (6.29) is the Ward identity for the vector-vector (actually conserved vector-conserved vector) two-point function.

Performing a Fourier transformation, the conserved vector current in momentum space can be expressed through

$$J_\mu^{tm}(\hat{Q}) = \sum_x e^{iQ \cdot (x + \hat{\mu}/2)} J_\mu^{tm}(x), \quad \hat{Q}_\mu = 2 \sin \left(\frac{Q_\mu}{2} \right). \quad (6.31)$$

Correspondingly, we construct the vacuum polarization tensor $\Pi_{\mu\nu}^{(1)}(\hat{Q})$ as

$$\Pi_{\mu\nu}^{(1)}(\hat{Q}) = \frac{1}{V} \sum_{x,y} e^{iQ \cdot (x + \hat{\mu}/2 - y - \hat{\nu}/2)} \langle J_\mu^{tm}(x) J_\nu^{tm}(y) \rangle \quad (6.32)$$

with $V = 1/(L^3 T)$. The Ward identity (6.29) translates into momentum space as

$$-i\hat{Q}_\mu \Pi_{\mu\nu}^{(1)}(\hat{Q}) = \frac{1}{V} \sum_y i\hat{Q}_\nu \langle J_\nu^{(2)}(y) \rangle. \quad (6.33)$$

a (fm)	V/a^4	L (fm)	m_π (MeV)						$(m_\pi L)_{\min}$
0.079	$24^3 \times 48$	1.9		420		480	520	640	4.1
0.079	$32^3 \times 64$	2.5	290	330					3.7
0.063	$24^3 \times 48$	1.5				450			3.5
0.063	$32^3 \times 64$	2.0		320		450		520	3.3

Table 6.1: Parameters used in the calculation of the hadronic vacuum polarization function.

We are therefore led to define

$$\Pi_{\mu\nu}(\hat{Q}) = \Pi_{\mu\nu}^{(1)}(\hat{Q}) + \Pi_{\mu\nu}^{(2)}(\hat{Q}), \quad \Pi_{\mu\nu}^{(2)}(\hat{Q}) = \frac{1}{V} \sum_y \delta_{\mu\nu} \langle J_\nu^{(2)}(y) \rangle. \quad (6.34)$$

$\Pi_{\mu\nu}(\hat{Q})$ as given in Eq. (6.34) fulfills the relation $\hat{Q}_\mu \Pi_{\mu\nu}(\hat{Q}) = 0$ and allows us to extract the vacuum polarization function $\Pi(\hat{Q}^2)$ through the relation¹

$$\Pi_{\mu\nu}(\hat{Q}) = (\hat{Q}_\mu \hat{Q}_\nu - \hat{Q}^2 \delta_{\mu\nu}) \Pi(\hat{Q}^2). \quad (6.35)$$

6.4 Lattice setup

The details of the ensembles used in this work are given in Table 6.1. We perform the calculation at two lattice spacings $a = 0.079$ fm and $a = 0.063$ fm with the pion mass ranging from 640 MeV to 290 MeV. At the lattice spacing $a = 0.063$ fm and a pion mass $m_\pi = 450$ MeV, there are two ensembles with different lattice sizes L , which allows us to perform a study of finite volume effects. At $m_\pi = 520$ MeV and $L \approx 2.0$ fm, there are two ensembles with different lattice spacings, which allows us to perform a study of lattice artifacts. Thus, we are in a position to estimate the systematic uncertainties stemming from these two effects.

The calculation of $\Pi_{\mu\nu}(\hat{Q})$ here proceeds as has been done in the previous work [18, 96, 112]. Propagators from point sources at a single lattice site and the four forward neighbors are calculated and used to construct the vector current-vector current correlator in Eq. (6.32). Here we place the sources randomly in the 4-dimensional Euclidean space to

¹Lattice discretization effects break the Lorentz symmetry. As a result, besides the terms of $\hat{Q}^2 \delta_{\mu\nu}$ and $\hat{Q}_\mu \hat{Q}_\nu$, other terms like $a^2 \hat{Q}_\mu^2 \hat{Q}_\nu^2$ will also appear in $\Pi_{\mu\nu}(\hat{Q})$ and make its structure more complicated. In our calculation, we neglect such lattice artifacts which is justified a posteriori when we employ a second value of the lattice spacing to check our results.

reduce the autocorrelation between consecutive trajectories. For each point source, we perform twelve inversions due to the spin and color degree of freedom. The one exceptional aspect of the calculation with twisted mass fermions is that separate u and d quark inversions must be performed due to the modified γ_5 -hermiticity: $\gamma_5 D_u^\dagger \gamma_5 = D_d$. This can be seen from the expression

$$\gamma_\mu D_u^{-1}(x, y) \gamma_\nu D_u^{-1\dagger}(y, x) = \gamma_\mu D_u^{-1}(x, y) \gamma_\nu \gamma_5 D_d^{-1}(x, y) \gamma_5. \quad (6.36)$$

Note that we therefore perform $5 \times 12 \times 2 = 120$ inversions for each configuration, showing that the calculation of the vacuum polarization tensor is a computationally rather demanding task.

Twisted mass fermions break flavor symmetry. However, the γ_5 -hermiticity relates u and d quark loops and results in $\Pi_{\mu\nu}^d(x, y) = \Pi_{\mu\nu}^{u*}(x, y)$. This expression is true for each gauge field configuration. The consequence is that $\text{Re}[\Pi^d(\hat{Q}^2)] = \text{Re}[\Pi^u(\hat{Q}^2)]$. Hence by simply taking the real part of $\Pi(\hat{Q}^2)$, which is real in the continuum limit, we eliminate any explicit flavor breaking in the valence sector². Additionally, we expect the real part of $\Pi(\hat{Q}^2)$ (which is the physically relevant piece) to be accurate to $O(a^2)$, even if the (unphysical) imaginary part has $O(a)$ corrections.

6.5 Results

6.5.1 $\Pi(\hat{Q}^2)$: analysis of systematic effects

First we examine the finite size effects in $\Pi(\hat{Q}^2)$. We have calculated $\Pi(\hat{Q}^2)$ at two volumes, $L = 2.0$ fm and $L = 1.5$ fm keeping $m_\pi = 450$ MeV and $a = 0.063$ fm fixed. In Fig. 6.2 we show the results for $\Pi(\hat{Q}^2)$ for these two volumes. Since we are working at a fixed value of the the lattice spacing, we do not need to subtract $\Pi(\hat{Q}^2)$ at $\hat{Q}^2 = 0$ to cancel the ultra-violet divergence for the study of finite volume effects. From Fig. 6.2 it can be seen that within the statistical errors there are no significant finite volume effects for $\Pi(\hat{Q}^2)$ when we use data with $m_\pi L \lesssim 3.5$ as done here. As can be inferred from Table 6.1, among all our data sets, there is only one ensemble with $m_\pi L$ slightly smaller than 3.5. We therefore

²In the sea sector, the implicit flavor breaking remains because $m_\rho^\pm \neq m_\rho^0$.

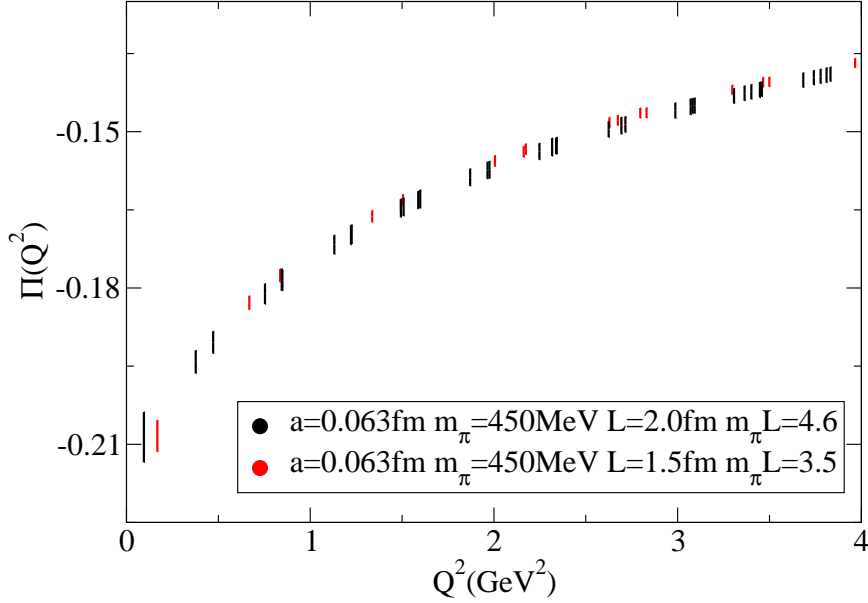


Figure 6.2: Volume dependence of $\Pi(\hat{Q}^2)$. This quantity requires an ultra-violet subtraction but is infra-red finite. Within the statistical errors there are no significant finite volume effects for $\Pi(\hat{Q}^2)$.

expect that most of our data are safe from such systematic effects. Below, by using different fitting models for the momentum dependence of $\Pi(\hat{Q}^2)$, we will investigate how finite volume effects may influence the results of a_μ^{had} where an additional extrapolation and subtraction procedure has to be applied.

Next we examine the lattice artifacts in $\Pi(\hat{Q}^2)$ which we have calculated at two lattice spacings, $a = 0.079$ fm and $a = 0.063$ fm. In both cases we have taken $m_\pi = 520$ MeV. The lattice sizes are only slightly different: one is $L = 1.9$ fm and the other 2.0 fm. Fig. 6.3 shows the unrenormalized results for $\Pi(\hat{Q}^2)$ demonstrating the ultra-violet divergence present without the subtraction. In Fig. 6.4 we subtract $\Pi(\hat{Q}_{\text{min}}^2)$ with \hat{Q}_{min}^2 taken at the lowest momentum \hat{Q}^2 available for the corresponding lattice spacing. This procedure avoids the extrapolation to $\hat{Q}^2 = 0$. Since the volumes are almost the same for both lattice spacings, the values of \hat{Q}_{min}^2 are very similar which allows for a meaningful comparison. As shown in Fig. 6.4, in the range $0.1 \text{ GeV}^2 < \hat{Q}^2 < 4 \text{ GeV}^2$ we see no significant lattice artifacts in

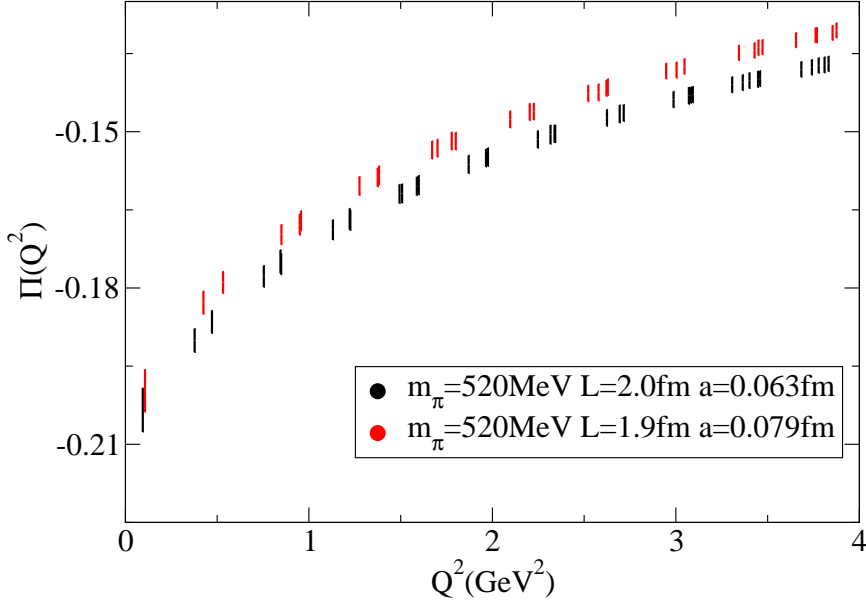


Figure 6.3: Lattice spacing dependence of $\Pi(\hat{Q}^2)$ without the subtraction of $\Pi(\hat{0}^2)$ needed to regulate the vacuum polarization function.

$$\Pi(\hat{Q}^2) - \Pi(\hat{Q}_{\min}^2).$$

As a next step, we now consider the m_π dependence. Figs. 6.5 and 6.6 show the pion mass dependence of $\Pi(\hat{Q}^2)$ with six values of m_π for $a = 0.079$ fm. Note that at the two lowest pion masses, the lattice size is larger, thus the \hat{Q}^2 values are different. Figs. 6.7 and 6.8 show $\Pi(\hat{Q}^2)$ with three values of m_π for $a = 0.063$ fm. Figs. 6.5 and 6.7 demonstrate that there is no significant quark mass dependence for large \hat{Q}^2 , as expected from perturbation theory [122,123]. Even when focussing on small values of \hat{Q}^2 , as shown in Fig. 6.6 and 6.8, we can only observe a systematic, but not statistically significant, shift with quark mass from 640 MeV to 270 MeV.

6.5.2 a_μ^{had} : results from various data modeling

To determine the contribution of the hadronic vacuum polarization function to a_μ^{had} , which is our final goal, we must parameterize and fit the \hat{Q}^2 dependence of $\Pi(\hat{Q}^2)$ and extrapolate to $\hat{Q}^2 = 0$ in order to perform the integral in Eq. (6.15). Unfortunately, there is no closed

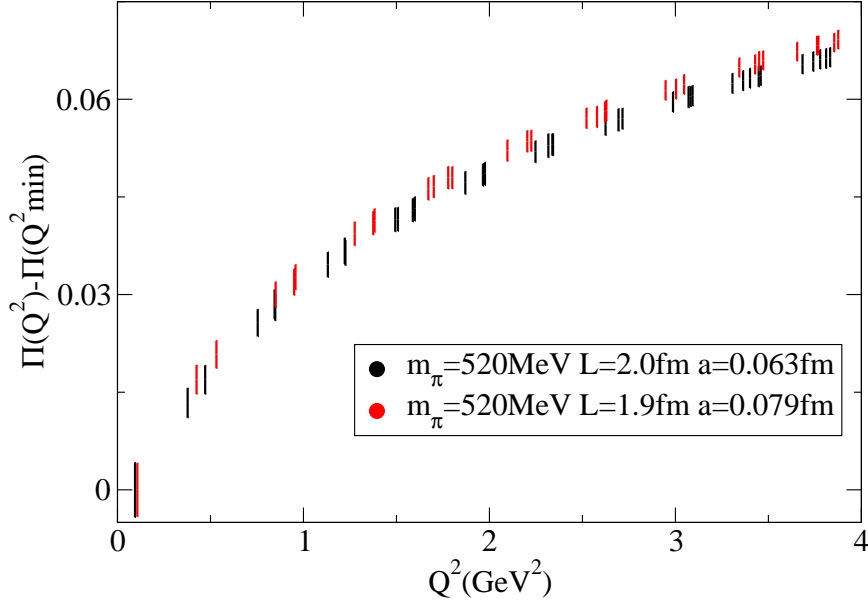


Figure 6.4: Lattice spacing dependence of $\Pi(\hat{Q}^2) - \Pi(\hat{Q}_{\min}^2)$. The results have been renormalized at the lowest value of $\hat{Q}^2 \approx 0.1 \text{ GeV}^2$ at each lattice spacing to illustrate the effect of the subtraction. In the range $0.1 \text{ GeV}^2 < \hat{Q}^2 < 4 \text{ GeV}^2$, there is no explicit lattice spacing dependence.

form available to describe the \hat{Q}^2 dependence of $\Pi(\hat{Q}^2)$. However, the analyticity property of $\Pi(Q)$ allows us to perform a fit using simple polynomials. In Figs. 6.9 and 6.10 we show fits to polynomials in \hat{Q}^2 with 4 terms (cubic) and 5 terms (quartic). The lattice results and corresponding curves are shifted vertically to illustrate the quality of the fits and the nature of the extrapolation to $\hat{Q}^2 = 0$. For all ensembles the cubic fit seems fully sufficient to describe the lattice results and hence from these fit results we are able to calculate a_μ^{had} using Eq. (6.15). Fig. 6.11 shows the resulting values for all the ten ensembles using the cubic fit ansatz. We have also examined the volume and the lattice spacing dependence of our results and find no explicit finite size effects and lattice artifacts in accordance with the discussion on $\Pi(\hat{Q}^2)$ above, see Figs. 6.2 and 6.4. Additionally, there is no clear quark mass dependence visible in Fig. 6.11. We perform a linear fit in the square of the pion mass to extrapolate our results to the physical point where we find $a_\mu^{\text{had}} = 383(44) \times 10^{-10}$. As

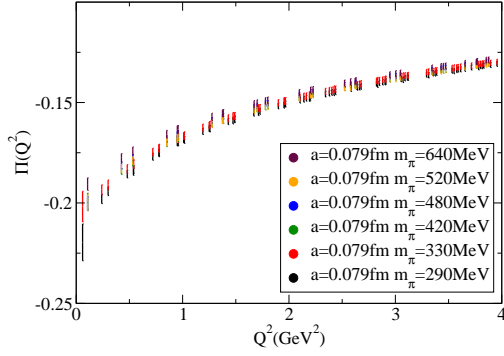


Figure 6.5: Quark mass dependence of $\Pi(\hat{Q}^2)$ at large \hat{Q}^2 using $a = 0.079$ fm. There is no noticeable quark mass dependence at large \hat{Q}^2 , consistent with pQCD expectations.

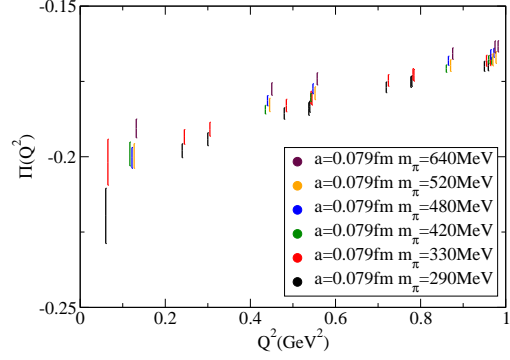


Figure 6.6: Quark mass dependence of $\Pi(\hat{Q}^2)$ at low \hat{Q}^2 using $a = 0.079$ fm. There is a systematic, but not statistically significant, shift with quark mass from $m_\pi = 640$ MeV to 270 MeV.

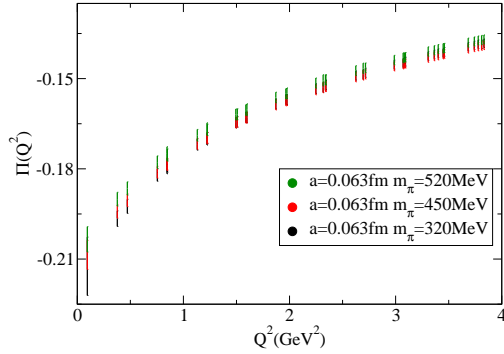


Figure 6.7: Quark mass dependence of $\Pi(\hat{Q}^2)$ at large \hat{Q}^2 using $a = 0.063$ fm. There is no noticeable quark mass dependence at large \hat{Q}^2 , consistent with pQCD expectations.

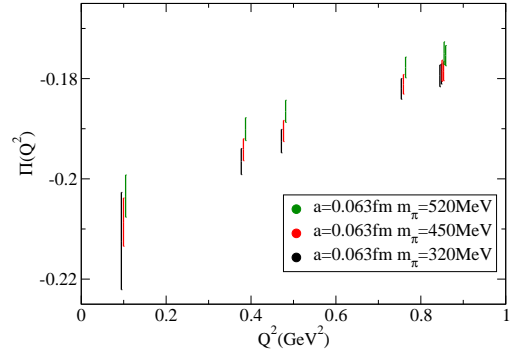


Figure 6.8: Quark mass dependence of $\Pi(\hat{Q}^2)$ at low \hat{Q}^2 using $a = 0.063$ fm. There is a systematic, but not statistically significant, shift with quark mass from $m_\pi = 640$ MeV to 270 MeV.

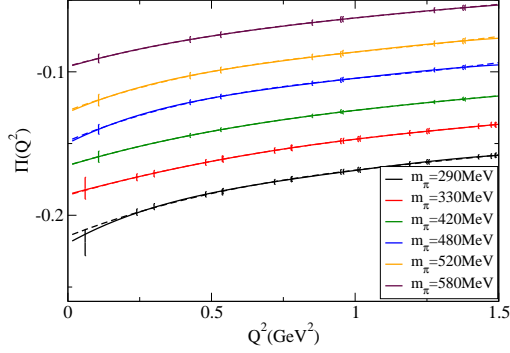


Figure 6.9: The low \hat{Q}^2 extrapolation of $\Pi(\hat{Q}^2)$ for $a = 0.079$ fm using polynomial fits. Each $\Pi(\hat{Q}^2)$ has been fit to cubic (dashed line) and quartic (solid line) functions of \hat{Q}^2 , showing agreement for all data sets.

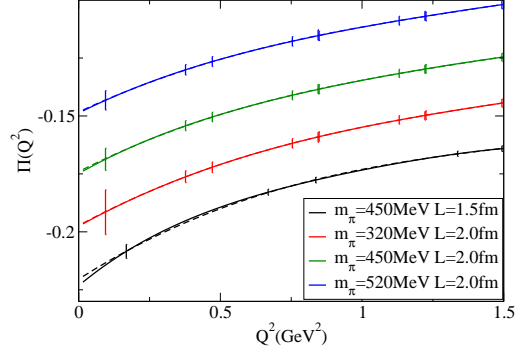


Figure 6.10: The low \hat{Q}^2 extrapolation of $\Pi(\hat{Q}^2)$ for $a = 0.063$ fm using polynomial fits. Each $\Pi(\hat{Q}^2)$ has been fit to cubic (dashed line) and quartic (solid line) functions of \hat{Q}^2 , showing agreement for all data sets.

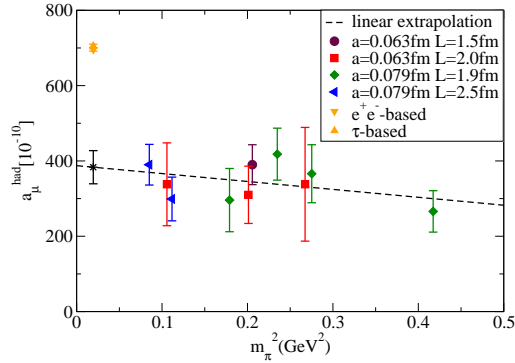


Figure 6.11: The results for a_μ^{had} using a cubic fit. Within the statistical errors, we do not find explicit finite size effects and lattice artifacts. Unfortunately, with the large errors, we do not find a clear quark mass dependence either.

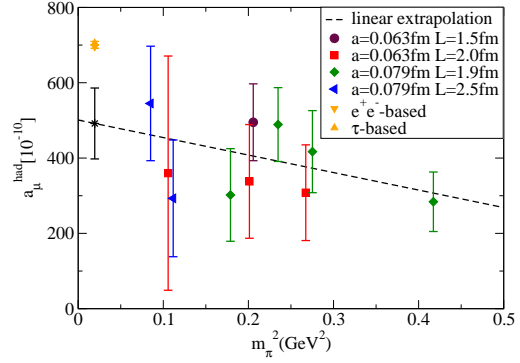


Figure 6.12: The results for a_μ^{had} using a quartic fit. As we increase the order of the polynomial from the cubic fit to the quartic fit the results become much noisier and a systematic, but not statistically significant, rise in a_μ^{had} is found.

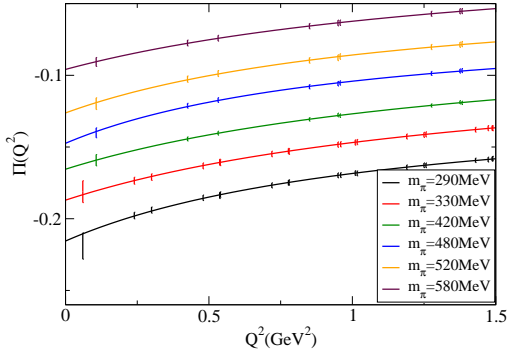


Figure 6.13: The low \hat{Q}^2 extrapolation of $\Pi(\hat{Q}^2)$ for $a = 0.079$ fm using a dipole fit. Each $\Pi(\hat{Q}^2)$ has been fit to the dipole function (6.40) of \hat{Q}^2 , showing agreement for all data sets.

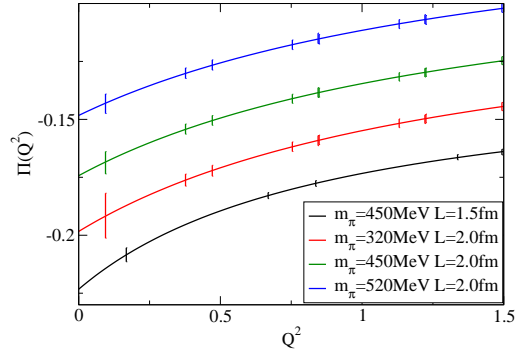


Figure 6.14: The low \hat{Q}^2 extrapolation of $\Pi(\hat{Q}^2)$ for $a = 0.063$ fm using a dipole fit. Each $\Pi(\hat{Q}^2)$ has been fit to the dipole function (6.40) of \hat{Q}^2 , showing agreement for all data sets.

can be seen in Fig. 6.11, our result indicated by the star symbol is lying rather low relative to the e^+e^- - or τ -based determination of a_μ^{had} . We will come back to this point later. In Fig. 6.12 we show the results for all the ten ensembles using the quartic fit ansatz. We note a systematic, but not statistically significant, rise in a_μ^{had} as we increase the order of the polynomial from the cubic fit to the quartic fit. At the physical point we find the resulting value of $a_\mu^{\text{had}} = 492(94) \times 10^{-10}$.

Phenomenologically, as indicated by Eq. (6.8) and (6.9), the imaginary part of the vacuum polarization function is related to intermediate hadronic states such as the low lying vector mesons $\rho, \omega, \phi, \dots$, and the hadronic multi-particle scattering states $\pi\pi, 3\pi, 4\pi, \dots$, which in the dispersion relation correspond to the states produced in e^+e^- -annihilation via a virtual photon. In Eq. (6.10), the kernel $K(s/m_\mu^2)$ gives very high weight to the low energy regime, in particular to the lowest vector bosons ρ, ω and ϕ . The contributions from the three lightest vector mesons to a_μ^{had} read [124]

$$a_\mu^\rho = 501.37(3.49) \times 10^{-10}, \quad a_\mu^\omega = 36.96(1.09) \times 10^{-10}, \quad a_\mu^\phi = 34.42(0.93) \times 10^{-10}, \quad (6.37)$$

present more than 80% of the total hadronic vacuum polarization contributions to a_μ^{had} . This vector meson dominance is also expected from χ PT [125], indicating that the vacuum

polarization function at tree level is given by

$$\Pi_V^{\text{tree}}(Q^2) = -\frac{f_V}{12\pi} \left[\frac{3}{Q^2 + m_\rho^2} + \frac{1}{Q^2 + m_\omega^2} \right] \quad (6.38)$$

where f_V is the tree level vector decay constant. Notice that at tree level, the masses of both the ρ and ω mesons are the same, $m_\rho = m_\omega = m_V$. Eq. (6.38) then becomes

$$\Pi_V^{\text{tree}}(Q^2) = -\frac{f_V}{3\pi} \frac{1}{Q^2 + m_V^2}. \quad (6.39)$$

If we were to measure the decay constant f_V as well as the vector masses m_V from lattice calculations, then Eq. (6.39) would have no free parameters. Here, however, we set both f_V and m_V as free fitting parameters. Considering the ultra-violet divergent property of $\Pi(\hat{Q}^2)$, we need to employ a third fit parameter c_0 , leading to the fit function

$$\Pi(Q^2) = -\frac{f_V}{3\pi} \frac{1}{Q^2 + m_V^2} + c_0, \quad (6.40)$$

which we refer to as the dipole fit. In Figs. 6.13 and 6.14 we show the plots of the dipole fit for the two lattice spacings we have used. The lattice results and the corresponding fit curves are shifted vertically to illustrate the quality of the fits and the extrapolation to $\hat{Q}^2 = 0$. For all ensembles the dipole fit seems to describe the lattice results well. Using this fit, we calculate a_μ^{had} in the same way as discussed above for the polynomial fits. Fig. 6.15 shows the resulting values for a_μ^{had} for all the ten ensembles using the dipole fit. Examining the L and a dependence of our results we again find that within our large statistical errors there are still no lattice artifacts and finite size effects visible in our calculation. As in the case of the cubic fit, no clear quark mass dependence is found here. Using the linear extrapolation we find for $a_\mu^{\text{had}} = 430(48)$ at the physical point. Our result lies low compared to the e^+e^- - or τ -based determination of a_μ^{had} , indicated by the triangle up and down symbols in Fig. 6.15. Choosing the dipole fit value as the final result and taking the range of a_μ^{had} spanned by various fitting models as a systematic error, we find for $a_\mu^{\text{had}} = 430(73)$.

The results of our analysis for a_μ^{had} discussed above show that our data points are lower than the e^+e^- - or τ -based value. One element of this discrepancy is due to the fact that our lattice results for m_ρ lie high relative to the physical value as shown by Fig. 5.11 (see Chapter 5 for details). There, the extrapolation of the ρ mass using effective field

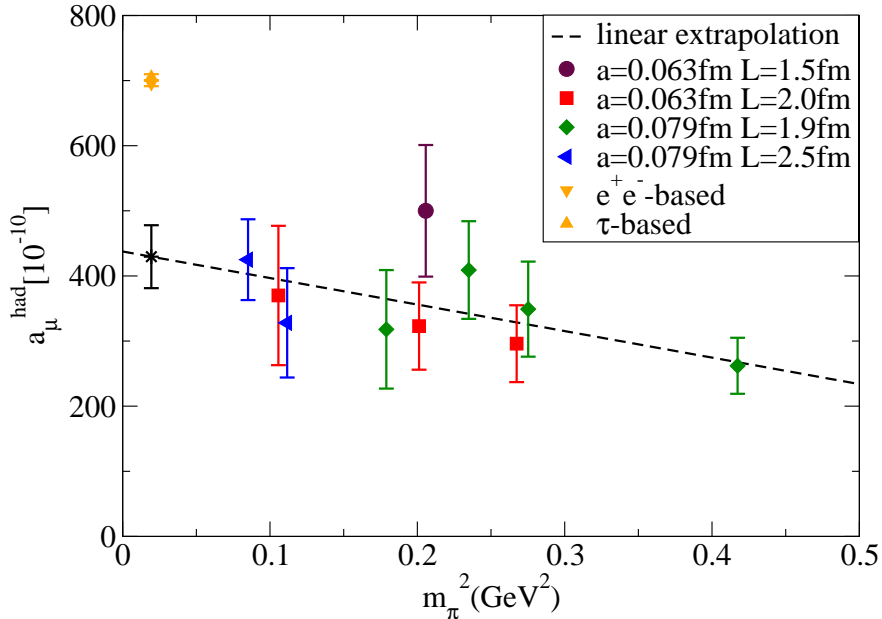


Figure 6.15: The results for a_μ^{had} using a dipole fit. Within the rather large statistical errors, we do not find explicit lattice artifacts and finite size effects in the determination of a_μ^{had} using the dipole fit. Unfortunately, there is no clear quark mass dependence either.

theory [111] shows that even if the ρ mass is determined down to $m_\pi \approx 300$ MeV, its quark mass dependence may not satisfactorily be described by effective field theory. Since the ρ meson makes the largest contribution to $\Pi(Q^2)$ and hence to a_μ^{had} , it is hence important to explore the behavior of $\Pi(Q^2)$ and a_μ^{had} at even lower pion masses.

In principle, our calculation could be improved by using larger lattice sizes L or alternative techniques such as twisted boundary conditions with twist angle θ . This could help to explore $\Pi(Q^2)$ in a smaller momentum region $\sim Q^2 = (\theta/L)^2$. In addition, alternative models could be used to fit the data. One choice would be to set one parameter f_V free but keep the other one m_V fixed, as it is done in Ref. [96]. By fitting only two free parameters, it can be expected that the statistical errors of the fitting results are smaller. A second choice is that we can plug the values of f_V and m_V calculated from lattice simulations into

$\Pi_V^{\text{tree}}(Q^2)$ and fit our data points with the function

$$\Pi(Q^2) = \Pi_V^{\text{tree}}(Q^2) + \sum_n c_n (Q^2)^n . \quad (6.41)$$

This method fixes the vector meson contribution to $\Pi(Q^2)$ and treats the contributions from other states such as J/Ψ and hadronic multi-particles scattering states in a simple phenomenological way as polynomials in Q^2 .

Besides these possible improvements, in principle also the rho decay effects should be taken into consideration when modeling the Q^2 dependence of $\Pi(Q^2)$ and extracting a_μ^{had} , since such effects become much stronger as the pion mass approaches the physical point. Another systematic effects, which remain undetermined, are the contributions to $\Pi(Q^2)$ from the disconnected diagrams. Such contributions, when summed over u , d and s quarks, cancel in the SU(3) flavor limit, and they are suppressed according to Zweig's rule [126,127]. Nevertheless, to make a precise determination of $\Pi(Q^2)$, we should estimate the size of this systematic error. However, all these new approaches which require partly new and demanding simulations go beyond the scope of this thesis and have to be left for future investigations.

CHAPTER VII

CONCLUSION AND OUTLOOK

In this concluding section we summarize the work presented in this thesis and give an outlook for possible extensions. The general theme of the thesis has been to obtain non-perturbative, ab-initio results from Lattice QCD computations that are of direct relevance for scattering experiments in high energy physics. In particular, we have discussed in Chapter 4 the $I = 2$ pion scattering length, have determined in Chapter 5 the ρ resonance parameters and in Chapter 6 the leading order hadronic contribution to the anomalous magnetic moment of the muon a_μ^{had} .

In more detail, in Chapter 4, we have calculated the S-wave pion-pion scattering length in the isospin $I = 2$ channel using the two-flavor maximally twisted mass Lattice QCD configurations from ETMC. The pion masses ranged from 520 MeV to 290 MeV and the lattice spacing was $a = 0.079$ fm. A second lattice spacing of $a = 0.063$ fm was used to demonstrate the absence of large lattice artifacts. Although this is only a check at a single value of a lattice spacing, when combined with the fact that the calculation is accurate to $O(a^2)$ due to the properties of maximally twisted mass fermions, it suggests that the lattice spacing dependence is mild.

Furthermore, from the χ PT side, discretization errors vanish from the $I = 2$, $I_3 = \pm 2$ channel at NLO, as shown by twisted mass χ PT. This allowed us to extrapolate our results for the scattering length to the physical limit, where the pion mass takes its experimentally measured value, using continuum χ PT at NLO. We investigated various systematic effects, such as π^0 contamination arising from the explicit isospin breaking of twisted mass fermions for $a \neq 0$, finite size effects and lattice artifacts. This led us to our final result for the scattering length at the physical point $m_\pi a_{\pi\pi}^{I=2} = -0.04385(28)(38)$ and for the low energy constant $l_{\pi\pi}^{I=2}(\mu = f_{\pi,\text{phy}}) = 4.65(0.85)(1.07)$. Here the first error is purely statistical while the second one is the systematic uncertainty. These results are in good agreement with the

previous lattice calculation from NPLQCD, the experimental determinations from E865 at BNL and from NA48/2 at CERN and the CGL analysis using various theoretical and experimental inputs (see Eqs. (4.3–4.8) for details). It is worth to mention that the lattice results are more accurate than the experimental measurements.

The successful determination of the pion-pion scattering length performed here, lays the basis for further lattice calculations. For example, we could study the momentum dependence of the pion-pion scattering phase, which is directly related to the energy dependence of the scattering cross section. In addition, the extraction of the derivative of the scattering phase with respect to the momentum can help to determine the K to $\pi\pi$ decay amplitude, using the Lellouch-Lüscher method [128]. Clearly, the techniques employed in this thesis can also be used to study more general two-particle scattering phenomena such as other meson-meson or meson-baryon and baryon-baryon scattering processes.

In Chapter 5, we have calculated the P-wave pion-pion scattering phase in the $I = 1$ channel. We have performed the calculations at pion masses ranging from 480 MeV to 290 MeV and at a lattice spacing of $a = 0.079$ fm. At all the pion masses, the physical kinematics for the ρ -meson decay, $m_\pi/m_\rho < 0.5$, is satisfied. A second lattice spacing of $a = 0.067$ fm has been used to examine the lattice artifacts. Within the statistical errors, we do not find any lattice artifacts. Compared to previous calculations by other lattice collaborations, we used a novel method by employing three Lorentz frames simultaneously. This allowed us to map out the energy region of the resonance rather precisely. Making use of Lüscher's finite size methods, we evaluated the scattering phase at six energy levels. In this way, we could fit the scattering phase with the effective range formula and find the results for the ρ -resonance mass m_ρ , the decay width Γ_ρ and the effective coupling $g_{\rho\pi\pi}$. Taking the high correlation between m_ρ and Γ_ρ into account, we have performed an extrapolation to the physical point of the combined parameter $Z = (m_\rho - i\Gamma_\rho/2)^2$ using fits guided by χ PT to $O(M_\pi^2)$ and $O(M_\pi^3)$. However, including the higher order terms significantly reduces the accuracy of the extrapolation, especially in the low pion mass region. We found that χ PT might not be fully adequate to describe the quark mass dependence of the ρ -meson mass and its decay width, even with pion masses as small as $m_\pi \sim 300$ MeV.

As the main result of this investigation, we found for the ρ -meson mass $m_\rho = 900(76)$ MeV and for the decay width $\Gamma_\rho = 178(32)$ MeV. When these numbers are compared to the corresponding experimentally measured quantities, it is clear that the lattice computations cannot yet match the experimental accuracy. Nevertheless, our work shows that the finite size method can in principle be used to determine resonance parameters from Lattice QCD calculations. Since most of the hadrons observed in nature are in fact resonances, this work demonstrates the practical possibility to treat these particles in a conceptually clean way on the lattice. Thus we consider our work concerning the ρ -resonance as a proof of principle that resonances can be studied in lattice calculations. An obvious extension of this work is to probe the pion-pion scattering in the $I = 0$ channel or the pion-nucleon scattering in the $I = 3/2$ channel, where the σ and Δ resonances appear. Since in these channels the experimental accuracy is not so high, the lattice may provide more precise results.

Moreover, the phenomenon of particle decay is a truly dynamical effect and the fact that we indeed have observed the ρ -meson as a resonance is a striking example of dynamical quark effects. Hence, the extraction of resonance parameters from lattice calculations can significantly contribute to our understanding of the dynamical aspects of hadron interactions.

Finally, let us summarize our lattice investigation of the muon anomalous magnetic moment, a_μ . The current high precision determinations of a_μ , both from experiment and theory, indicate a small discrepancy between nature and the Standard Model. The largest source of uncertainty in the Standard Model calculation of a_μ is the leading order hadronic contribution a_μ^{had} . In Chapter 6 we have presented a full QCD calculation of the vacuum polarization function and, in particular, of precisely this hadronic contribution a_μ^{had} . We have performed calculations with dynamical maximally twisted mass fermions with pion masses ranging from 640 MeV to 290 MeV. We had examined both finite size effects and lattice artifacts in our calculations. This is a first effort to begin to calculate a_μ^{had} while controlling the major sources of systematic error. Using both polynomial and dipole functions to model $\Pi(Q^2)$ and then determine a_μ^{had} , we do not find any obvious quark mass dependence, at least within our large statistical errors. We find that the resulting values of

a_μ^{had} obtained from the lattice lie too low relative to the e^+e^- - or τ -based value. One likely reason for this is the fact that the calculated ρ masses lie high relative to the physical value.

It would be very useful to have a more accurate determination of a_μ^{had} from Lattice QCD. There are several directions one could think of to improve the calculations. One possibility is to employ more sophisticated models to reduce the statistical error by eliminating some fit parameters. Also, larger lattice volumes should be used not only for reducing the finite volume effects, but also for exploring the lower Q^2 region. Some techniques like twisted boundary conditions may also be helpful to reach smaller Q^2 values. Most importantly, however, is the necessity to study both, $\Pi(Q^2)$ and a_μ^{had} , at lower pion masses than the ones employed here of $m_\pi \approx 300$ MeV. This would allow for a clean extrapolation to the physical pion mass. A controlled and accurate numerical calculation of $\Pi(Q^2)$ would not only lead to a precise value of a_μ^{had} , but would also help to compute the Adler function and to determine the strong coupling constant α_s .

To summarize, in this thesis we have demonstrated that a combination of lattice calculations with finite size methods and analytical approaches can provide –in some cases very accurate– physical quantities that are directly relevant to scattering experiments. While there are still open issues, such as the accurate extrapolation to the physical point, it is clear that Lattice QCD has reached a level of accuracy such that a direct interaction with phenomenology and experiment can begin to take place. We believe that the results obtained in this thesis provide an example of just such a fruitful interaction.

REFERENCES

- [1] NPLQCD S. R. Beane, P. F. Bedaque, K. Orginos, and M. J. Savage, “I = 2 pi pi scattering from fully-dynamical mixed-action lattice QCD,” *Phys. Rev.* **D73**, 054503 (2006) hep-lat/0506013.
- [2] S. R. Beane *et al.*, “Precise Determination of the I=2 pipi Scattering Length from Mixed-Action Lattice QCD,” *Phys. Rev.* **D77**, 014505 (2008) 0706.3026.
- [3] CP-PACS T. Yamazaki *et al.*, “I = 2 pi pi scattering phase shift with two flavors of O(a) improved dynamical quarks,” *Phys. Rev.* **D70**, 074513 (2004) hep-lat/0402025.
- [4] B. Bloch-Devauux, “Precision Measurement of pp Scattering Lengths in Ke4 Decays by NA48/2,” *PoS KAON09*, 033 (2009).
- [5] D. J. Gross and F. Wilczek, “ULTRAVIOLET BEHAVIOR OF NON-ABELIAN GAUGE THEORIES,” *Phys. Rev. Lett.* **30**, 1343 (1973).
- [6] S. Weinberg, “Nonabelian Gauge Theories of the Strong Interactions,” *Phys. Rev. Lett.* **31**, 494 (1973).
- [7] H. Fritzsch, M. Gell-Mann, and H. Leutwyler, “Advantages of the Color Octet Gluon Picture,” *Phys. Lett.* **B47**, 365 (1973).
- [8] F. Jegerlehner, “Precision measurements of sigma(hadronic) for alpha(eff)(E) at ILC energies and (g-2)(mu),” *Nucl. Phys. Proc. Suppl.* **162**, 22 (2006) hep-ph/0608329.
- [9] S. L. Adler, “Some Simple Vacuum Polarization Phenomenology: e+ e- → Hadrons: The mu - Mesic Atom x-Ray Discrepancy and (g-2) of the Muon,” *Phys. Rev.* **D10**, 3714 (1974).
- [10] A. De Rujula and H. Georgi, “Counting Quarks in e+ e- Annihilation,” *Phys. Rev.* **D13**, 1296 (1976).

- [11] S. Eidelman, F. Jegerlehner, A. L. Kataev, and O. Veretin, “Testing non-perturbative strong interaction effects via the Adler function,” *Phys. Lett.* **B454**, 369 (1999) hep-ph/9812521.
- [12] D. J. Gross and F. Wilczek, “Asymptotically Free Gauge Theories. 1,” *Phys. Rev.* **D8**, 3633 (1973).
- [13] H. D. Politzer, “RELIABLE PERTURBATIVE RESULTS FOR STRONG INTERACTIONS?,” *Phys. Rev. Lett.* **30**, 1346 (1973).
- [14] H. D. Politzer, “Asymptotic Freedom: An Approach to Strong Interactions,” *Phys. Rept.* **14**, 129 (1974).
- [15] Muon G-2 G. W. Bennett *et al.*, “Final report of the muon E821 anomalous magnetic moment measurement at BNL,” *Phys. Rev.* **D73**, 072003 (2006) hep-ex/0602035.
- [16] M. Davier, A. Hoecker, B. Malaescu, C. Z. Yuan, and Z. Zhang, “Reevaluation of the hadronic contribution to the muon magnetic anomaly using new $e^+e^- \rightarrow \pi^+\pi^-$ cross section data from BABAR,” *Eur. Phys. J.* **C66**, 1 (2010) 0908.4300.
- [17] M. Davier *et al.*, “The Discrepancy Between tau and e^+e^- Spectral Functions Revisited and the Consequences for the Muon Magnetic Anomaly,” *Eur. Phys. J.* **C66**, 127 (2010) 0906.5443.
- [18] T. Blum, “Lattice calculation of the lowest order hadronic contribution to the muon anomalous magnetic moment. ((U)),” *Phys. Rev. Lett.* **91**, 052001 (2003) hep-lat/0212018.
- [19] M. N. Achasov, “CMD-2 and SND results on the rho, omega and Phi,” *Nucl. Phys. Proc. Suppl.* **162**, 114 (2006) hep-ex/0604051.
- [20] Particle Data Group C. Amsler *et al.*, “Review of particle physics,” *Phys. Lett.* **B667**, 1 (2008).
- [21] M. Luscher, “Volume Dependence of the Energy Spectrum in Massive Quantum Field Theories. 1. Stable Particle States,” *Commun. Math. Phys.* **104**, 177 (1986).

- [22] M. Luscher, “Volume Dependence of the Energy Spectrum in Massive Quantum Field Theories. 2. Scattering States,” *Commun. Math. Phys.* **105**, 153 (1986).
- [23] M. Luscher and U. Wolff, “HOW TO CALCULATE THE ELASTIC SCATTERING MATRIX IN TWO- DIMENSIONAL QUANTUM FIELD THEORIES BY NUMERICAL SIMULATION,” *Nucl. Phys.* **B339**, 222 (1990).
- [24] M. Luscher, “Two particle states on a torus and their relation to the scattering matrix,” *Nucl. Phys.* **B354**, 531 (1991).
- [25] M. Luscher, “Signatures of unstable particles in finite volume,” *Nucl. Phys.* **B364**, 237 (1991).
- [26] J. Gasser and H. Leutwyler, “Chiral Perturbation Theory to One Loop,” *Ann. Phys.* **158**, 142 (1984).
- [27] J. Gasser and H. Leutwyler, “Chiral Perturbation Theory: Expansions in the Mass of the Strange Quark,” *Nucl. Phys.* **B250**, 465 (1985).
- [28] R. Frezzotti and G. C. Rossi, “Chirally improving Wilson fermions. I: O(a) improvement,” *JHEP* **08**, 007 (2004) hep-lat/0306014.
- [29] ETM P. Boucaud *et al.*, “Dynamical twisted mass fermions with light quarks,” *Phys. Lett.* **B650**, 304 (2007) hep-lat/0701012.
- [30] ETM P. Dimopoulos *et al.*, “Scaling and chiral extrapolation of pion mass and decay constant with maximally twisted mass QCD,” *arXiv:0810.2873* (2008) 0810.2873.
- [31] European Twisted Mass C. Urbach, “Lattice QCD with two light Wilson quarks and maximally twisted mass,” *PoS LAT2007*, 022 (2007) 0710.1517.
- [32] ETM P. Dimopoulos *et al.*, “Scaling and ChPT Description of Pions from $N_f = 2$ twisted mass QCD,” *PoS LAT2009*, 117 (2009) 0912.5198.
- [33] K. G. Wilson, “CONFINEMENT OF QUARKS,” *Phys. Rev.* **D10**, 2445 (1974).

- [34] M. Creutz, “Monte Carlo Study of Quantized SU(2) Gauge Theory,” *Phys. Rev.* **D21**, 2308 (1980).
- [35] I. Montvay and G. Munster, “Quantum fields on a lattice,” Cambridge, UK: Univ. Pr. (1994) 491 p. (Cambridge monographs on mathematical physics).
- [36] J. Smit, “Introduction to quantum fields on a lattice: A robust mate,” *Cambridge Lect. Notes Phys.* **15**, 1 (2002).
- [37] H. J. Rothe, “Lattice gauge theories: An Introduction,” *World Sci. Lect. Notes Phys.* **74**, 1 (2005).
- [38] T. DeGrand and C. E. Detar, “Lattice methods for quantum chromodynamics,” New Jersey, USA: World Scientific (2006) 345 p.
- [39] R. Gupta, “Introduction to lattice QCD,” (1997) hep-lat/9807028.
- [40] C. Davies, “Lattice QCD,” (2002) hep-ph/0205181.
- [41] M. Luscher, “Advanced lattice QCD,” (1998) hep-lat/9802029.
- [42] K. Osterwalder and R. Schrader, “AXIOMS FOR EUCLIDEAN GREEN’S FUNCTIONS,” *Commun. Math. Phys.* **31**, 83 (1973).
- [43] E. Seiler, “Gauge Theories as a Problem of Constructive Quantum Field Theory and Statistical Mechanics,” *Lect. Notes Phys.* **159**, 1 (1982).
- [44] H. B. Nielsen and M. Ninomiya, “No Go Theorem for Regularizing Chiral Fermions,” *Phys. Lett.* **B105**, 219 (1981).
- [45] QCD-TARO P. de Forcrand *et al.*, “Search for effective lattice action of pure QCD,” *Nucl. Phys. Proc. Suppl.* **53**, 938 (1997) hep-lat/9608094.
- [46] P. Weisz, “Continuum Limit Improved Lattice Action for Pure Yang- Mills Theory. 1,” *Nucl. Phys.* **B212**, 1 (1983).

- [47] F. A. Berezin and M. S. Marinov, “Classical Spin and Grassmann Algebra,” *Pisma Zh. Eksp. Teor. Fiz.* **21**, 678 (1975).
- [48] K. Symanzik, “SOME TOPICS IN QUANTUM FIELD THEORY,” Presented at 6th Int. Conf. on Mathematical Physics, Berlin, West Germany, Aug 11-21, 1981.
- [49] K. Symanzik, “Continuum Limit and Improved Action in Lattice Theories. 1. Principles and ϕ^4 Theory,” *Nucl. Phys.* **B226**, 187 (1983).
- [50] K. Symanzik, “Continuum Limit and Improved Action in Lattice Theories. 2. $O(N)$ Nonlinear Sigma Model in Perturbation Theory,” *Nucl. Phys.* **B226**, 205 (1983).
- [51] M. Luscher, S. Sint, R. Sommer, and P. Weisz, “Chiral symmetry and $O(a)$ improvement in lattice QCD,” *Nucl. Phys.* **B478**, 365 (1996) hep-lat/9605038.
- [52] R. Frezzotti, P. A. Grassi, S. Sint, and P. Weisz, “A local formulation of lattice QCD without unphysical fermion zero modes,” *Nucl. Phys. Proc. Suppl.* **83**, 941 (2000) hep-lat/9909003.
- [53] R. Frezzotti, P. A. Grassi, S. Sint, and P. Weisz, “Lattice QCD with a chirally twisted mass term,” *JHEP* **08**, 058 (2001) hep-lat/0101001.
- [54] S. A. Gottlieb and K. Rummukainen, “Resonance Scattering on the Lattice with Non-Zero Total Momentum,” *Nucl. Phys. Proc. Suppl.* **47**, 819 (1996) hep-lat/9509088.
- [55] R. G. Newton, “SCATTERING THEORY OF WAVES AND PARTICLES,” New York, Usa: Springer (1982) 743p.
- [56] J. Goldstone, A. Salam, and S. Weinberg, “Broken Symmetries,” *Phys. Rev.* **127**, 965 (1962).
- [57] S. Weinberg, “Pion scattering lengths,” *Phys. Rev. Lett.* **17**, 616 (1966).
- [58] S. Pislak *et al.*, “High statistics measurement of K_{e4} decay properties,” *Phys. Rev.* **D67**, 072004 (2003) hep-ex/0301040.

- [59] G. Colangelo, J. Gasser, and H. Leutwyler, “The pi pi S-wave scattering lengths,” *Phys. Lett.* **B488**, 261 (2000) hep-ph/0007112.
- [60] G. Colangelo, J. Gasser, and H. Leutwyler, “pi pi scattering,” *Nucl. Phys.* **B603**, 125 (2001) hep-ph/0103088.
- [61] NA48/2 J. R. Batley *et al.*, “New high statistics measurement of K(e4) decay form factors and pi pi scattering phase shifts,” *Eur. Phys. J.* **C54**, 411 (2008).
- [62] J. R. Batley *et al.*, “Determination of the S-wave pi pi scattering lengths from a study of $K^{+-} \rightarrow \pi^{+-} \pi^0 \pi^0$ decays,” *Eur. Phys. J.* **C64**, 589 (2009).
- [63] B. Bloch-Devaux, “Private Communication,” *Private Communication* .
- [64] N. Ishizuka and T. Yamazaki, “I = 2 pion scattering length from two-pion wave function,” *Nucl. Phys. Proc. Suppl.* **129**, 233 (2004) hep-lat/0309168.
- [65] CP-PACS S. Aoki *et al.*, “I = 2 pion scattering length from two-pion wave function,” *Nucl. Phys. Proc. Suppl.* **140**, 305 (2005) hep-lat/0409063.
- [66] CP-PACS S. Aoki *et al.*, “I = 2 pion scattering length from two-pion wave functions,” *Phys. Rev.* **D71**, 094504 (2005) hep-lat/0503025.
- [67] K. Sasaki and N. Ishizuka, “I=2 Two-Pion Wave Functions with Non-zero Total Momentum,” *PoS LAT2007*, 130 (2007) 0710.0434.
- [68] K. Sasaki and N. Ishizuka, “I=2 Two-Pion Wave Function and Scattering Phase Shift,” *Phys. Rev.* **D78**, 014511 (2008) 0804.2941.
- [69] S. R. Sharpe, R. Gupta, and G. W. Kilcup, “Lattice calculation of I = 2 pion scattering length,” *Nucl. Phys.* **B383**, 309 (1992).
- [70] R. Gupta, A. Patel, and S. R. Sharpe, “I = 2 pion scattering amplitude with Wilson fermions,” *Phys. Rev.* **D48**, 388 (1993) hep-lat/9301016.
- [71] Y. Kuramashi, M. Fukugita, H. Mino, M. Okawa, and A. Ukawa, “Lattice QCD calculation of full pion scattering lengths,” *Phys. Rev. Lett.* **71**, 2387 (1993).

- [72] Y. Kuramashi, M. Fukugita, H. Mino, M. Okawa, and A. Ukawa, “Lattice QCD calculation of hadron scattering lengths,” *hep-lat/9312016* (1993) hep-lat/9312016.
- [73] M. Fukugita, Y. Kuramashi, H. Mino, M. Okawa, and A. Ukawa, “An Exploratory study of nucleon-nucleon scattering lengths in lattice QCD,” *Phys. Rev. Lett.* **73**, 2176 (1994) hep-lat/9407012.
- [74] M. Fukugita, Y. Kuramashi, M. Okawa, H. Mino, and A. Ukawa, “Hadron scattering lengths in lattice QCD,” *Phys. Rev.* **D52**, 3003 (1995) hep-lat/9501024.
- [75] JLQCD S. Aoki *et al.*, “ $I = 2$ pion scattering length with Wilson fermions,” *Nucl. Phys. Proc. Suppl.* **83**, 241 (2000) hep-lat/9911025.
- [76] H. R. Fiebig, K. Rabitsch, H. Markum, and A. Mihaly, “Exploring the $\pi^+ \pi^+$ interaction in lattice QCD,” *Few Body Syst.* **29**, 95 (2000) hep-lat/9906002.
- [77] C. Liu, J.-h. Zhang, Y. Chen, and J. P. Ma, “ $I = 2$ pion scattering length from a coarse anisotropic lattice calculation,” *hep-lat/0109010* (2001) hep-lat/0109010.
- [78] CP-PACS S. Aoki *et al.*, “ $I = 2$ pion scattering length and phase shift with Wilson fermions,” *Nucl. Phys. Proc. Suppl.* **106**, 230 (2002) hep-lat/0110151.
- [79] C. Liu, J.-h. Zhang, Y. Chen, and J. P. Ma, “Calculating the $I = 2$ pion scattering length using tadpole improved clover Wilson action on coarse anisotropic lattices,” *Nucl. Phys.* **B624**, 360 (2002) hep-lat/0109020.
- [80] JLQCD S. Aoki *et al.*, “ $I=2$ Pion Scattering Length with the Wilson Fermion,” *Phys. Rev.* **D66**, 077501 (2002) hep-lat/0206011.
- [81] CP-PACS S. Aoki *et al.*, “ $I = 2$ pion scattering phase shift with Wilson fermions,” *Nucl. Phys. Proc. Suppl.* **119**, 311 (2003) hep-lat/0209056.
- [82] CP-PACS S. Aoki *et al.*, “ $I=2$ Pion Scattering Phase Shift with Wilson Fermions,” *Phys. Rev.* **D67**, 014502 (2003) hep-lat/0209124.

- [83] BGR K. J. Juge, “ $I = 2$ pion scattering length with the parametrized fixed point action,” *Nucl. Phys. Proc. Suppl.* **129**, 194 (2004) hep-lat/0309075.
- [84] Bern-Graz-Regensburg C. Gattringer, D. Hierl, and R. Pullirsch, “Pion scattering on the lattice with chirally improved fermions,” *Nucl. Phys. Proc. Suppl.* **140**, 308 (2005) hep-lat/0409064.
- [85] CLQCD X. Li *et al.*, “Hadron Scattering in an Asymmetric Box,” *JHEP* **06**, 053 (2007) hep-lat/0703015.
- [86] T. Umeda, “A constant contribution in meson correlators at finite temperature,” *Phys. Rev.* **D75**, 094502 (2007) hep-lat/0701005.
- [87] UKQCD M. Foster and C. Michael, “Quark mass dependence of hadron masses from lattice QCD,” *Phys. Rev.* **D59**, 074503 (1999) hep-lat/9810021.
- [88] UKQCD C. McNeile and C. Michael, “Decay width of light quark hybrid meson from the lattice,” *Phys. Rev.* **D73**, 074506 (2006) hep-lat/0603007.
- [89] ETM P. Boucaud *et al.*, “Dynamical Twisted Mass Fermions with Light Quarks: Simulation and Analysis Details,” *Comput. Phys. Commun.* **179**, 695 (2008) 0803.0224.
- [90] ALPHA U. Wolff, “Monte Carlo errors with less errors,” *Comput. Phys. Commun.* **156**, 143 (2004) hep-lat/0306017.
- [91] P. Dimopoulos, R. Frezzotti, C. Michael, G. C. Rossi, and C. Urbach, “ $O(a^2)$ cutoff effects in lattice Wilson fermion simulations,” *arXiv:0908.0451* (2009) 0908.0451.
- [92] P. F. Bedaque, I. Sato, and A. Walker-Loud, “Finite volume corrections to pi pi scattering,” *Phys. Rev.* **D73**, 074501 (2006) hep-lat/0601033.
- [93] M. I. Buchoff, J.-W. Chen, and A. Walker-Loud, “pi-pi Scattering in Twisted Mass Chiral Perturbation Theory,” *Phys. Rev.* **79**, 074503 (2009) 0810.2464.
- [94] J. Gasser and H. Leutwyler, “Low-Energy Theorems as Precision Tests of QCD,” *Phys. Lett.* **B125**, 325 (1983).

- [95] J. Bijnens, G. Colangelo, G. Ecker, J. Gasser, and M. E. Sainio, “Pion pion scattering at low energy,” *Nucl. Phys.* **B508**, 263 (1997) hep-ph/9707291.
- [96] C. Aubin and T. Blum, “Calculating the hadronic vacuum polarization and leading hadronic contribution to the muon anomalous magnetic moment with improved staggered quarks,” *Phys. Rev.* **D75**, 114502 (2007) hep-lat/0608011.
- [97] D. B. Renner and X. Feng, “Hadronic contribution to g-2 from twisted mass fermions,” *PoS LATTICE2008*, 129 (2008) 0902.2796.
- [98] R. Frezzotti, V. Lubicz, and S. Simula, “Electromagnetic form factor of the pion from twisted-mass lattice QCD at Nf=2,” *Phys. Rev.* **D79**, 074506 (2009) 0812.4042.
- [99] S. A. Gottlieb, P. B. Mackenzie, H. B. Thacker, and D. Weingarten, “The rho- pi pi Coupling Constant in Lattice Gauge Theory,” *Phys. Lett.* **B134**, 346 (1984).
- [100] R. D. Loft and T. A. DeGrand, “VECTOR MESON DECAY INTO PSEUDOSCALARS FROM QUENCHED LATTICE QCD,” *Phys. Rev.* **D39**, 2692 (1989).
- [101] UKQCD C. McNeile and C. Michael, “Hadronic decay of a vector meson from the lattice,” *Phys. Lett.* **B556**, 177 (2003) hep-lat/0212020.
- [102] CP-PACS S. Aoki *et al.*, “Lattice QCD Calculation of the ρ Meson Decay Width,” *Phys. Rev.* **D76**, 094506 (2007) 0708.3705.
- [103] QCDSF M. Gockeler *et al.*, “Extracting the rho resonance from lattice QCD simulations at small quark masses,” *arXiv:0810.5337* (2008) 0810.5337.
- [104] S. Durr *et al.*, “Ab-Initio Determination of Light Hadron Masses,” *Science* **322**, 1224 (2008) 0906.3599.
- [105] ETM C. Michael and C. Urbach, “Neutral mesons and disconnected diagrams in Twisted Mass QCD,” *PoS LAT2007*, 122 (2007) 0709.4564.
- [106] L. S. Brown and R. L. Goble, “Pion-Pion Scattering, Current Algebra, Unitarity, and the Width of the Rho Meson,” *Phys. Rev. Lett.* **20**, 346 (1968).

- [107] E. E. Jenkins, A. V. Manohar, and M. B. Wise, “Chiral Perturbation Theory for Vector Mesons,” *Phys. Rev. Lett.* **75**, 2272 (1995) hep-ph/9506356.
- [108] J. Bijnens, P. Gosdzinsky, and P. Talavera, “Vector meson masses in chiral perturbation theory,” *Nucl. Phys.* **B501**, 495 (1997) hep-ph/9704212.
- [109] P. C. Bruns and U.-G. Meissner, “Infrared regularization for spin-1 fields,” *Eur. Phys. J.* **C40**, 97 (2005) hep-ph/0411223.
- [110] C. Hanhart, J. R. Pelaez, and G. Rios, “Quark mass dependence of the rho and sigma from dispersion relations and Chiral Perturbation Theory,” *Phys. Rev. Lett.* **100**, 152001 (2008) 0801.2871.
- [111] D. Djukanovic, J. Gegelia, A. Keller, and S. Scherer, “Complex mass renormalization in EFT,” (2010) 1001.1772.
- [112] QCDSF M. Gockeler *et al.*, “Vacuum polarisation and hadronic contribution to muon g-2 from lattice QCD,” *Nucl. Phys.* **B688**, 135 (2004) hep-lat/0312032.
- [113] JLQCD E. Shintani *et al.*, “Lattice study of the vacuum polarization function and determination of the strong coupling constant,” *Phys. Rev.* **D79**, 074510 (2009) 0807.0556.
- [114] E. Shintani *et al.*, “Strong coupling constant from vacuum polarization functions in three-flavor lattice QCD with dynamical overlap fermions,” (2010) 1002.0371.
- [115] P. A. M. Dirac, “The Quantum theory of electron,” *Proc. Roy. Soc. Lond.* **A117**, 610 (1928).
- [116] P. A. M. Dirac, “The Quantum theory of electron. 2,” *Proc. Roy. Soc. Lond.* **A118**, 351 (1928).
- [117] J. S. Schwinger, “On Quantum electrodynamics and the magnetic moment of the electron,” *Phys. Rev.* **73**, 416 (1948).
- [118] F. Jegerlehner and A. Nyffeler, “The Muon g-2,” *Phys. Rept.* **477**, 1 (2009) 0902.3360.

- [119] BABAR B. Aubert *et al.*, “Precise measurement of the $e^+ e^-$ to $\pi^+ \pi^- (\gamma)$ cross section with the Initial State Radiation method at BABAR,” *Phys. Rev. Lett.* **103**, 231801 (2009) 0908.3589.
- [120] Belle M. Fujikawa *et al.*, “High-Statistics Study of the $\tau^- \rightarrow \pi^- \pi^0 \nu_\tau$ Decay,” *Phys. Rev.* **D78**, 072006 (2008) 0805.3773.
- [121] M. Bochicchio, L. Maiani, G. Martinelli, G. C. Rossi, and M. Testa, “Chiral Symmetry on the Lattice with Wilson Fermions,” *Nucl. Phys.* **B262**, 331 (1985).
- [122] K. G. Chetyrkin, J. H. Kuhn, and M. Steinhauser, “Three-loop polarization function and $O(\alpha(s)^2)$ corrections to the production of heavy quarks,” *Nucl. Phys.* **B482**, 213 (1996) hep-ph/9606230.
- [123] K. G. Chetyrkin, R. V. Harlander, and J. H. Kuhn, “Quartic mass corrections to $R(\text{had})$ at $O(\alpha(s)^3)$,” *Nucl. Phys.* **B586**, 56 (2000) hep-ph/0005139.
- [124] F. Jegerlehner, “The anomalous magnetic moment of the muon,” Berlin, Germany: Springer (2008) 426 p.
- [125] G. Ecker, J. Gasser, A. Pich, and E. de Rafael, “The Role of Resonances in Chiral Perturbation Theory,” *Nucl. Phys.* **B321**, 311 (1989).
- [126] G. Zweig, “An $SU(3)$ model for strong interaction symmetry and its breaking,” CERN-TH-401.
- [127] G. Zweig, “AN $SU(3)$ MODEL FOR STRONG INTERACTION SYMMETRY AND ITS BREAKING. 2,” CERN-TH-412.
- [128] L. Lellouch and M. Luscher, “Weak transition matrix elements from finite-volume correlation functions,” *Commun. Math. Phys.* **219**, 31 (2001) hep-lat/0003023.

CURRICULUM VITAE

Information

Name: Xu Feng
Date of Birth: April 16, 1982
Place of Birth: Zhejiang, P. R. China
Nationality: P. R. China

Education

09.1989 – 07.1994 Daxi Primary School, Zhejiang, China
09.1994 – 07.1997 Daxi Middle School, Zhejiang, China
09.1997 – 07.2000 Wenling Middle School, Zhejiang, China
07.2000 Higher Education Entrance Qualification

Higher Education

09.2000 – 07.2004 Studies of Physics at Peking University, Beijing, China
Thesis: Two particle states in an asymmetric box
and the elastic scattering phases
Under Supervision of Prof. Chuan Liu
07.2004 B.S. in Physics with High Honors
09.2004 – 07.2007 Studies of Theoretical Physics at Peking University,
Beijing, China
Thesis: Study of two-particle scattering and chiral
fermions on lattices
Under Supervision of Prof. Chuan Liu
07.2007 M.S. in Physics with High Honors

Ph.D. Study

08.2007 Beginning of Ph.D. Study at DESY Zeuthen
& University of Münster
Under Supervision of Priv.-Doz. Dr. Karl Jansen
& Prof. Dr. Gernot Münster